TAMPEREEN TEKNILLINEN YLIOPISTO
TAMPERE UNIVERSITY OF TECHNOLOGY
Julkaisu 586 • Publication 586

Mika Masti

Hall Magnetometer for AC Characterization and Test Results of Bi-2223 Tape Specimens

Tampere 2006

Tampereen teknillinen yliopisto. Julkaisu 586
Tampere University of Technology. Publication 586

Mika Masti

Hall Magnetometer for AC Characterization and Test Results of Bi-2223 Tape Specimens

Thesis for the degree of Doctor of Technology to be presented with due permission for public examination and criticism in Sähkötalo Building, Auditorium S1, at Tampere University of Technology, on the 17th of February 2006, at 12 noon.

Tampereen teknillinen yliopisto - Tampere University of Technology
Tampere 2006

ISBN 952-15-1548-1 (printed)
ISBN 952-15-1816-2 (PDF)
ISSN 1459-2045

Abstract

The economically viable use of HTS superconductors poses strict demands on the manufacturing and operational losses of superconducting tapes. Both these losses are minimized with an appropriate choice of tape cross-section and manufacturing process. They can be optimized with systematic testing of different combinations, but such testing is expensive, consumes plenty of time and provides only few answers as to the sources of the internal losses in the tested tapes.

In this thesis, Hall sensor modification for AC characterization has been made to enable novel AC measurements and to gain new information about the current distributions causing AC maps. The work involved analysis of the reproducibility and accuracy of the measurement and calculation methods. In addition, DC measurements and their analysis were included to help visualize the differences between DC and AC maps. New tools based on the discrete Fourier transformation were developed to determine the optimal current distribution among several assumed current penetration models.

The modified AC Hall magnetometer proved to be inexpensive, robust, simple to use, and well suited for tape manufacturers to test systematically their specimens. Test tools for the estimation of the inversion errors proved to give tight error limits. Comparison between Hall sensor and magnetic knife measurements showed that these methods should be used complementary to examine possible current variations in the cross-section of the tape. DFT analysis was used to test penetration models and find estimates on tape I_c and penetration model parameter G, even thicknesswise evolution of current density could be distinguished. The third harmonic content was shown to be crucial in optimization.

Preface

The work presented in this thesis was made at the Institute of Electromagnetics in the Tampere University of Technology during my 5 years of post-graduate studies between 2000-2005. Main part of the work was funded by Institute, parts of the work by EU project funding.

First of all, I send my thanks to the numerous colleagues all over Europe and Asia I've had the priviledge to work or discuss with, unfortunately they're too numerous to list here. However, I must name especially the highly skilled and easy to work with professionals of Bratislava, Institute of Electrical Engineering. Especially Jozef Kvitkovič, Milan Polák, Pavol Kováč, Fedor Gömöry, Ľubomír Kopera, and Tibor Melíšek among several others. Keep up your excellent work and all the best for you all.

Naturally, I'm also greatly indebted to the persons supervising and assisting my research, Jorma Lehtonen, Risto Mikkonen, Lasse Söderlund and Lauri Kettunen. Especially without Jorma, this thesis would not have completed in the present form. My special thanks goes to Tapio Kalliohaka, Raine Perälä and Iiro Hiltunen, the three laboratory wizards I've been fortunate enough to know and work with. I want to thank Jaakko Paasi for guiding me to the wondrous world of superconductivity in the beginning of my scientific career. The rest of the Institute deserve no less compliments, since my often slightly-low-tolerance-to-computer-malfunctions and other peculiar habits have been tolerated very well and apparently people now even look forward to help and comfort me when my computer refuses to co-operate. My special thanks on this and several other matters goes to Maria Ahoranta, who has been most unlucky and shared an office room with me for many years. She has kept me more or less sane through these years and apparently survided the burden herself admirably.

My thanks to Heidi Koskela, who prepared several pictures of this thesis and Maija-Liisa Paasonen, who was indispensable help when I needed to send packages abroad or use the infernal fax-machine of the Institute. Thanks for Timo Lepistö for correcting mistakes caused by my far-less-than-perfect-English-grammar, although I'm sure I've added several mistakes after the grammar check.

My warm thanks to my good old friends, Mikko Tasanen, Tero Vuorela, Mikko Asunta, Jussi Mikkonen, Ossi Toivonen, Nina Hjelm, Joonas Kaarnametsä and many others. How on earth have you tolerated me for all these years? Thanks for being there when I need you.

My thanks also to my parents-in-law, Jaakko and Irene Alanko, thanks for letting me in to your family and making me feel at home. Naturally, I'm deeply grateful to my parents, Juhani and Aila Masti, for their love and care through all these years. I must also thank my little sister, Erja Masti, for making my life more, let's say, interesting. I love you sis, don't wear yourself out in your busy lifestyle. And the most important, my loving thanks to You, my dear wife Niina-Maaret, you've taken the greatest burden of them all, life with me. This thesis wouldn't be possible without your support and understanding, thanks for being at my side.

Mika Masti, 17.2.2006 in Tampere

List of Publications

Publication **I**

Masti M, Lehtonen J, Perälä R, and Mikkonen R

Magnetic flux density maps caused by DC, AC and remanence currents around artificial defects in Bi-2223/Ag tapes

Physica C **386** (2003) 1-4

Publication **II**

Masti M, Lehtonen J, Mikkonen R, and Rostila L

Accuracy of numerical analysis for Hall sensor magnetometer measurements

IEEE Trans. Appl. Supercond. **13** (2003) 3671-3674

Publication **III**

Masti M, Lehtonen J, Perälä R, Nah W, and Kang J

Comparison of voltage-current characteristics of high quality Bi-2223 tapes with Hall-sensor measurements and computed current density distributions

Physica C **401** (2004) 155-159

Publication **IV**

Masti M, Lehtonen J, Perälä R, Joronen J, Goldacker W, Zabara O, Nast R, Arndt T J, Bruzek C-E, and Lallouet N

Hall sensor magnetometer measurements of Bi-HTS tapes for low AC loss applications

IEEE Trans. Appl. Supercond. **14** (2004) 1074-1077

Publication **V**

Masti M, Lehtonen J, Perälä R, Mikkonen R, Söderlund L, and Seppälä P

Hall sensor magnetometer for AC characterization of high temperature superconducting tapes

Meas. Sci. Technol. **16** (2005) 1092–1098

Publication **VI**

Kováč P, Masti M, Lehtonen J, Kopera L, Kawano K, Abell S, Metz B, and Dhallé M

Comparison and analysis of Hall probe scanning, magneto-optical imaging and magnetic knife measurements of Bi-2223/Ag tape

Supercond. Sci. Technol. **18** (2005) 805-812

Publication **VII**

Masti M, Lehtonen J, and Mikkonen R

Discrete Fourier transformation analysis of AC Hall sensor magnetometer measurements of high temperature superconductor tapes

Supercond. Sci. Technol. **18** (2005) 1428-1436

Contents

List of Symbols

A	Matrix of the calculation model
a	x-direction semi-axe of an elliptical filament zone
A_+	Cross-sectional area of positive current
A_-	Cross-sectional area of negative current
A_{ave}	Average amplitude of A_m in a measured map
A_b	Cross-sectional area of an ellipse between A_+ and A_-
a_b	x-direction semi-axe of an ellipse between A_+ and A_-
A_m	Fitted value of current amplitude at mth spatial point
A_{max}	Cross-sectional area of a filamentary zone ellipse
A_{min}	Cross-sectional area of a current free center ellipse
a_{min}	x-direction semi-axe of a current free center ellipse
$\mathbf{B}$	Magnetic flux density vector
b	z-direction semi-axe of an elliptical filament zone
B^*	Magnetic flux density of full penetration, specimen parameter
B_0	Fitting constant of Kim's model
B_{ave}	Average magnetic flux density in $i_{CDD}(\pm W/2)$
b_b	z-direction semi-axe of an ellipse between A_+ and A_-
B_c	Critical magnetic flux density, material constant
B_{c1}	Material parameter of type II superconductors
B_{c2}	Material parameter of type II superconductors
$\mathbf{B}_e$	External magnetic flux density vector
B_{max}	Magnetic flux density maximum during an example B_e cycle
b_{min}	z-direction semi-axe of a current free center ellipse
$\mathbf{B}_s$	Magnetic flux density caused by internal currents
$\mathbf{B}_z$	Measured B_z values above current elements
B_z	B component parallel to tape broad face normal
B_{zi}	ith component of $\mathbf{B}_z$
B_{zrs}	Magnetic flux density component B_z caused by I_{rs}
C	Number of cycles, measurement parameter
C_{mk}	kth frequency component of mth simulation point c_{mn}
c_{mn}	nth sample of simulated B_z at mth point
$\mathbf{E}$	Electric field vector
E_0	Calculation parameter defining total current
e_B	Relative error ratio due to $\delta\mathbf{B}_z$
E_c	Critical electric field strength, selectable parameter
E_{eB}	Error e_B expectation value
e_{max}	Maximum percentage of e_{mmean} compared to A_{ave}
e_{mean}	Mean percentage of e_{mmean} compared to A_{ave}
e_{mmean}	Mean deviation between fitted sinusoid and i_{mn}

e_{num}	Relative numerical error when $\delta\mathbf{B}_z = 0$
F	Measured transport current frequency
f	Transport current frequency
f_{ave}	Average frequency of f_m in a measured map
ff	Fill-factor of the filament-zone area
f_k	Frequency corresponding to kth frequency component
f_m	Fitted value of current frequency at mth spatial point
FS_m	Frequency spectrum of mth measurement point
G	Penetration model parameter
G_1	Optimal G parameter from Δ_1 optimization
G_{13}	Optimal G parameter from Δ_{13} optimization
h	Filament-zone height in simulations
H	Tape thickness
h_{f}	Filament height in simulations
h_{m}	Measurement height in simulations
h_{SC}	Local superconductor structure thickness
$\mathbf{I}$	Current amplitudes I_j in current elements
I	Current amplitude
I^*	Current of full penetration
I_1	Left filament zone current in model case II and III
I_{11}	Current meandering inside left filament zone
I_{12}	Current between left and center filament zones
I_2	Center filament zone current in model case II and III
I_{22}	Current meandering inside center filament zone
I_{23}	Current between center and right filament zones
I_3	Right filament zone current in model case II and III
I_{33}	Current meandering inside right filament zone
I_{c}	Critical current, specimen parameter
I_{c1}	Optimal I_{c} parameter from Δ_1 optimization
I_{c13}	Optimal I_{c} parameter from Δ_{13} optimization
i_{CDD}	Current per unit width, calculated from J_{CDD}
I_j	jth component of $\mathbf{I}$
i_{LSF}	Current per unit width, calculated from currents I_j
i_{mn}	Current sample n from mth spatial point, scaled $v_{\text{I}mn}$
I_{N}	Normalized transport current amplitude
I_{N1}	Current I_{op} normalized to I_{c1}
I_{N13}	Current I_{op} normalized to I_{c13}
I_{neg}	Negative current amplitude
I_{op}	Transport current amplitude, for both DC and AC currents
I_{pos}	Positive current amplitude
I_{rs}	Current amplitude in current thread rs
i_{T}	Transport current
$\text{I}_{\text{T}mk}$	kth frequency component of mth measurement point i_{mn}
$\mathbf{J}$	Current density vector
J_{c}	Critical current density, local specimen parameter
J_{c0}	Critical current density in zero B_z field
J_{CDD}	Current density solution of CDD model
J_{x}	Current density component parallel to tape width

J_y	Current density component parallel to tape length
$\mathbf{J}_y$	Vector containing the calculated current density components J_y
$\hat{\mathbf{J}}_y$	Solution of a disturbed system
J_{yi}	ith component of vector $\mathbf{J}_y$
J_z	Current density component parallel to tape thickness
K	Index of kth frequency component referring to $f_k = f$
L	Index of kth frequency component referring to $f_k = 3f$
L_V	Distance between voltage taps
m_1	SP_k profile lower end spatial index
m_2	SP_k profile higher end spatial index
N	Number of samples
n	Specimen parameter defining curvature of $E(J)$ curve
N_J	Number of current elements
N_L	Number of filament layers in simulations
N_M	Number of spatial measurement points
N_{rs}	Temporary variable for defining negative current threads
N_S	Number of simulations
O_{ave}	Average amplitude of O_m in a measured map
O_m	Fitted value of current offset at mth spatial point
p	Parameter defining the norm used
P_{rs}	Temporary variable for defining positive current threads
Q	AC losses per cycle
$\mathbf{r}'$	Position vector in volume Ω
$\mathbf{r}$	Position vector
$\mathbf{r}_j$	Position vector of a spatial measurement point
R_p	Resistance used in digitization of downscaled current
S	Separable function of B_z dependence of J_c
S_{PC}	Samples per cycle, measurement parameter
SP_k	Spatial profile of kth frequency components
t	Time
T_c	Critical temperature, material constant
t_{In}	Time of sample n from trigger
V	Voltage
v_{Hm}	Hall voltage at spatial point m
V_{Hmk}	kth frequency component of mth measurement point v_{Hmn}
v_{Hmn}	Hall voltage sample n from mth spatial point
v_{Hm}^{ave}	Average cycle Hall voltage at spatial point m
v_{Imn}	Downscaled current signal sample n from mth point
w	Filament-zone width in simulations
W	Tape width
w_f	Filament width in simulations
w_m	Measurement width in simulations
x	Direction of specimen width
x_0	Spatial point of turning magnetic flux density in MK
x_m	x-coordinate of mth measurement point
x_{max}	Spatial point corresponding to maximum of SP_K
x_{mid}	Spatial middle point between x_{max} and SP_K minimum

X_{rs}	x-coordinate of current thread *rs* center
y	Direction of specimen length
z	Direction of specimen broad face normal
z_m	z-coordinate of *m*th measurement point
Z_{rs}	z-coordinate of current thread *rs* center
Δ_1	Error function for main frequency *f* optimization
Δ_{13}	Sum of error functions Δ_1 and Δ_3
Δ_3	Error function for third harmonic frequency 3*f* optimization
ΔA	Variation range of A_m in a measured map
Δf	Variation range of f_m in a measured map
ΔO	Variation range of O_m in a measured map
Φ_0	Flux quantum, magnetic flux inside a flux line
Υ_{eB}	Cumulative distribution function of e_B
Ω	Integration volume where currents flow
α	Fitting constant of Kim's model
β	Angle between B_e and normal of the tape broad face
δA	Disturbance in matrix *A*
$\delta \mathbf{B}_z$	Disturbance in vector $\mathbf{B}_z$
$\delta \mathbf{J}_y$	Resultant error in $\mathbf{J}_y$ by disturbances
δJ_{yi}	*i*th component of vector $\delta \mathbf{J}_y$
ε	Probability percentage of density function
γ	Desired transport current phase
φ_{mn}	Current phase of *n*th sample from *m*th spatial point
κ	Condition number of matrix *A*
μ_0	Vacuum permeability
θ	Transport current phase
θ_m	Transport current initial phase at spatial point *m*
θ_n	Current phase of *n*th simulated sample
σ_B	Standard deviation of error distribution $\delta \mathbf{B}_z$
σ_{eB}	Standard deviation of error e_B

List of Abbreviations

2D	Two dimensional
3D	Three dimensional
AD	Analogue-to-digital
Bi-2212	$Bi_2Sr_2CaCu_2O_8$, Bismuth-based HTS material
Bi-2223	$(Bi,Pb)_2Sr_2Ca_2Cu_3O_{10}$, Bismuth-based HTS material
Bi-2223/Ag	Bi-2223 based HTS tape with silver matrix
CDD	Current Density Distribution, model abbreviation
CT	High precision current transducer
DAQ	Data Acquisition Card
DFT	Discrete Fourier Transformation, analysis tool
GPIB	General Purpose Interface Bus
HS	Hall sensor magnetometer
HTS	High Temperature Superconductors
LN_2	Liquid nitrogen, at 77 K
LSF	Least Squares Fitting, calculation method abbreviation
LTS	Low Temperature Superconductors
MgB_2	Recently discovered superconductor material
MK	Magnetic knife
MRI	Magnetic Resonance Imaging, clinical measurement tool
Nb_3Sn	Common LTS material
NbTi	Another common LTS material
OPERA	Commercial FEM calculation program
OPIT	Oxide Powder In Tube, manufacturing method
TIRT	Tape In Rectangular Tube, manufacturing method
YBCO	$YBa_2Cu_3O_7$, Yttrium-based HTS material

1 Introduction

Superconductivity was discovered by Heike Kamerlingh Onnes in 1911. In the following years, numerous materials and alloys were found to be superconductive, but only few proved to be technically feasible. In 1986, a new ceramic material class of superconductors was discovered, but though these materials allowed operation at much higher temperatures, they were extremely difficult to manufacture so as to have acceptable electromagnetic and mechanical properties. The older materials, found before 1986, are called low temperature superconductors (LTS) because of their highest critical temperature of 23 K, and the ceramic materials found after 1986 are called high temperature superconductors (HTS).

The best known LTS materials are NbTi and Nb_3Sn. MgB_2, which was discovered as late as 2001 and may replace NbTi or Nb_3Sn in some future applications, is classified as neither LTS nor HTS. The primary HTS materials so far are $YBa_2Cu_3O_7$ (YBCO), $Bi_2Sr_2CaCu_2O_8$, (Bi-2212), and $(Bi,Pb)_2Sr_2Ca_2Cu_3O_{10}$ (Bi-2223) [87]. These materials are manufactured in various forms for different applications [37], but a bendable wire, tape, or cable is the preferred current carrying element in power applications. Except for YBCO tapes, current carrying elements are often manufactured as a straight or twisted multifilament structure embedded in a metal matrix [3,4,36,48,53]. YBCO tapes are manufactured typically in the form of a thin layer placed on top of a specially prepared substrate to help the grains orient more precisely [93].

The applications enabled by superconductors are called *enabling applications*, whereas other applications in some ways improved by superconductors are called *replacing applications*. The limiting factor between these two applications is economical viability. In enabling applications, such as MRI and particle physics accelerators or detectors, costs are not the primary factor in deciding whether to build the application or

not. On the other hand, replacing existing applications with superconducting counterparts must be economical to make them attractive on the market.

The cost of an application system comprises the initial cost plus operational costs, the former being reducible through optimization of raw materials and manufacturing processes whereas the latter come from losses in the superconductors. In DC operation, superconductors can exhibit practically no losses at all. However, most power applications operate in the AC regime, which unfortunately causes small losses in superconductors generated at their operation temperature. Consequently, much more cooling power is needed at room temperature to compensate for these losses. This effect is called the cooling penalty, and its exact value is determined by the Carnot factor and the efficiency of the cooling machine. For example, at room temperature, we need 10-20 times more cooling power to compensate for the power lost at 77 K. Therefore, the cooling penalty, heat leaks from the system's surroundings, and often higher initial cost compared to the technology to be replaced pose strict AC loss limits on all technically feasible wires, tapes, and cables. LTS materials are considered uneconomical practically for all replacing applications because of the high cooling penalty caused by their low operation temperature, typically 4.2 K. Nevertheless, engineers and scientists have been struggling for years to produce sufficiently long pieces of HTS tapes with adequate mechanical and electromagnetic characteristics and with a price tag to make them economically viable [24,66].

1.1 Aim of the thesis

Systematic testing of different combinations of tape structure and manufacturing process is a straightforward way to find the best tape [19]. Unfortunately, such testing consumes time and resources and provides few answers as to the sources of the internal losses in the tested tapes. Hence it is difficult to estimate if a tape's poor performance is due to failures in manufacture or to the tape's inefficient structure.

For more efficient screening, it would help us greatly to find out more about how current density is distributed inside particular specimens, though direct measurements herein would also disturb the distribution itself. Because of this constraint, measurements

are often focused on mapping the magnetic flux density around HTS tapes [29,38,55,74,95] and on estimating the current density distribution that possibly causes these maps [44,46,96], though even these methods are of limited resolution and often numerically unstable. Furthermore, since measured DC and AC magnetic flux density maps clearly differ from each other [54], the tapes should be characterized in both DC and AC conditions.

Based on the above, this thesis thus aimed to modify the Hall system magnetometer to enable novel AC measurements and to gain new information about the current distributions causing AC maps. The work naturally involved analysis of the reproducibility and accuracy of the measurement and calculation methods. In addition, DC measurements and their analysis were included to help visualize the differences between DC and AC maps. To analyze current densities, I developed a new tool based on the discrete Fourier transformation and used it to determine the optimal current distribution among several assumed current penetration models.

At the beginning of this thesis work, Bi-2223 was generally known as the prime HTS material. Therefore, measurements were started with Bi-2223 specimens, and no other materials were studied in order to keep all results comparable. Excluded was also calculation of AC losses as it is relatively straightforward after we learn how current density evolves. The SI-system was used throughout to define units and the magnetic field equations.

1.2 Structure of the thesis

Chapter 2 provides the basic definitions and concepts of superconductivity necessary for readers to understand the rest of the thesis. Chapter 3 presents the AC Hall magnetometer and its auxiliaries. The relevant parts of the system and the measurement process itself are explained in detail together with error sources and error estimates. Chapter 4 demonstrates the numerical instability of the process often used to calculate current density distributions and introduces a simple alternative, which is later used extensively to determine the best estimate of current density distributions. Chapter 5 discusses the visible differences between measured magnetic flux density maps and argues

for the method's simplicity and effectiveness in distinguishing between clearly different current densities. Chapter 6 compares the results of the Hall sensor magnetometer with those of the magnetic knife and shows how combining these methods can help uncover reasons behind observed current densities. Chapter 7 presents the calculation of current density distributions under two transient current states: voltage-current measurement and the AC cycle. Chapter 8, which summarizes the results, is followed by the seven publications that constitute the scientific core of this thesis.

1.3 Author's contribution

In all the publications, I, assisted by Mr. R. Perälä, conducted the Hall measurements as well as wrote the text, except for paper number 6, that was authored and mainly written by Dr. P. Kováč. Doctors J. Lehtonen and R. Mikkonen supervised the papers and provided invaluable insights during discussions. Together with Mr. L. Rostila, I wrote the codes for the statistical comparison in publication 2 and made most of the calculations. Doctors W. Nah and J. Kang made the calculations for publication 3. In publication 4, most measurements were inspected by Mr. J. Joronen under my supervision while the other co-authors provided specimens. I performed the verifying calculations together with Dr. J. Lehtonen. In publication 5, I designed the AC Hall system measurement and the post-processing software and post-processed the results while Messrs. L. Söderlund and P. Seppälä provided the custom-made current source. In publication 6, I wrote part of the text on the calculation of current density distributions and the information available on combined systems. Other co-authors provided specimens, magneto-optical and magnetic knife measurements, and parts of the text. In publication 7, I made the calculation and additional measurements.

2 Superconductivity

This chapter introduces the readers to the basic concepts and material classes of superconductivity to help them understand the subsequent chapters (further information on basic superconducting terms is available, for example, in [20,52,91]). Since this thesis concentrates on detecting macroscopical variations in current densities inside superconductor tapes, microscopical material structures and theories are kept at a minimum.

2.1 Basic definitions

All superconductive materials have a characteristic critical temperature, T_c, at which electrical resistivity suddenly drops within a narrow temperature range, and the material is said to pass into the superconductive state. A limited testing time does not allow us to determine whether the resistance drops to zero or only very close to it. Experiments on persistent current rings show the current's characteristic decaying time to be more than 10^5 years [91]. Therefore, *perfect conductivity* seems a fitting term for this first property, and cables, motors, and magnets are some of the power applications that currently exploit the phenomenon [32,34,42,65,67].

Perfect diamagnetism

When cooled in an external magnetic field B_e, a superconductor passes into the superconductive state at a temperature lower than T_c. In addition, when the material passes into this state, the magnetic field, except for a thin screening current layer at the surface, is expulsed from the material. This reversible expulsion is called the Meissner effect or alternatively *perfect diamagnetism*. The bigger the B_e, the lower the temperature must be for expulsion to occur. When B_e equals the critical magnetic flux density, B_c, the material

does not expulse B_e at any temperature. Meissner effect is exploited, for example, in magnetically levitated trains and fault current limiters [34,67,70].

Since a current creates a magnetic flux density around itself, it is only natural that superconductors also have a critical current density, J_c, which limits the specimen's current carrying capabilities. Unlike the previous two, this parameter is not a material constant but rather a manufacturing-process-dependent local value, which is often determined as an average value over the specimen. These three limiting values are interdependent and together define the specimen's critical surface between normal and superconductive states.

Type I and type II superconductors

Magnetic flux density can penetrate the material in two distinctly different ways. In so-called type I materials, the $B_e > B_c$ penetrates the whole specimen instantly and turns it fully into a normal state. In type II materials, the B_e forms "flux lines" that penetrate the specimen when $B_e > B_{c1}$. A flux line is a normal-conductive area containing one flux quantum, $\Phi_0 \approx 2 \cdot 10^{-15}$ Wb, surrounded by supercurrents. When B_e is further increased, the number of flux lines increases. At $B_e = B_{c2}$, the normal-conductive areas in the flux lines overlap, and the specimen progresses fully into the normal state. When B_e is between B_{c1} and B_{c2}, the specimen is said to be in a mixed or vortex state. It is important that we understand the mixed state because all technically applicable superconductors are of type II materials. B_{c1} is typically in the order of 100 mT and B_{c2} around tens of teslas or even above 100 T, depending on the temperature and material. This means that in most of their applications, these superconductors operate in the mixed state.

If flux lines could move freely, they would distribute evenly over the whole specimen and redistribute always when B_e is changed. Practical superconductors, however, have dislocations, crystal defects, and other inhomogeneous parts that hinder the movement of flux lines. Therefore, when B_e is increased beyond B_{c1}, flux lines cross the specimen surface but are pinned down close to the edge, creating a gradual magnetic flux density decline between the edge at B_e and the magnetic flux density free inner part of the specimen.

Bean model

According to Ampere's law, a gradual magnetic flux density decline creates a current at right angles to it and vice versa. In 1962, C. Bean proposed that the pinning determines a maximum magnetic flux density gradient and, therefore, a critical current J_c in the specimen [8]. According to Bean's model, B_e causes screening currents of the current density J_c inside the specimen. In his model, three possible current density values exist inside the specimen: $+J_c$, $-J_c$, and 0. Currents start at the specimen edges and penetrate deeper as B_e is increased. When B_e reaches B^*, that is, the full penetration magnetic flux density, the flux lines have reached the center of the specimen. After the specimen is fully penetrated, the current distribution does not change but the magnetic flux density inside the specimen grows evenly until at B_{c2} the specimen passes into the normal state. If B_e is decreased, screening currents change direction first at the specimen edges and penetrate deeper at decreasing B_e. If B_e is lowered to zero before it has reached B^*, a current free inner part of the specimen remains after the B_e cycle. Figure 2.1 shows the magnetic flux penetration in several B_e cases.

***E*(*J*) characteristics**

The superconductor behavior is characterized by the so-called *V*(*I*) measurement, often done as a four-point measurement in which a slowly increasing current ramp is fed through the specimen from its ends. Two voltage taps are attached on top of the specimen, often a few millimeters or centimeters apart. The voltage from these taps is recorded together with the current fed through the specimen, and the result is reported as the specimen's *V*(*I*) curve. Typically, *E*(*J*) characteristics are calculated from the *V*(*I*) measurement by simply dividing *I* by the cross-section of the superconductor and *V* by the distance between the voltage taps.

The critical current I_c is the current value at which the measured voltage V equals L_V times the selectable threshold value E_c, where L_V is the length between the voltage taps. Quite often with HTS materials, 1 $\mu V\ cm^{-1}$ is used as an E_c criterion. The critical current density J_c is typically assumed constant over the cross-section and therefore calculated by dividing I_c by the superconductor cross-section.

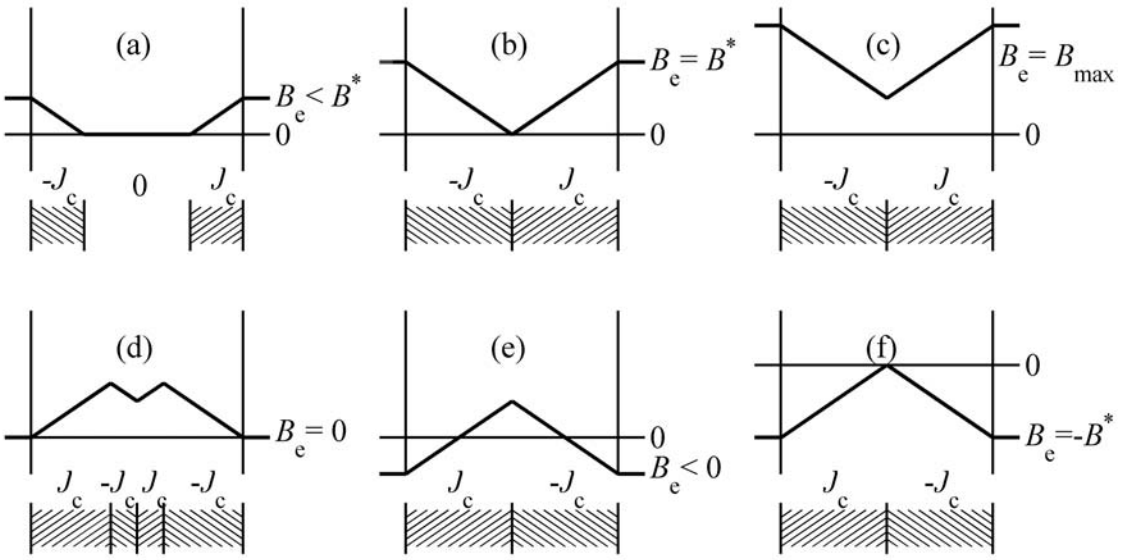

Figure 2.1: Magnetic flux penetration in an infinite superconductor plate in a parallel field B_e according to the Bean model. On top of each subfigure is the plate thickness B distribution and below it the thicknesswise current distribution. Shown are the B_e cycle from 0 to $2B^* > B_{max} > B^*$ and then down to $-B^*$. In (a), $B_e < B^*$ and increases to (b) $B_e = B^*$. In (c), a further field increase to $B_e = B_{max}$ increases only the magnetic flux density inside the plate but leaves the current distribution intact if B_{max} is less than B_{c2}. Lowering B_e starts to turn current directions first at the plate surface. At $B_e = 0$, as seen in (d), currents inside the plate are flowing and nonzero magnetic flux density distribution dependent on the B_e history remains inside the plate. (e) As B_e is increased in the negative direction, currents keep turning until at some B_e value they are fully turned. Further increase in the negative direction, as seen in (f), maintains the current distribution and changes only the B distribution same way as in the evolution from (b) to (c).

Power law approximation

The crystal lattice of all materials embodies thermal energy that makes the lattice vibrate, and naturally the vibrations are stronger at higher temperatures. HTS materials are operated at about 77 K, which is much higher than the 4.2 K typically used with LTS materials. At HTS operational temperatures, lattice vibrations are strong enough to occasionally dislodge a flux line from its pinning center. This so-called flux creep leads to a gradual relaxation of the flux line structure and hence to losses well below the J_c value. The losses show in the $V(I)$ measurement as a smooth voltage increase as opposed to the much steeper voltage rise in LTS materials. In modeling, this effect is taken into account by the so-called power-law approximation

$$E = E_c \left(\frac{J}{J_c} \right)^n ,$$

where J_c and the n values are defined by fitting them to a measured curve. The external magnetic flux density B_e decreases both J_c and n. Figure 2.2 compares the critical state model's steep $E(J)$ curve, characteristic of LTS materials, to the gradual increase seen in HTS materials.

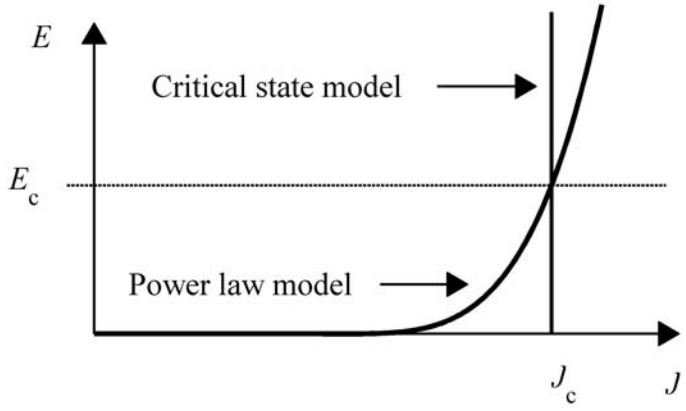

Figure 2.2: Comparison of the critical state and power law models. Ideal $E(J)$ curve based on critical state model is typical of LTS materials, where the change from superconducting to normal state is almost instantaneous and modeled with a high n value in the range of 20-100. In HTS materials and low quality LTS materials, the change between superconductive and normal states is more gradual and causes losses much earlier than indicated by J_c. Typically, the n values of HTS materials fall in the range of 10-30 though higher n values have recently been measured in YBCO tapes.

Magnetic field -dependent models

The Bean model's assumption of a constant J_c is not valid for real superconductors. In reality, the magnetic flux density dependence of J_c modifies the magnetic flux density penetration inside the specimen. The effect is modeled by several authors [2,47] and the so-called Kim model is given as:

$$J_c(B) = \frac{\alpha}{B + B_0},$$

where α and B_0 are constants fitted to the material's measured magnetic flux density dependence. Figure 2.3 gives further insight into the magnetic flux density distribution

inside the specimen if $J_c(B)$ is used. Since using $J_c(B)$ leads to nonlinear equations, and since we need numerical calculations to solve local magnetic flux densities inside the specimen, the Bean model is still used as the common basic approximation to estimate current density distributions inside specimens.

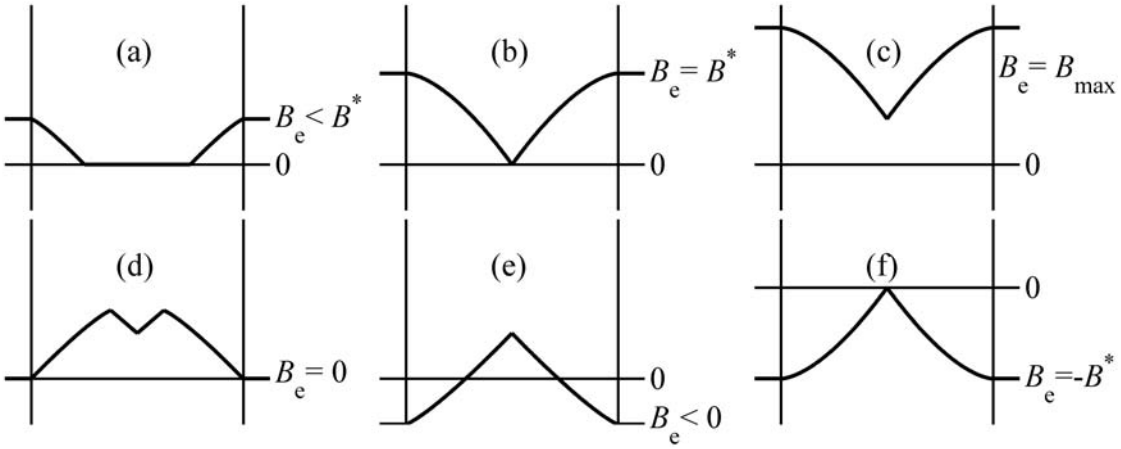

Figure 2.3: Magnetic flux penetration in an infinite superconductor plate in a parallel field B_e according to the Kim model. The current density inside the plate changes smoothly depending on the local magnetic flux density and is therefore not shown. The thickness B distributions shown are approximations to illustrate the two main effects of the Kim model: 1) Any given B_e penetrates deeper than it would in the Bean model and 2) the distribution of B inside the plate is non-linear. The B_e cycle from 0 to $2B^* > B_{max} > B^*$and then down to $-B^*$ is again assumed. In (a), $B_e < B^*$ and increases to (b) $B_e = B^*$. In (c), the field increases to $B_e = B_{max}$. Lowering B_e down to zero, as in (d), leaves B distribution and internal current to the plate dependent on the B_e history. (e) Currents keep turning inside the sample and at some $B_e < 0$ they are fully turned. (f) After further increasing the B_e in the negative direction, current distribution changes only slightly due to the increased B inside the sample.

The basic crystal lattice of HTS materials is anisotropic, a property that is reflected in the anisotropic magnetic field dependence of these materials. Figure 2.4 presents the crystal structure of Bi-2223 and names the lattice directions. The superconducting current flows practically fully in the so-called ab-plane of the crystal lattice, inside the CuO planes. HTS materials are typically granular and the supercurrent flows between adjacent grains only when the ab-planes of neighboring grains are highly parallel. Now that manufacturing seeks to ensure that the grains are carefully aligned, we are faced with the side effect that the HTS tape shows anisotropic magnetic flux density dependence. Because the ab-plane is parallel to the broad face of the tape, the magnetic field parallel to this face lowers J_c much less than the field parallel to the broad face normal. In the following chapters, β stands for the angle between the direction of B_e and the normal of the tape broad face.

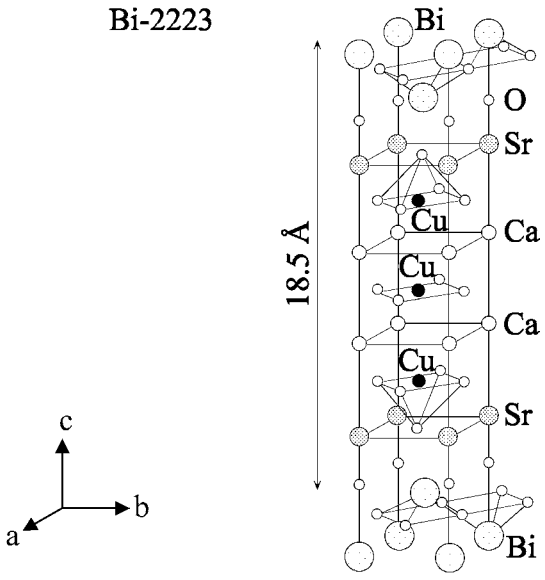

Figure 2.4: The crystallographic structure of Bi-2223

2.2 AC losses

AC losses in HTS specimens depend on several parameters such as material type, manufacturing process, specimen dimensions, the external field amplitude and orientation, the relative amplitude and the frequency of the transport current, local weak spots in the specimen, and the filamentary structure [28,62,63,64,72,100]. In general, the combined magnetic field caused by external fields and all the currents flowing in the specimen cause hysteretic losses because of the irreversible drag of magnetic flux line movement. Normally, hysteretic losses caused by the external field B_e are called magnetization losses, and losses caused by the AC transport current are called self-field losses, but the basis of these losses is the same. Multifilamentary tapes exhibit additional eddy current and coupling losses owing to their matrix metal and filamentary structure.

Calculation methods

Basically, losses per cycle, Q, are calculated with the following equation:

$$Q = \oint_{1/f} \frac{1}{\Omega} \int_{\Omega} \mathbf{E} \cdot \mathbf{J} \, \mathrm{d}\Omega \mathrm{d}t \,,$$

but in order to do so, we need to know the local electrical field **E** and current density **J** inside the whole specimen. The symbol Ω marks the integration volume, and f defines the

current frequency. Clearly, since neither **E** nor **J** can be measured directly without disturbing their distributions inside the specimen, a calculation model is used to define **E** and **J** inside the specimen.

Among other things, specimen inhomogeneities or a complex filamentary structure may lead to unpredictable current density behavior. To check whether the above conditions exist in a given specimen, we need some measurement data. Unfortunately, only a few methods yield measurement data on current distributions inside a specimen carrying AC current or in an external AC field to verify the models' assumptions. Therefore, the assumed models are typically simple, and theoreticians worry mostly about finding the type of unideality that causes the differences between calculation losses and measurements in each case. Such model inaccuracy often leads to pronounced differences, especially in the small current amplitude range. Quite often researchers exploit the Bean model and calculate hysteretic losses for different cross-sections, AC currents, or field amplitudes. Bean, Carr, Norris, and Wilson, among many others, have calculated the losses in various combinations of AC/DC fields/currents for basic cross-sections [8,16,56,58,69,75,77,98].

Measurement methods

There are two main classes of methods to measure AC loss: calorimetric measurement and electrical measurement methods. The calorimetric systems are frequently based on measurement of the boiling rate of the coolant (typically liquid nitrogen, LN_2, in the HTS case) and in some cases on temperature rise in the specimen during operation. These measurements reveal the total loss over a certain length of specimen, they are typically time-consuming, their resolution is somewhat limited, and they do not yield any information to help us distinguish between different AC loss components. On the other hand, the results are reliable with no problems to scale signal to losses [6,22,33,60,61,89]. In addition, local calorimetric measurements have also been proposed [7].

Electrical measurement systems allow us to separate the different loss components. Self-field losses are measured by the four-probe method on the specimen surface

[15,25,26] whereas magnetization losses are typically measured with a pick-up loop on the specimen surface [71,73,86]. After some preparation, the measurements are quick to make and their resolution is better than that of calorimetric measurements. On the downside, electrical measurements show a low signal to noise ratio and make it difficult to scale the signals correctly to AC losses. A few years ago, also systems for combined measurement of AC current and field losses were devised to mimic realistic applications [5,27,39,83,84,85]. Comparisons between calorimetric and electric loss measurement systems prove that both methods yield comparable results [23,59].

All the above loss measurement methods lack cross-sectional spatial resolution to help us understand where the problems and main AC loss sources occur in each specimen. Causes are determined based on the AC loss dependence in comparison to current/field frequency/amplitude, operational temperature, and other external parameters. To further optimize and understand the loss sources in each specimen, we need relatively simple and repeatable measurements to reveal as much as possible about current distribution and its evolution during an AC cycle. The measurement system should be simple to use, reliable, fast, and operable at 77 K, the temperature area of greatest interest and difficulties.

3 Hall magnetometer for AC currents

To examine the magnetic flux densities that currents inside the specimen cause, we need a measurement system capable of measuring such densities. This chapter introduces the structure of the AC Hall magnetometer and its auxiliaries, explains its operational principles, and scrutinizes some sources of error. In addition to static maps, the system is capable of measuring the magnetic flux density above HTS tapes during an AC cycle. All the magnetic flux density maps presented in the following chapters were measured with this system at 77 K. This chapter is based mainly on publication number 5.

3.1 The measurement system

Figure 3.1 below shows the flowchart of the alternating transport current Hall sensor magnetometer and its auxiliaries. The current source fed AC at an amplitude of I_{op} through the specimen in the magnetometer. A current transducer in series with the specimen was used to produce an analogue voltage signal following the alternating transport current.

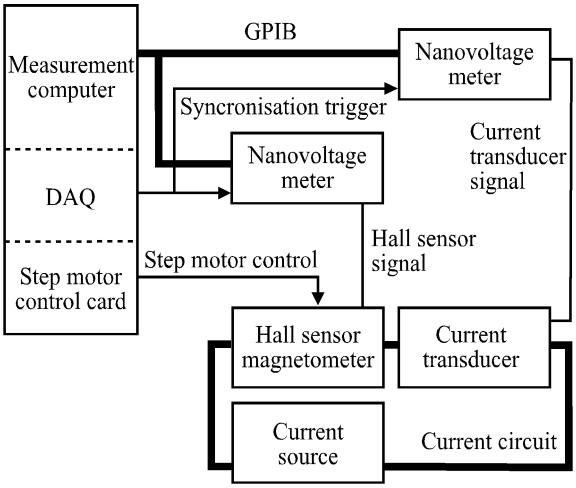

Figure 3.1: Flowchart of the alternating transport current Hall sensor magnetometer and auxiliaries. Thick solid lines mark the transport current circuit and GPIB. Thin arrows identify the trigger and step motor signals. Thin lines stand for Hall and current transducer signals.

The Hall sensor and current transducer signals were digitized with two synchronized voltage meters and transmitted to the measurement computer via the general-purpose interface bus (GPIB). Synchronization relied on the voltage meters' internal clock circuits and on an external trigger signal from the data acquisition card (DAQ). The computer also controlled the movement of the Hall sensor via three step motors. The measuring system was based on a three-axis Hall sensor magnetometer, constructed previously in our university [76].

The Hall sensor magnetometer

A Bi-2223/Ag tape specimen was attached to an epoxy specimen holder plate at the lower end of the cylindrical system holder, as seen in Figure 3.2. Because of its dimensions, the holder could take maximum 70 mm long specimens, though the specimen's measurable length was limited to 50 mm owing to the current transfer length demands. A current transfer length of < 1.0 mm at DC and ~1.5 mm at 50 Hz AC has been measured in silver sheathed tapes, but an alloyed sheath can further increase it [43]. Therefore, current transfer to superconducting filaments cannot be guaranteed before 5-10 mm from the current contacts.

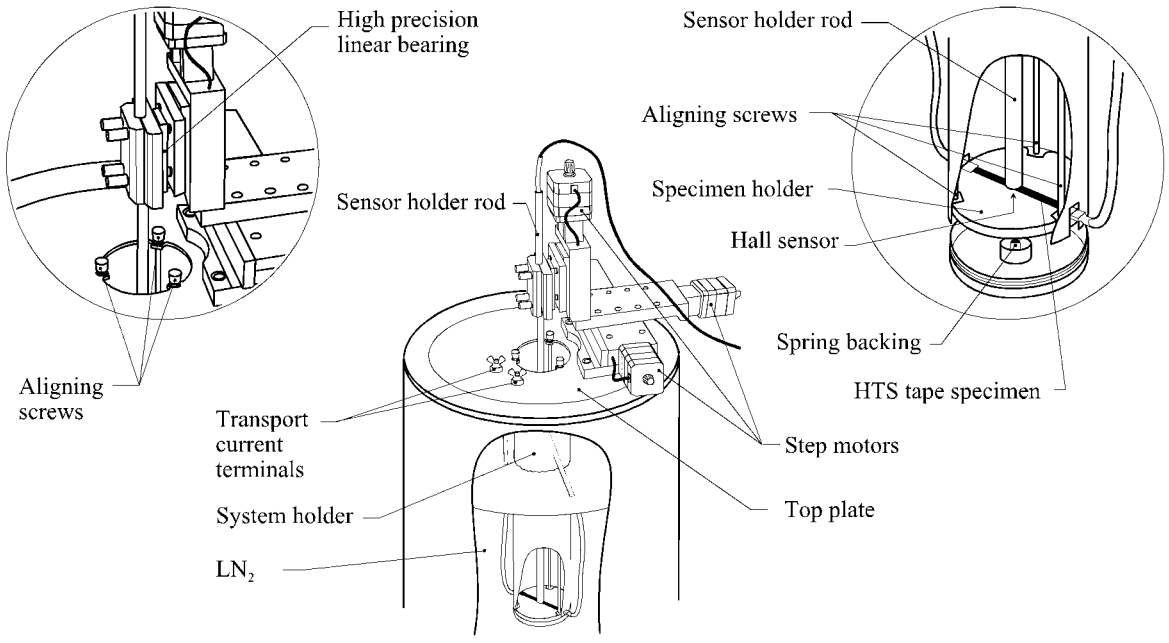

Figure 3.2: Structural sketch of the Hall sensor magnetometer. Dimensions not shown to scale.

The Hall sensor was attached to the lower end of a 300 mm long steel rod, where the last 40 mm were made of epoxy. The upper end of the rod was attached to step motors, which enabled 3D movement. During measurements, the specimen, specimen holder, and the lower end of the rod were immersed in LN_2. Because the magnetometer's upper part remained open, the measurement temperature was fixed at 77 K. We used a Hall sensor specifically designed for cryogenic temperatures and AC measurements with active area of 20 μm x 20 μm, DC excitation current of 5 mA, and sensitivity of 99.6 μV mT^{-1} in most Hall measurements presented in this thesis.

The system could map magnetic flux density in a desired set of spatial points caused by static or alternating current. Static current measurements were further divided into direct current measurements and remanent current measurements, which meant measuring the remaining magnetic flux density distribution after the transport current had been switched off.

3.2 Static current measurements

Preparation started by soldering one end of the specimen to a current terminal. Then to ensure that measurement was performed at a constant height, the specimen holder was leveled to the step motor plane by attaching a dial gauge in place of the Hall sensor rod. The dial gauge was moved manually on top of the specimen holder to measure the distance at several points along the holder edges. Differences were leveled out with three aligning screws and the spring backing of the specimen holder (see Figure 3.2). Next, the dial gauge was replaced with the Hall sensor, and the magnetometer was cooled by LN_2. After cooling, the other end of the Bi-2223/Ag specimen was attached to its current terminal with a screw clamp to avoid any tension to the Bi-2223/Ag tape by unmatched thermal contraction constants.

Measurement of DC magnetic flux density maps started by manually lowering the Hall sensor and by selecting the measurement height. Then the offset of the sensor was measured and recorded for later offset removal. The transport current was switched on, and the current density distribution was allowed to stabilize. Next, the transport current amplitude was measured, and the sensor was moved to the first intended spatial point with

the step motors to measure the Hall voltage. The procedure was repeated, with the transport current continuously on, at all the intended spatial points. Only the vertical component, B_z, was studied though also other components can be recorded with a 3D Hall-sensor. The transport current amplitude was measured at each point to verify its constancy, often it is measured only once and simply assumed to remain constant. The number of spatial points is restricted only by the computer's memory and time constraints. A typical measurement of about 400 spatial points takes roughly 15 minutes. The measurement of remanent magnetic flux density maps is otherwise the same, but the transport current is switched off after it has stabilized, and about 15-45 minutes are allowed before starting the measurement. Naturally, it is not necessary to measure the current amplitude.

In addition to measurements made above the specimen, the Hall sensor was also lowered down to the specimen surface, in which case the movement between the spatial points consisted of consecutive vertical and horizontal displacements of the sensor to avoid dragging the sensor on the specimen surface. A high-precision linear bearing with an adjustable stopper between the rod and step motors provided a fallback area for the rod and enabled a gentle contact with the specimen surface. The actual measuring distance from the specimen surface was 100-350 μm, which was the same as the thickness of the protective and insulating varnish layer on the sensor's active area.

Error sources and error analysis

The system's lateral spatial resolution was about 5 μm, caused by the long steel rod and the step motor resolution. Only visual estimation was made to fix the measurement's spatial origin in each map.

Constant and intended measurement height was ensured with horizontal leveling before cool-down, amounting to less than 0.03 mrad of leveling mismatch. The measurement height had an additional inaccuracy of about 50 μm, caused by manually fastening the sensor rod and by variations in its thermal contraction with the changing LN_2 level.

In this system, the practical magnetic resolution of the Hall sensor was about 50 μT, owing to signal noise, whereas its linearity error was typically < 0.2 % up to 1 T. The offset voltage varied slightly between each cool-down and was therefore recorded at each cooling; however, it did not exceed 250 μV. In several measurements the sensor was lowered to the specimen surface and a total mass of 300 g (Hall sensor, sensor rod, and linear bearing) rested on a specimen surface of 50 mm^2, equaling an average pressure of 60 kPa. This pressure was far too low to measurably affect the Bi-2223/Ag specimen's current carrying capacity [13,30] or the sensor voltage.

3.3 Alternating current measurements

The preparation of an AC magnetic flux density map did not differ from that of the DC map, nor the measurement of an AC magnetic flux density map up to the transport current switch on. After the waiting time, the transport current frequency, F, was measured. Before the measurement though, two parameters had to be decided on, samples per cycle, S_{PC}, and the number of cycles, C. An S_{PC} within range of 10-100 was selected, after which C was restricted by the maximum number of samples in the voltage-meters' memory, which was 5000. Then the Hall sensor was moved to its first intended spatial point, where the measurement computer sent an external hardware trigger signal to both meters and started their digitization sequence of N samples, in which N equaled S_{PC} times C. After the sequence was completed, all samples from both voltage meters were transferred to the measurement computer, and the Hall sensor was moved to the next spatial point.

The first voltage meter measured the Hall voltage as in DC measurement. The nth sample of the Hall voltage digitized at the mth spatial point was referred to as a voltage v_{Hmn}. The second voltage meter measured the signal produced by the high precision current transducer (CT) used to downscale the transport current in a ratio of 1500:1. The nth sample of the downscaled current was digitized at the mth spatial point as a voltage v_{Imn} over a precision resistance of R_p = 100 Ω. The actual sampling times of v_{Hmn} and v_{Imn} relative to the external trigger at all spatial points can be given as

$$t_{In} = (n-1)/(F \cdot S_{PC}), \tag{3.1}$$

if we assume exact sample timing and a zero trigger lag. Since the trigger signal was not synchronized with the current, any initial phase of the transport current, θ_m, was possible.

Error sources and error analysis

The accuracy of Hall voltage samples depends mainly on the digitization rate because it limits the time available for AD-conversion. In this system, the fastest digitization rate was 100 samples per cycle at a frequency of 400 Hz, which gave a minimum sample accuracy of 5.5 digits in the measurement range. With our Hall sensors, this translated into a magnetic field accuracy of 10 μT at a measurement range of 100 mV, but background, pickup, and measurement noise together lowered the magnetic field accuracy in the AC map to 100 μT. To quantify inductive voltages in the measurements, we duplicated several AC maps with the Hall current feed switched off. Typically, inductive components relative to the signal amplitudes were bigger in low I_{op} measurements than in over-current I_{op} measurements. Except for measurements made at 400 Hz, these inductive amplitudes were always below 5 % compared to the total signal level and were therefore omitted in the results.

The CT response time, verified with an oscilloscope, was 0.3 μs, which was 1.2 % of the sampling time of one sample at a maximum sampling rate of 100 samples per cycle at 400 Hz. The CT signal was compared to a signal measured through a power resistance at I_{op} of 20 A. Current changes of less than 100 A μs^{-1} could be followed, which ensured accurate digitization. The CT created a < 10 μA error in the downscaled current. For example, at I_{op} = 50 A, this error was < 0.03 %.

Synchronization between v_{Hmn} and v_{Imn} relied on the external trigger signal, delivered to both meters on the same signal lead. External trigger latency within the meters was < 175 ns with a jitter of < 50 ns. Between multiple meters, the trigger latency varied < 125 ns. Therefore, at the fastest rate of 100 samples per cycle and 400 Hz, the maximum total triggering error was < 1.5 % of the sampling time of one sample. Each voltage meter's internal clock had an insignificant, non-cumulative, sample-timing jitter of < 100 ps. In a long sampling sequence, a difference in the sampling frequency between meters can lead to a visible drift. To test this, a sinusoidal signal of 20 Hz and 400 Hz

from the signal generator were digitized using both voltage meters at ten readings per cycle over 500 cycles. The sampling frequency difference of < 0.9 mHz between the meters was measured at 20 Hz; at 400 Hz, it was < 17 mHz. During the 500 cycles, the frequency difference equaled a cumulative sampling mismatch of < 2.3 samples at 20 Hz and < 2.2 samples at 400 Hz. To keep the sampling mismatch error below one sample, we should have no more than 200 digitization cycles.

3.4 Reconstruction of the magnetic field density map

DC reconstruction is simple and straightforward: the sensor's offset voltage measured at the beginning of the measurement is subtracted from each Hall voltage, and the voltages are scaled to the magnetic flux density using the Hall sensor's sensitivity value. Then the scaled values are arranged according to their spatial coordinates, and a magnetic flux density map is drawn from the results.

Alternating current measurements

In AC reconstruction, we must, for each spatial point, find θ_m and the average cycle of the measured Hall voltage. After that, we can draw a measured magnetic flux density map for any desired current phase.

First, the digitized $v_{\mathrm{I}mn}$ is scaled to current $i_{mn} = 1500\, v_{\mathrm{I}mn} / R_{\mathrm{p}}$. Phases θ_m are found when each i_{mn} is fitted to the sinusoidal function

$$i_{mn} = A_m \sin\left(2\pi f_m \cdot t_{\mathrm{I}n} + \theta_m\right) + O_m ,$$

$t_{\mathrm{I}n}$ is defined by (3.1). At each point m, variations in the current amplitude, A_m, frequency, f_m, and offset O_m inform us about the stability of the current source. The first estimate of these parameters is calculated from i_{mn} with the discrete Fourier transformation, and the results are then used as a starting value for an algorithm based on Golden Section search and parabolic interpolation. The aim is to minimize the mean deviation $e_{m\mathrm{mean}}$ between fitted sinusoid and i_{mn}

$$e_{m\mathrm{mean}} = \sum_n \frac{\left| A_m \sin\left(2\pi f_m t_{\mathrm{I}n} + \theta_m\right) + O_m - i_{mn} \right|}{N}.$$

Table 3.1 shows details of an example AC measurements. Table 3.2 shows average A_m, f_m, and O_m values and their ranges for several AC maps.

Table 3.1: Details of an example AC maps, where f marks the alternating transport current frequency and I_{op} the alternating transport current amplitude. A varnish layer of thickness 0.35 mm must be added to the measuring distance to get the actual measuring distance. Samples per cycle and the number of cycles refer to Hall and transport current voltage digitization. The last column shows if the whole Hall signal (on) or only its inductive component (off) was measured.

AC map name	f (Hz)	I_{op} (A)	Measuring height (mm)	S_{PC} (pcs)	C (pcs)	Hall current
M1	20	50	0	100	50	on
M2	20	50	0	100	50	off
M3	20	150	0	100	50	on
M4	20	150	0	100	50	off
M5	50	50	0	50	100	on
M6	50	50	0	50	100	off
M7	50	50	0.4	50	100	on
M8	50	50	0.4	50	100	off
M9	50	150	0	50	100	on
M10	50	150	0	50	100	off
M11	100	50	0	30	150	on
M12	100	50	0	30	150	off
M13	100	150	0	30	150	on
M14	100	150	0	30	150	off
M15	400	50	0	20	250	on
M16	400	50	0	20	250	off
M17	400	150	0	20	250	on
M18	400	150	0	20	250	off

After all θ_m are found, a transport current phase is assigned to each digitized sample of i_{mn} as

$$\varphi_{mn} = \frac{2\pi f_m}{F \cdot S_{\mathrm{PC}}}(n-1) + \theta_m,$$

where φ_{mn} is the current phase of the nth sample at the mth point. If we assume ideal synchronization between $v_{\mathrm{H}mn}$ and $v_{\mathrm{I}mn}$, we know then the φ_{mn} of each sample n in $v_{\mathrm{H}mn}$ and

can calculate the Hall voltage that corresponds to any desired phase γ, $v_{\mathrm{H}m}(\gamma)$ at each spatial point with linear interpolation between samples. When we further assume all current cycles to be equivalent, we are in a position to re-create a measured AC map. If we digitize $v_{\mathrm{H}mn}$ and $v_{\mathrm{I}mn}$ over several cycles, C, we can average the corresponding Hall voltages $v_{\mathrm{H}m}(\gamma)$ from all the C cycles and reduce measurement noise and error caused by slightly varying current cycles. The average $v_{\mathrm{H}m}^{\mathrm{ave}}(\gamma)$ is calculated as

$$v_{\mathrm{H}m}^{\mathrm{ave}}(\gamma)=\begin{cases}\dfrac{1}{C}\displaystyle\sum_{k=0}^{C-1} v_{\mathrm{H}m}(\gamma+k\cdot 2\pi), \text{ if } \gamma \geq \theta_m \\ \dfrac{1}{C}\displaystyle\sum_{k=1}^{C} v_{\mathrm{H}m}(\gamma+k\cdot 2\pi), \text{ if } \gamma < \theta_m\end{cases}.$$

Table 3.2: Average frequencies $f_{\mathrm{ave}} = \mathrm{ave}(f_m)$, amplitudes $A_{\mathrm{ave}} = \mathrm{ave}(A_m)$, and offsets $O_{\mathrm{ave}} = \mathrm{ave}(O_m)$ as well as ranges $\Delta f = \max f_m - \min f_m$, $\Delta A = \max A_m - \min A_m$ and $\Delta O = \max O_m - \min O_m$ for several AC maps. Shown also are percentages of $\Delta A/A_{\mathrm{ave}}$ and $\Delta O/A_{\mathrm{ave}}$ with mean/max deviations $e_{\mathrm{mean}} = \mathrm{mean}(e_{m\mathrm{mean}})/A_{\mathrm{ave}}$ and $e_{\mathrm{max}} = \max(e_{m\mathrm{mean}})/A_{\mathrm{ave}}$.

AC map name	M1	M3	M5	M7	M9	M11	M13	M15	M17
f_{ave} (Hz)	20.00	20.00	49.99	50.00	49.99	99.99	99.99	399.99	399.99
Δf (mHz)	0.58	0.58	1.18	0.88	1.07	2.06	2.81	23.07	10.76
A_{ave} (A)	50.04	152.26	49.78	49.79	150.30	49.66	149.51	50.47	145.41
ΔA (A)	0.34	2.05	0.44	0.29	0.69	0.14	0.61	0.36	1.33
O_{ave} (A)	0.05	0.10	0.01	0.10	-0.01	0.00	0.09	-0.01	-0.01
ΔO (A)	0.08	4.22	0.05	0.14	0.26	0.03	0.91	0.02	0.21
$\Delta A/A_{\mathrm{ave}}$ (%)	0.69	1.35	0.89	0.58	0.46	0.27	0.41	0.71	0.91
$\Delta O/A_{\mathrm{ave}}$ (%)	0.16	2.77	0.10	0.27	0.17	0.06	0.61	0.04	0.15
e_{mean} (%)	0.68	0.82	0.72	0.58	0.68	0.66	1.04	2.18	0.80
e_{max} (%)	0.72	0.92	0.86	0.82	0.81	0.82	1.40	3.38	1.31

3.5 Chapter summary

This chapter introduced the Hall magnetometer together with its auxiliaries, capable of measuring magnetic flux density components above tape specimens that carry an alternating transport current at 77 K. The chapter also discussed signal and transport current flow between components as well as specimen preparation and the process of static and AC measurements. Furthermore, the chapter presented a post-processing algorithm to produce magnetic flux density maps at any desired current phase and to reconstruct DC and AC maps from measured data together with estimation of errors and their sources. Several example maps and their analyses showed that the system is capable of measuring magnetic flux densities caused by alternating currents in the frequency range of 0-400 Hz.

4 Inversion and direct methods

A calculation method is always needed to discover the current density that causes measured magnetic flux density maps. This chapter focuses on two common methods. First, it introduces briefly the inversion method and demonstrates statistically some of its characteristic problems. Besides many other fields [17,41], inversion is widely used to approximate the current density that causes measured magnetic flux density maps [10,40,45,80,81,92,97,99]. Second, it introduces briefly a direct, alternative method to test desired current density distribution. This simple and numerically stable method is used several times in the following chapters to verify assumed current density distributions inside a specimen. This chapter is based mainly on publication number 2.

4.1 Relation between magnetic flux density and current density

The basic relation between the magnetic flux density vector **B** in any place **r** and the current density **J** in volume Ω is expressed by the Biot-Savart law,

$$\mathbf{B}(\mathbf{r}) = \frac{\mu_0}{4\pi}\int_{\Omega}\frac{\mathbf{J}(\mathbf{r}')\times(\mathbf{r}-\mathbf{r}')}{\|\mathbf{r}-\mathbf{r}'\|^3}\mathrm{d}\Omega\,, \tag{4.1}$$

where μ_0 is the vacuum permeability, and **r**' is a position vector in Ω. Since, in our case, we know the magnetic flux density **B,** our target is to solve **J**.

For numerical computation, (4.1) must be discretized. **B** is inevitably recorded at discrete measurement points $\mathbf{r}_j$, $j = 1, 2, \ldots, N_\mathrm{M}$, where N_M is the number of points. The current density distribution is discretized by dividing the specimen volume into small elements. The problem is usually kept two-dimensional. Here we use a Cartesian coordinate system where the x-axis is parallel to the tape width, the y-axis parallel to the

tape length, and the z-axis parallel to the normal of the tape broad face. We assume that **J** is independent of y and present a $B_z(x)$ profile analysis with J_y assumed constant within each element. The discretization of the system leads to a set of linear equations that can be given in a matrix form

$$A\mathbf{J}_y = \mathbf{B}_z, \tag{4.2}$$

where A is the matrix dependent on the selected model geometry, $\mathbf{J}_y$ is the vector containing values of the current density J_y in the defined current elements, and $\mathbf{B}_z$ is the vector containing measured magnetic flux density values.

4.2 Inversion method calculations

The simplest form of inversion can be done if matrix A has an inverse. In this case, the solution $\mathbf{J}_y$ of (4.2) can be written as

$$A\mathbf{J}_y = \mathbf{B}_z \quad \Rightarrow \quad \mathbf{J}_y = A^{-1}\mathbf{B}_z,$$

where A^{-1} is just an inverted matrix A. Unfortunately, this works only for square matrixes and even then, as in our case, three simple but unavoidable practical limitations cause severe problems: nonzero measurement noise, numerical error by discrete numbers during computations, and modeling error owing to the difference between discretized model and real specimen. These three facts together with the task's numerical instability, caused by the long measuring distance compared to the desired spatial resolution, makes an accurate solution practically impossible.

Background of the statistical study

Because it is hard for even a trained mathematician to see the effect of the above three practical limitations in a mathematical context, we made a simple statistical study to demonstrate the numerical instability of the problem. The study was restricted to cases where A was a square matrix, that is, the number of the current elements equaled N_M. Now (4.2) provides a unique solution, which can be found with direct methods such as Gaussian elimination [21,99] or iterative methods like the fast Fourier transformation or

the conjugate gradient method [21,81,97]. The total error in computed results can be estimated by studying how much the problem's solution is disturbed if input data are disturbed as follows:

$$\left(A+\delta A\right)\hat{\mathbf{J}}_{\mathrm{y}}=\mathbf{B}_{\mathrm{z}}+\delta\mathbf{B}_{\mathrm{z}},$$

where δA and $\delta\mathbf{B}_{\mathrm{z}}$ are disturbances in A and $\mathbf{B}_{\mathrm{z}}$, respectively. $\hat{\mathbf{J}}_{\mathrm{y}}$ stands for the solution of the disturbed system and can be given as $\hat{\mathbf{J}}_{\mathrm{y}}=\mathbf{J}_{\mathrm{y}}+\delta\mathbf{J}_{\mathrm{y}}$, where $\delta\mathbf{J}_{\mathrm{y}}$ is the resultant error in $\mathbf{J}_{\mathrm{y}}$ [21]. The theoretical upper bound of the relative error in the output is obtained as

$$\frac{\left\|\delta\mathbf{J}_{\mathrm{y}}\right\|}{\left\|\mathbf{J}_{\mathrm{y}}\right\|}\leq\frac{\kappa\left(A\right)}{1-\kappa\left(A\right)\dfrac{\left\|\delta A\right\|}{\left\|A\right\|}}\left(\frac{\left\|\delta A\right\|}{\left\|A\right\|}+\frac{\left\|\delta\mathbf{B}_{\mathrm{z}}\right\|}{\left\|\mathbf{B}_{\mathrm{z}}\right\|}\right), \tag{4.3}$$

where $\kappa(A)=\|A^{-1}\|\,\|A\|$ is the condition number of matrix A [21]. Depending on the application, different matrix norms can be used to compute the relative error [31], the most common being the p-norms

$$\left\|\mathbf{J}_{\mathrm{y}}\right\|_{p}\leq\left(\sum_{i=1}^{N_{\mathrm{M}}}\left|J_{\mathrm{y}i}\right|^{p}\right)^{1/p},$$

where $J_{\mathrm{y}i}$ is the ith component of the vector $\mathbf{J}_{\mathrm{y}}$ and $1\leq p\leq\infty$.

In many cases, (4.3) gives too pessimistic a limit for the error [21]. If we know something more about δA and $\delta\mathbf{B}_{\mathrm{z}}$, we can analytically derive tighter error bounds than (4.3) [21]. Numerically, we can test the accuracy of (4.3) and gain detailed statistical knowledge about the true error distribution. We can then compare the different inversion methods without deriving specific error bounds for each individual method.

When inversion methods are applied to measured data, no accurate information is available about δA and $\delta\mathbf{B}_{\mathrm{z}}$, and since it is particularly difficult to isolate δA from $\delta\mathbf{B}_{\mathrm{z}}$, computational simulations are used here. In simulations, the current density distribution

inside a specimen model is fixed, and the magnetic flux density above the conductor is calculated. Now both the geometry of the specimen interior and $\mathbf{B}_z$ are known exactly, and various δA and $\delta\mathbf{B}_z$ can be introduced with $\delta\mathbf{B}_z$ to simulate noise in the measured signal and δA to contain the inaccuracies of the measurement point positions $\mathbf{r}_j$ and of the model geometry. Naturally, numerical round-off errors arise when the above methods are applied to simulated data.

Models for the statistical study

We used here only the standard matrix inversion method of Gaussian elimination with pivoting because comparing a host of methods would have gone beyond the scope of this thesis. The errors in the model geometry, δA, were set to zero to examine if we could reduce the inversion error by properly choosing $\mathbf{r}_j$. We varied the measurement height, h_m, and width, w_m, to find optimal $\mathbf{r}_j$ locations where the total error would be minimized.

We investigated two kinds of specimen geometries (see schematic view of model I in Figure 4.1). Variations of model I are widely used with inverse problems [40,92]. Measured data were simulated by assuming that a 1.0 A current flowed in each individual filament and was zero elsewhere. Furthermore, the filaments were of equal dimensions and rectangular cross-sections, and the distances between neighboring $\mathbf{r}_j$ were constants. Solutions were sought by varying N_M from two to 60 and the number of filament layers in the z-direction, N_L, from one to five. Model II imitated the filament structure of a real Bi-2223/Ag tape (see Figure 4.2).

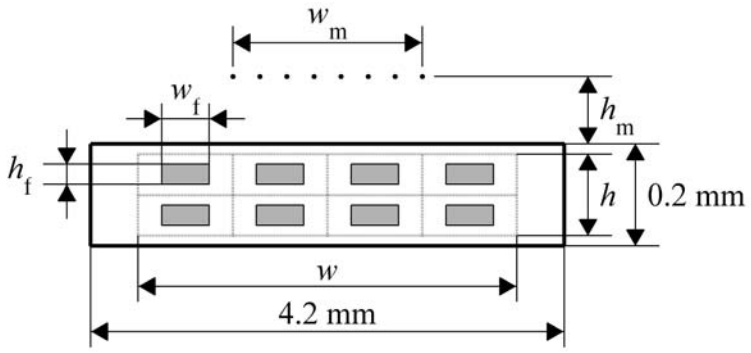

Figure 4.1: Schematic view of the cross-section of a model I.

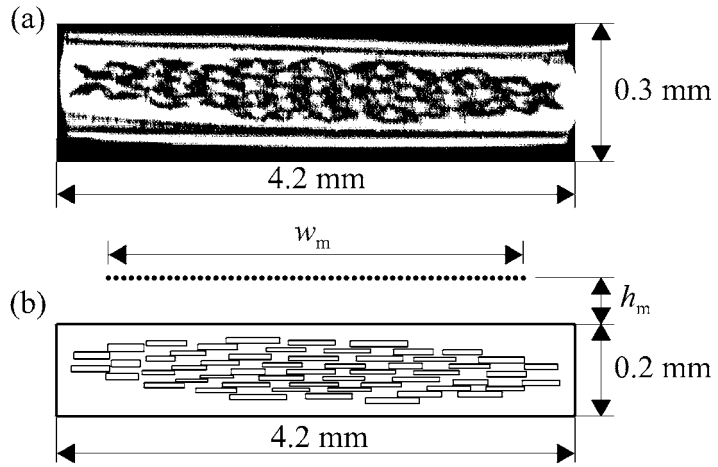

Figure 4.2: (a) SEM micrograph and (b) model II of a real Bi-2223/Ag tape manufactured by American Superconductor Corporation.

For both models, $\mathbf{B}_z$ was computed analytically according to [9]. A disturbance vector $\delta\mathbf{B}_z$ was added to the simulated data and inversion was carried out with the whole procedure repeated N_S times. The components of $\delta\mathbf{B}_z$ were normally distributed random errors.

Results of the statistical study

When δA is zero, (4.3) can be reduced to

$$e_B = \frac{\left\|\delta\mathbf{J}_y\right\|\left\|\mathbf{J}_y\right\|^{-1}}{\left\|\delta\mathbf{B}_z\right\|\left\|\mathbf{B}_z\right\|^{-1}} \le \kappa(A), \tag{4.4}$$

where e_B is the ratio of the relative error in currents to the relative error in measurements. Equation (4.4) assumes that the numerical error in the inversion equals zero. The results were computed by varying the standard deviation of the $\delta\mathbf{B}_z$ distribution, σ_B, between 2.5 μT and 12.5 μT. However, the average of e_B over all N_S simulations was practically independent of σ_B. Yet when σ_B exceeded 50 μT, overflows occurred in computation.

The condition number of matrix A increases when filament currents contribute in a similar fashion to the field at two or more measurement points; that is, when the rows in A become almost linearly dependent. For example, when the ratio of the filament dimensions to the corresponding unit cell dimensions, the so-called fill-factor $ff = N_M\, w_f\, (N_L\, w)^{-1} =$

$N_L\, h_f\, h^{-1}$ between 0 and 1, increases, the condition number increases. Figure 4.1 defines w_f, h_f, w, and h. So when *ff* increases, the filaments close on each other and become almost indistinguishable. However, $\kappa(A)$ is not necessarily a monotonously increasing function of *ff* because the relative positions of the measurement points to the filaments change with *ff*.

Figure 4.3 exemplifies typical density functions of an error e_B. Table 4.1 shows, with different norms, the expectation value, E_{eB}, standard deviation, σ_{eB}, the limits below which e_B remains with the probability of ε, $Y_{eB}(\varepsilon)$, and the condition number $\kappa(A)$. The expectation value is 3–9 % of $\kappa(A)$, and even $Y_{eB}(99.9\ \%)$ remains below 0.4 $\kappa(A)$. In general, $\kappa(A)$ gives a far too pessimistic error bound for the errors. The relative error is largest with the ∞-norm, which takes into account only the maximum error in individual filament currents, $\|\delta\mathbf{J}_y\|_\infty = \max(|\delta J_{yi}|)$. The distribution was computed with $N_S = 10000$, but the statistical parameters differed negligibly from $N_S = 1000$. In the following, the ∞-norm and $N_S = 1000$ are used unless stated otherwise.

Table 4.1: Parameters of error e_B distributions from Figure 4.3.

	E_{eB}	σ_{eB}	$Y_{eB}(95\ \%)$	$Y_{eB}(99.9\ \%)$	$\kappa(A)$
1-norm	26	17	59	92	920
2-norm	36	25	84	131	380
∞-norm	87	64	211	350	1850

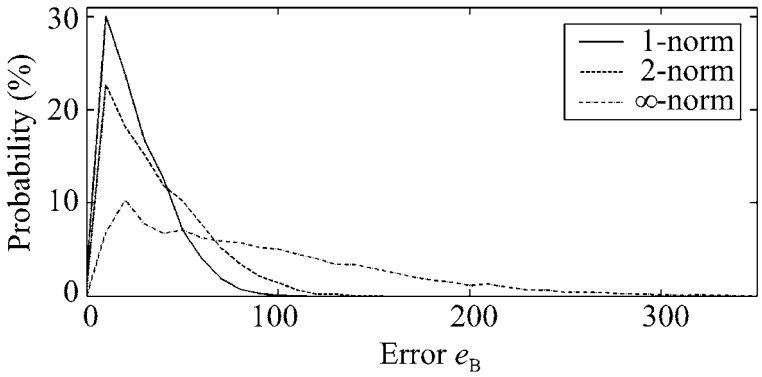

Figure 4.3: Density functions of e_B in a model having $N_M = 30$, $N_L = 1$, $h_m = 0.01$ mm, $w_m = 0.96\ w$, $ff = 0.5$, and $\sigma_B = 12.5\ \mu$T.

To minimize errors by proper choice of measurement points, we computed E_{eB} as a function of h_m and w_m. Figure 4.4 shows a typical $E_{eB}(h_m, w_m)$. A minimum occurred in $E_{eB}(w_m)$ at each h_m independent of the choice of N_M, N_L, and *ff*. When $\mathbf{r}_j$ were above the filament centers, the filaments became spatially distinct, but the B_z created by the nearest filament remained zero. Thus $E_{eB}(w_m)$ was very sensitive to the relative positions of filaments and measurement points. The error increased rapidly with rising h_m.

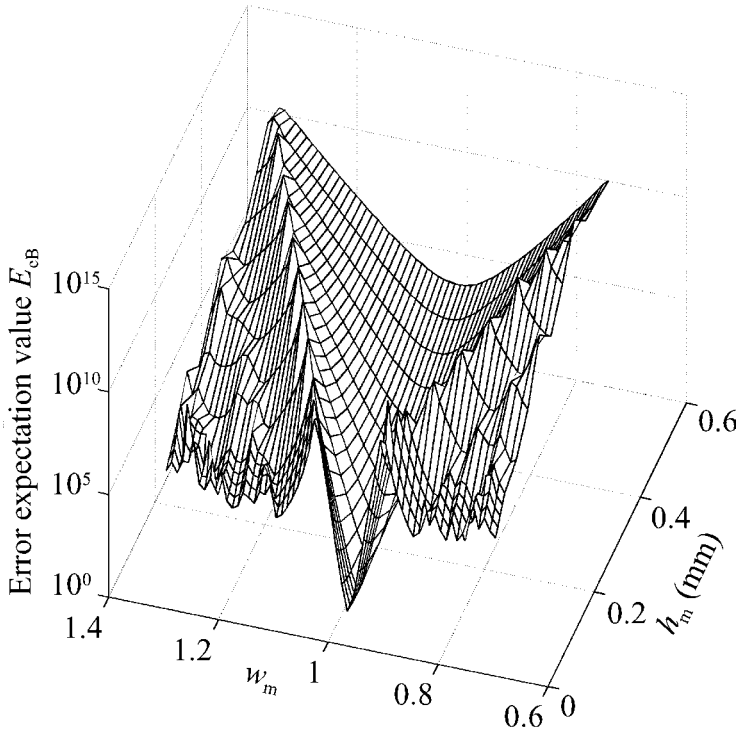

Figure 4.4: Expectation value of e_B as a function of measurement width and height when $N_M = 30$, $N_L = 1$, $ff = 0.5$. The w_m is normalized to the tape width w and h_m is given in millimeters.

We tested the numerical accuracy of Gaussian elimination by computing $e_{num} = \|\delta\mathbf{J}_y\| \, \|\mathbf{J}_y\|^{-1}$, when $\delta\mathbf{B}_z = 0$. A large e_{num} always coincided with a large e_B. The maximum of e_{num} in one filament layer calculations on model I was about 6 % with a geometry where $e_B \approx 10^{10}$; that is measurement error of $\|\delta\mathbf{B}_z\| = 10^{-11}\|\mathbf{B}_z\|$ can disturb the solution more than purely numerical inaccuracies can.

Figure 4.5 shows the $E_{eB}(N_M)$ dependence on the filament and layer number at $h_m = 0.5$ mm. Generally, E_{eB} increases rapidly with N_M and N_L. However, $E_{eB}(N_L = 2)$ is smaller than $E_{eB}(N_L = 1)$ when $N_M > 20$. This, together with the local peaks of E_{eB}, like at

($N_M = 12$, $N_L = 3$), were caused by the sensitivity of E_{eB} to the relative positions of filaments and measurement points. With $N_L = 4$ and $N_M = 60$ or $N_L = 5$ and $N_M > 50$, e_{num} exceeded 10%.

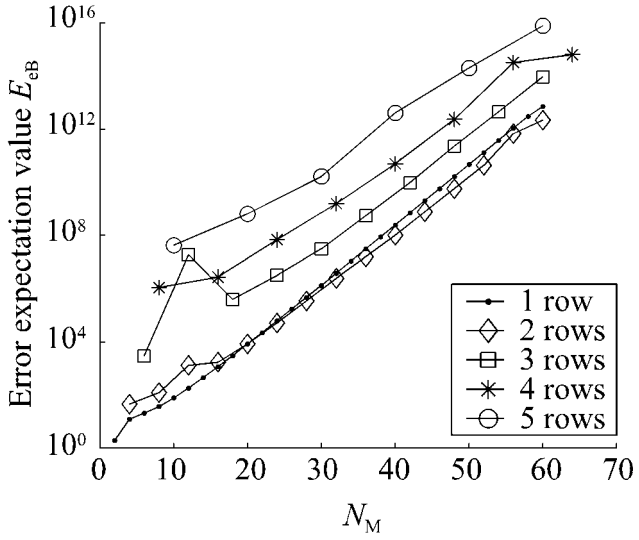

Figure 4.5: Expectation value of e_B as a function of the number of measurement points at N_L = 1, 2, 3, 4, and 5, when h_m = 0.5 mm, $w_m = w$, and ff = 0.5.

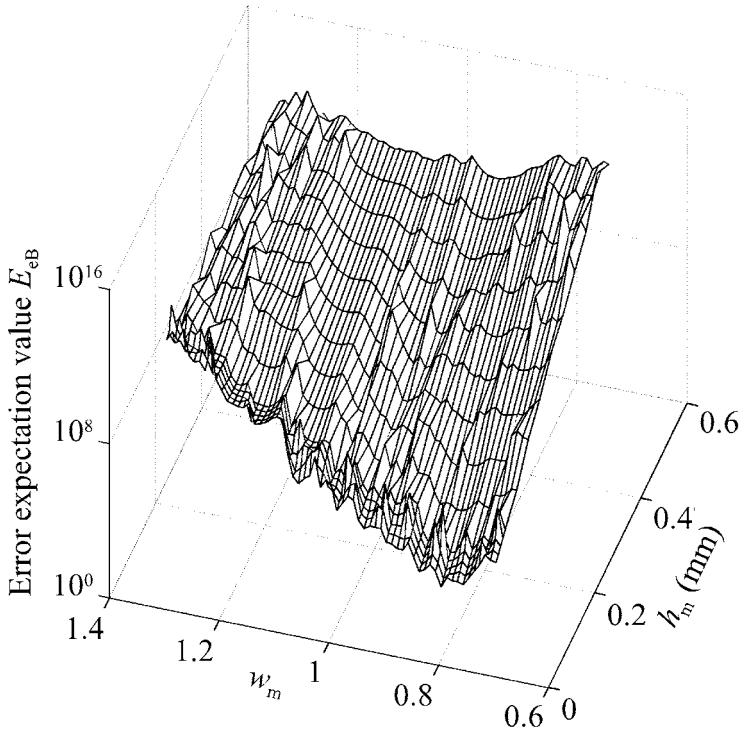

Figure 4.6: Expectation value of e_B as a function of measurement width and height for model II. The w_m is normalized to the tape width w and h_m is given in millimeters.

Figure 4.6 shows $E_{eB}(h_m, w_m)$ for model II. A minimum with respect to w_m is again seen near the point $w_m \approx 0.8\ w$. However, local maxima, typical of model I, do not appear, since no clear borders exist between the filament columns. Again, numerical errors coincided with large e_B, and e_{num} exceeded 10 % when $w_m > 1.2\ w$ or $h_m > 0.3$ mm. The error limit was reduced by several orders of magnitude through proper choice of $\mathbf{r}_j$, but the problem remained too sensitive for direct inversion. In this case, regularization methods could be of use [94].

4.3 Direct method calculation

A simple alternative to the demonstrably error-prone inversion method is the so-called direct method. In direct method calculation, a magnetic flux density caused by several feasible and probable current densities is calculated simply by using a numerically stable integration based on (4.1). In some cases, the calculation can even be reduced to simple analytical formulas [9]. When we then compare these calculated magnetic flux densities to a measured map, we can identify the assumed current density distributions that were closest to the real one. Typically, some kind of error minimization is used to find the closest solution in comparisons. Of course, the problem of poor resolution remains, which in this method means that countless current density distributions produce closely resembling magnetic flux density maps. The problem is there also in the inversion method, which yields no clear picture about the current density distribution. However, the direct method does not add huge, poorly traceable errors to the calculated magnetic flux densities and consequently, unlike the inversion method, needs no vaguely defined regularization parameters to exclude unphysical solutions [94].

4.4 Chapter summary

This chapter focused on the relation between current density **J** and magnetic flux density **B**. The relation was discretized in matrix format, and three practical limitations to discrete model inversion were discussed. Then the chapter embarked on the mathematical challenge of demonstrating the numerical instability caused by the above limitations by resorting to a simple statistical analysis. For basic Gaussian elimination, the statistical analysis gave more accurate error estimates than the condition number of matrix *A*. Therefore, this analysis can be used to accurately predict error limits for any given inversion method and to compare the accuracies of desired inversion methods. Furthermore, it turned out to be very difficult at the given measurement distance to distinguish currents flowing in filaments laid on top of each other. In the end, an alternative inversion method was adopted, in which the magnetic flux density caused by an assumed current distribution was calculated for several possible current distributions. Calculated and measured magnetic flux density maps could then be compared and the closest fit found for them.

5 Visible differences in measured maps

Major differences in current densities are also visible in measured magnetic flux density maps. In analysis, visual differences can therefore be used as a first estimate, for example, to check the homogeneity of the specimens. This chapter demonstrates and discusses several visual differences between magnetic flux density maps, first, differences between DC and AC maps and then effects visible around artificial defects. Finally, the chapter reviews some differences caused by different manufacturing and annealing processes. Sections 5.1 and 5.2 use specimens cut from the high homogeneity commercial tape presented in Figure 5.1, section 5.3 uses 20 R&D specimens presented in Table 5.1. The chapter is based mainly on publications 1 and 4.

5.1 Differences between static and alternating current maps

The Bi-2223/Ag specimens used in the measurements of this and next section were cut from a 55-filament Bi-2223/Ag tape with steel reinforcements and untwisted filaments, made by American Superconductor. Figure 5.1 shows the cross-section of the specimen. The critical current of these tapes was I_c = 145 A in a self-field (1 μV cm^{-1} criterion).

Figure 5.1: Cross-section of a 55-filament Bi-2223/Ag HTS tape specimen made by American Superconductor.

We used a 7-cm specimen for our measurements to determine differences between DC and AC maps of homogeneous specimens. DC maps of I_{op} = 50 A, 106 A, and 150 A, measured in contact with the specimen surface, are shown in Figure 5.2. At I_{op} = 50 A, the magnetic flux density concentrated at the specimen edges, and with an increasing current, the profiles penetrated the central area. The measurements were repeated at 0.4 mm above

the specimen surface. Now the signal amplitudes at the tape edges decreased by 25 % compared to the contact measurements. Furthermore, the profiles became flatter and the flux concentration at the specimen edges at I_{op} = 50 A is almost non-detectable. Thus, a 0.4 mm decrease in the measurement height led to a considerable information gain.

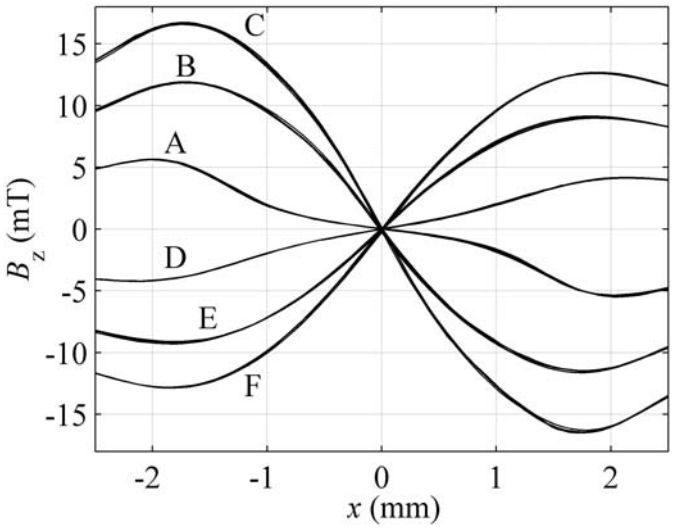

Figure 5.2: DC maps shown as cross-sectional profile sets of five profiles. Profile sets A, B, and C are from DC maps I_{op} = 50 A, 106 A, and 150 A, measured in contact with the specimen surface. Profile sets D, E, and F are corresponding DC maps from a distance of 0.4 mm, but with a current flow negative compared to profile sets A, B, and C to make it easier to distinguish between the sets.

Figure 5.3 shows three AC maps at six current phases. Profiles B in Figure 5.2 and 5.3 correspond to a current of 106 A. The comparison of profiles B between Figure 5.2 and 5.3 (a) shows clearly that with a direct transport current and at a corresponding momentary amplitude of 20 Hz alternating current, current density distributions must differ markedly because with the alternating current the magnetic flux concentrated much more at the sample edges. Figure 5.3 (a) and (b) illustrate the fact that flux penetration and thereby current density distribution must depend on the frequency of the alternating transport current. Finally, Figure 5.3 (c) shows that in a normal-conducting copper-tape, no flux-free region appears in the center though the electrical conductivity of copper is roughly eight times higher at 77 K than at room temperature. In simple terms, the difference between Figure 5.2 and 5.3 (a) as well as the differences between Figure 5.3 (a) and (b) suggest that there is a time dependent factor, the flux line lattice relaxation, that plays a significant role in current distribution. A comparison between Figure 5.3 (a), (b), and (c) stresses the fact that the cause must be something else than the simple skin effect

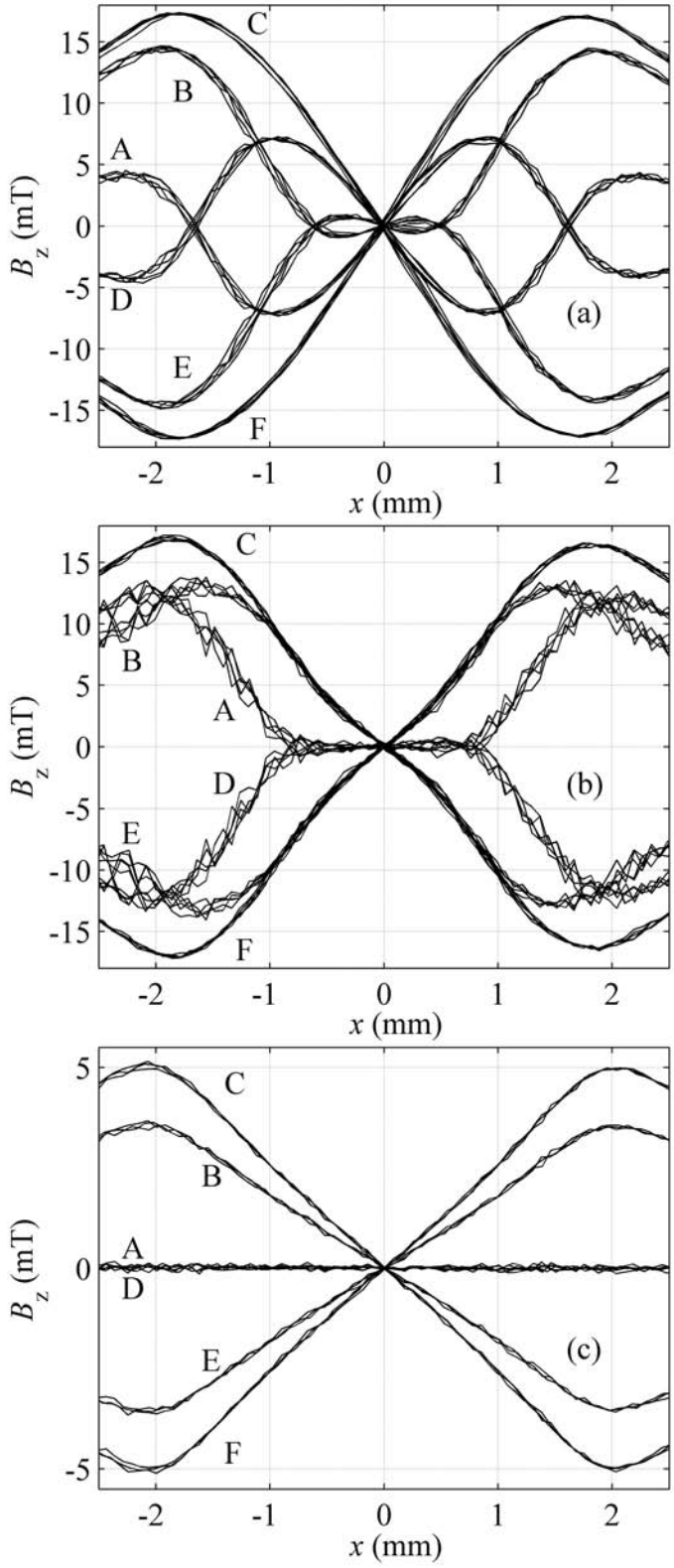

Figure 5.3: (a) Post-processed AC map at f = 20 Hz and I_{op} = 150 A (M3), shown as cross-sectional profile sets at six current phases of 0, π/4, π/2, π, 5π/4, and 3π/2 rad, marked as A, B, C, D, E and F, respectively. (b) Post-processed AC map at f = 100 Hz and I_{op} = 150 A (M13) at the same phases. (c) Post-processed AC map measured at f = 20 Hz and I_{op} = 50 A in contact with a 4-mm-wide copper tape at the same current phases.

of the resistive materials, the inductive component of the Hall sensor or simple measurement error. The effects of flux creep are discussed theoretically in [12,78].

5.2 Differences in maps around known defects

The behavior of the current around known defects was tested with two 7-cm specimens of 55-filament Bi-2223/Ag tape, M_{EH} and M_{CH}. A set of DC and AC measurements was made of these specimens to verify their lengthwise homogeneity; then artificial defects were created by drilling a ∅ 0.5 mm hole about 1 mm from the edge of specimen M_{EH} and the same size hole almost in the center of specimen M_{CH}. Measurements were then repeated to see the differences the holes may have caused. Figure 5.4 shows the locations of the holes relative to the specimen width of 4.2 mm.

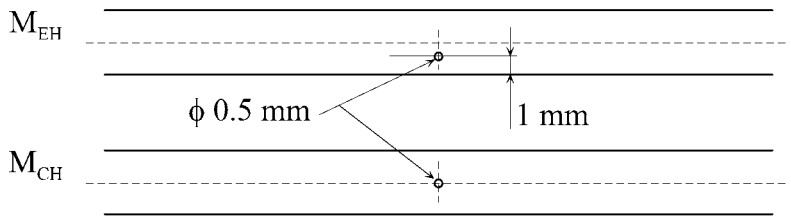

Figure 5.4: The location of the holes in the samples M_{EH} and M_{CH}.

Transport current amplitudes of 60 and 160 A were used to study the differences between DC maps at sub-critical and over-critical currents. Measurement of remanence maps was started 45 minutes after switching off $I_{op} = 160$ A. AC maps were measured with a transport current of $i_T(\theta) = I_{op} \sin(\theta)$, where I_{op} was 60 or 160 A and frequency 50 Hz. Three-dimensional magnetic field computations were used to test the validity of the claims made of the current density distribution in this section.

DC maps

Figure 5.5 shows the DC maps of both specimens after drilling. A meandering current created both a local maximum and minimum of B_z around the hole in each map. At sub-critical I_{op} currents, the current density J was highest close to the tape surface whereas inside the tape J was very small and appeared as a flat region where $\partial B_z / \partial x \approx 0$ in maps measured with $I_{op} = 60$ A (see Figure 5.5 (a) and (c)). Consequently, also the hole in M_{CH} is only weakly visible.

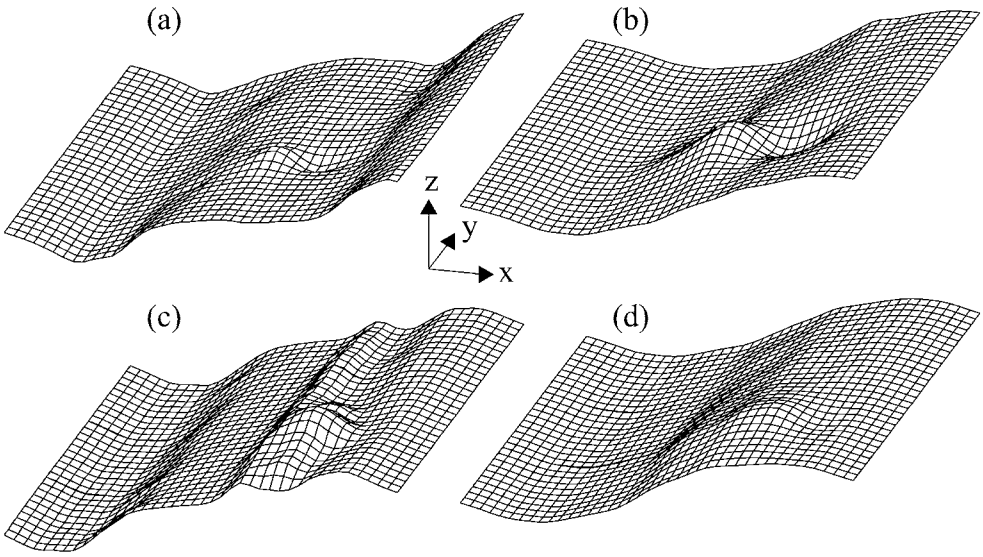

Figure 5.5: Measured DC maps: (a) M_{CH}, I_{op} = 60 A, (b) M_{CH}, I_{op} = 160 A, (c) M_{EH}, I_{op} = 60 A, (d) M_{EH}, I_{op} = 160 A. The current flows in the negative y-direction. *(In publication 1 there is a misprint on this caption, captions for figures (a) and (b) have changed places with (c) and (d).)*

When I_{op} is increased, the current penetrates deeper into the specimen, and the defect in M_{CH} becomes more evident as shown in Figure 5.5 (b). Specimen M_{EH} behaved exactly the opposite. At I_{op} = 60 A, the defect was conspicuous because of a local minimum of $B_z(x)$, which extended through the whole map in the y-direction. This suggests that at sub-critical currents, the current prefers energywise to flow straight in the inner filaments rather that meander through the matrix metal. Hence, only little current flows in the broken filaments.

At over-critical currents, J is high in the inner filaments, and, therefore, also broken filaments must be exploited in current transfer. At I_{op} = 160 A, the minimum of $B_z(x)$ vanished as shown in Figure 5.5 (d). In general, the results suggest that defects located close to the specimen edges are easier to detect by using sub-critical DC currents; on the other hand, defects close to the tape center are more visible with over-critical DC currents.

Remanence maps

When the DC transport current was switched off, the currents meandering through the silver died out rapidly, and only induced remanence currents flowed inside the filaments. The remanence maps shown in Figure 5.6 indicate that the local minima of B_z were created at the holes. The minimum can arise because the interaction of the

remanence current loops flowing in the filaments resembles a current loop around a hole. This loop has a direction opposite to the current loops inside the filaments.

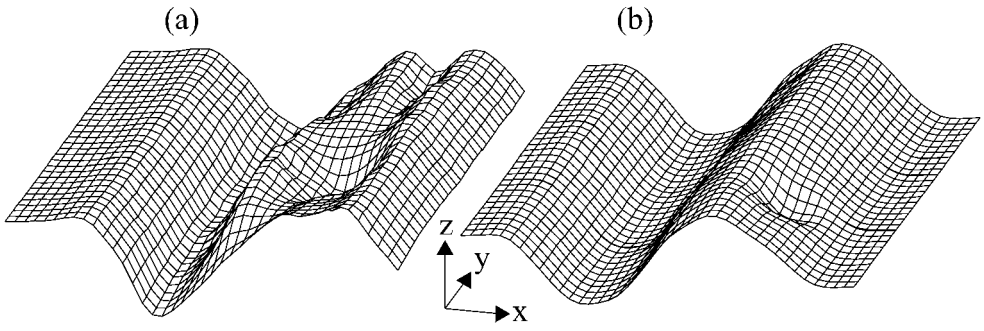

Figure 5.6: Measured remanence maps started 45 minutes after switching off a direct current of 160 A: (a) M_{CH} (b) M_{EH}. I_{op} flowed in the negative y-direction.

In specimen M_{EH}, the hole's effect on the remanence map was restricted to its immediate vicinity whereas the remanence map of M_{CH} had a local minimum of $B_z(x)$ similar to that in Figure 5.5 (c).

AC maps

Figure 5.7 shows AC maps of specimen M_{EH}, I_{op} = 160 A at transport current phases θ of 0, $\pi/4$, and $\pi/2$ rad. The phases correspond to an i_T of 0 A, 113 A, and 160 A. At $\theta = 0$ rad, $i_T(\theta) = 0$ A, but magnetization currents flowed in the specimen. Because the filaments were non-twisted, the multifilamentary specimen behaved like a monofilamentary specimen. Therefore, the magnetization current loop was not restricted inside one filament the way remanence current loops were [75].

The above caused the maxima of $B_z(x)$ in Figure 5.7 (a) to shift to the positive x-direction in contrast to the remanence maps. When $i_T(\theta)$ increased to 113 A at $\theta = \pi/4$ rad, magnetization currents contributed much less and, finally, at $i_T(\pi/2) = 160$ A, the current density flowed everywhere in the negative y-direction. In principle, when the transport current fully penetrates the tape cross-section at overcritical currents, then at the same current amplitude the AC map should resemble the DC map. However, the full-penetration current, I^*, and the I_c defined with the 1 μV cm^{-1} criterion are different in Bi-2223/Ag materials in that the higher the frequency, the higher the I^* [58]. In other words, at 50 Hz the current density close to the tape surface is higher than with DC current, therefore

changing also the current flow around the hole. In general, defects are less visible in AC maps than in DC maps. Furthermore, the higher noise in the AC measurement makes it more difficult to detect defects. However, the effect of holes on AC maps can be seen within 1.5 mm from the hole, an observation that coincides with the local voltage–current measurements by Polak *et al.* [82].

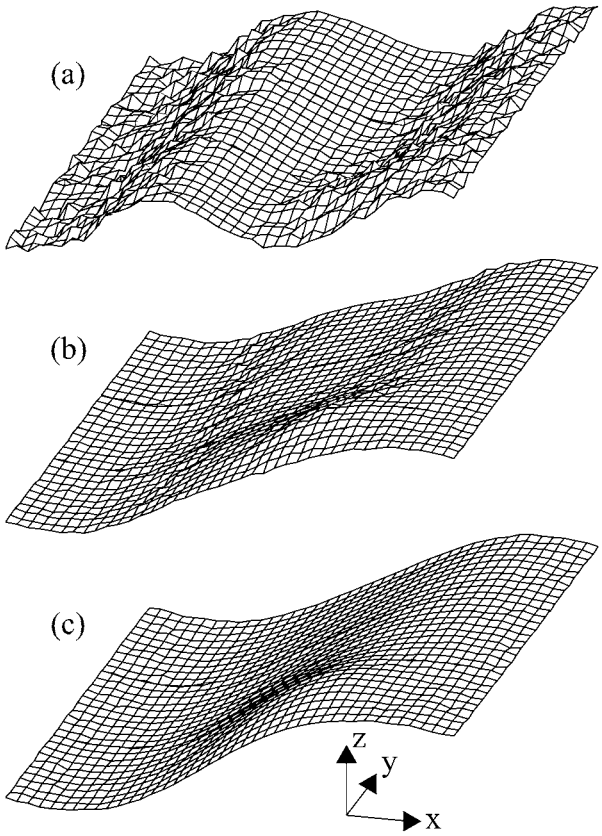

Figure 5.7: Measured AC maps in M_{EH} at I_{op} = 160 A and a frequency of 50 Hz: (a) $\theta = 0$ rad, (b) $\theta = \pi/4$ rad, and (c) $\theta = \pi/2$ rad. A positive current flows in the negative y-direction.

5.3 The benefits to the commercial tape manufacturers

To test whether manufacturing effects and different tape structures can be seen in magnetic flux density maps, we measured and analyzed a set of twenty Bi-2223 R&D specimens made by three different manufacturers. The main parameters appear in Table 5.1. The EAS Bi-2223 specimens A through G were manufactured by the Oxide Powder in Tube (OPIT) method [35].

The Nexans specimens were made by the OPIT method and mechanical deformations using two-axial rolling [36,48,49]. High mechanical strength was ensured with AgMg outer sheaths. Specimens I through K had also $SrZrO_3$ barriers around the filaments to increase their inter-filamentary resistance.

The FZK specimens were made by the OPIT method and all their specimens had $SrZrO_3$ barriers around the filaments (see [53] and the references therein).

Table 5.1. Properties of the specimens

Specimen	Manufacturer	Twist pitch (mm)	Tape width (mm)	I_c (A)	J_c (A mm^{-2})
A	EAS	straight	2.81	42.0	75
B	EAS	10.7	2.93	32.0	57
C	EAS	5.5	4.27	17.5	16
D	EAS	11.3	3.62	34.0	55
E	EAS	9.1	2.69	31.0	41
F	EAS	7.5	2.53	32.0	53
G	EAS	11.0	4.28	31.0	36
H	Nexans	straight	4.16	15.0	27
I	Nexans	straight	3.32	7.5	8
J	Nexans	8.0	4.24	10.0	9
K	Nexans	6.0	2.51	3.4	5
L	FZK	straight	3.32	19.2	23
M	FZK	40.0	3.40	15.5	19
N	FZK	20.0	3.38	15.2	19
O	FZK	10.0	3.40	18.5	24
P	FZK	9.0	3.36	13.1	16
Q	FZK	straight	3.45	16.0	19
R	FZK	40.0	3.31	14.0	18
S	FZK	20.0	3.34	15.9	20
T	FZK	10.0	3.35	13.5	17

DC maps

After comparing specimens A through G, we observed more inhomogeneities at the edges of wide specimens than on those of narrow specimens. The phenomenon is quite natural because the manufacture of a wide tape undergoes severe mechanical treatment, which may result in filament deformation and possible intergrowths at the tape edges. This effect is clearly visible in Figure 5.8 (b), specimen G. In its center, this map should have a

wider flat area than that in the map of specimen E in Figure 5.8 (a) because we used the same sub-critical current amplitude $I_{op} = 0.45\, I_c$ and because specimen G was wider. According to the measured map, the sub-critical current preferred to flow close to the center filaments in specimen G. In addition, the minimum and maximum of the map in Figure 5.8 (b) were wider and the map had irregularities, all of them serving as further indications of deformations in the outermost filaments at the specimen edges. The critical current was the same in both specimens. Even the twist pitch of the filaments could be detected. A twist pitch of 9.1 mm can be seen in specimen E in Figure 5.8 (a) as diagonal ridges advancing in the positive width direction with increasing length. Mainly the topmost filaments cause ridges. In a contour view, these ridges are distinguishable everywhere whereas on a surface like that in Figure 5.8 (a), they are best visible in the flat center area. Also in Figure 5.9, the twisted path of the topmost filaments in specimen J is well defined.

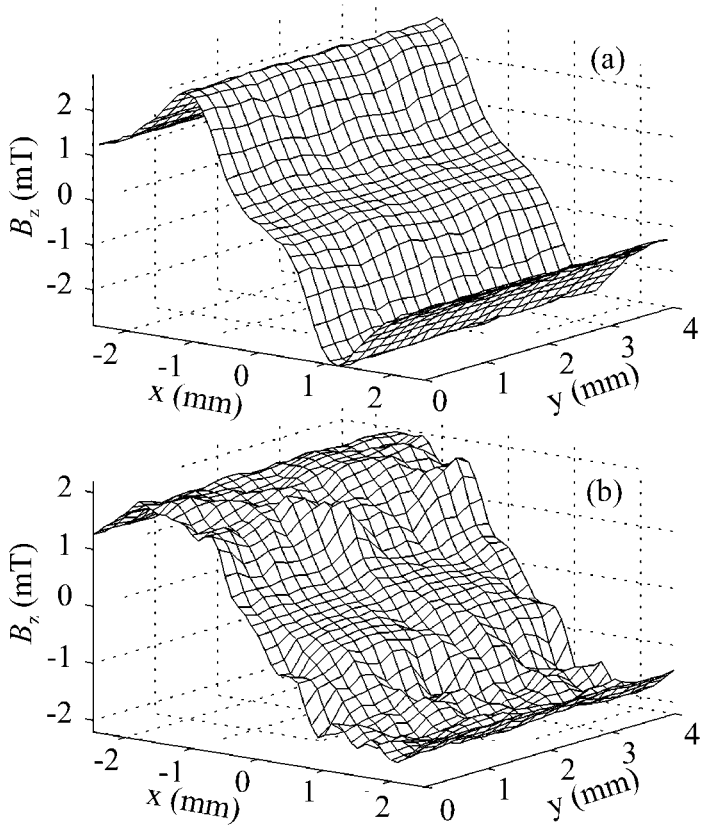

Figure 5.8: Measured DC B_z-map of (a) specimen E and (b) specimen G, both at I_{op} = 14 A = 0.45 I_c.

Specimen E was manufactured in nineteen steps of mechanical and heat treatment. According to Hall measurements, the homogeneity of the specimen was nearly perfect.

However, in specimen F only four steps produced homogeneity close to that in specimen E. Special attention was paid also to the symmetry of the measured profiles with respect to the tape center. For example, in specimen A, measured maps showed otherwise good homogeneity, but the current penetrated more rapidly from one edge than from the other, an asymmetry which had arisen during the heat treatment.

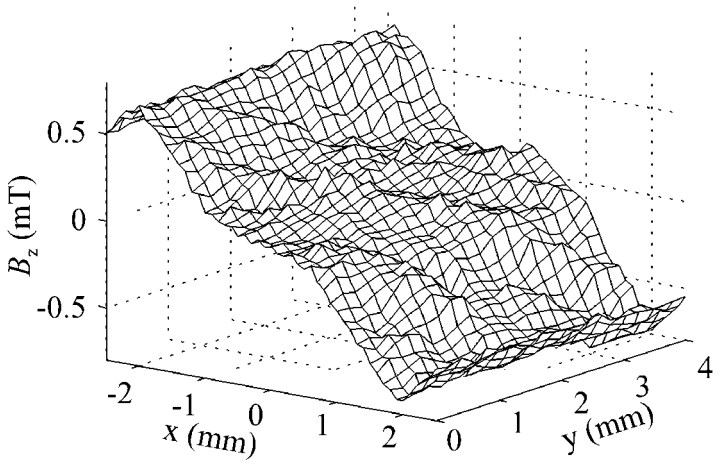

Figure 5.9: Measured DC B_z-map of specimen J at I_{op} = 5 A = 0.50 I_c.

Remanence maps

No matter how useful direct current B_z maps may be to tape manufacturers in deciding the nature and cause of inhomogeneities, the remanence maps are still the best indicators of small inhomogeneities. Figure 5.10 shows a remanence map of specimen E in the same location and even during the same cooling as the map in Figure 5.8 (a). Small

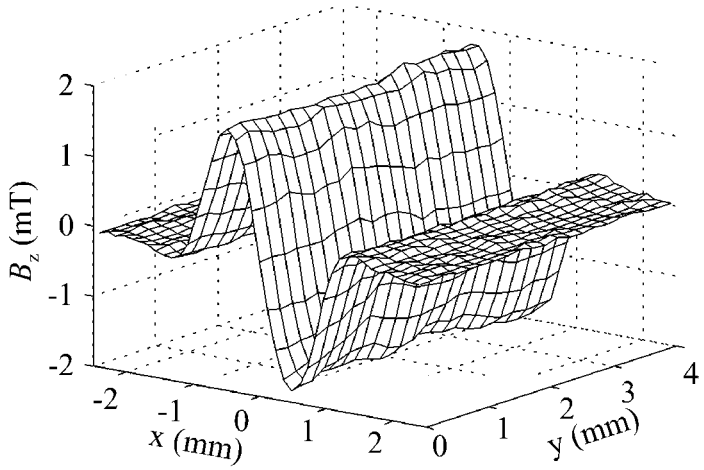

Figure 5.10: Measured remanence B_z map of specimen E.

lengthwise variations apparently related to twisting are visible at the remanence map's minimum and maximum though in Figure 5.8 (a) they are hardly visible.

AC maps

If I_{op} is much smaller than I_c, the flat area in the middle remains almost intact through the whole current cycle though the map's maximum and minimum change signs during the cycle. The change corresponds to the current flowing only in the outer filaments and changing their direction almost simultaneously with i_T. If I_{op} is roughly I_c, the current flow in the inner filaments is opposite to that in the outer filaments, a phenomenon that can be seen as an additional minimum and maximum in place of the flat area in the map, as in Figure 5.11. When the current phase is increased, the center area becomes first flat and finally a straight line, caused by the current in the inner filaments slowly turning to the direction of the current in the outer filaments. The current amplitude at which the flat area becomes a straight line gives an estimate of I^*. The width of the flat area and I^* are also frequency-dependent. In Bi-2223/Ag tapes, the full-penetration current is an important parameter defining the tapes' AC behavior [58]. We can obtain an estimate of I^* directly from measured AC maps by using the principle shown in Figure 5.11.

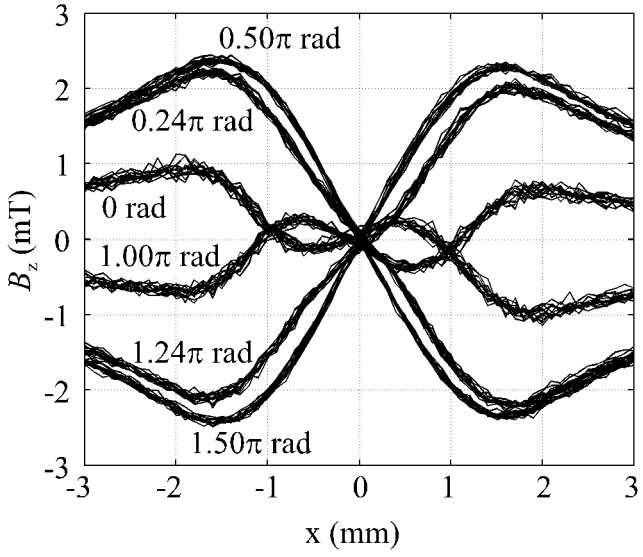

Figure 5.11: Measured AC B_z profiles of specimen L, 50 Hz at I_{op} = 24 A = 1.25 I_c, at current phases θ of 0, 0.24 π, 0.50 π, π, 1.24 π, and 1.5 π radians. Current phases 0.24 π and 1.24 π correspond to an I^* of 16 A.

5.4 Chapter summary

This chapter discussed briefly the differences between DC and AC maps and the effect of the measurement height. The **J** inside an Bi-2223/Ag specimen was shown to differ in both DC and AC modes from that inside a copper strip under an AC cycle.

Differences in the magnetic flux density caused by physical holes in various places in two Bi-2223/Ag specimens were tested, and the results showed that the current behaved differently in different I_{op} ranges. At low I_{op} values, the center hole was barely visible because it hindered hardly at all the current flow in the specimen. In the high I_{op} range, it did and was also much more visible. At the edge, the hole behaved in a contrary fashion because the high current amplitude forced all available filaments to carry current, even those damaged by the hole.

An extensive set of twisted and untwisted R&D specimens were tested, and the results showed that several types of defects and structures could be identified by comparing measured magnetic flux density maps. Generally, thin specimens had more defects at specimen edges and the twist pitches of the specimens could be detected from the maps. In addition, some problems were identified as being caused by heat treatment.

6 Comparison and combination of methods

The Hall sensor magnetometer is not the only method capable of providing insight into the current carrying capabilities of an HTS specimen. This chapter compares Hall sensor magnetometer (HS) measurements to magnetic knife (MK) measurements and seeks to underline advantages inherent in combining these methods. The chapter is based mainly on publication 6.

6.1 Magnetic knife

The MK, developed at the University of Twente, makes use of strong suppression of I_c in a perpendicular magnetic field to select a narrow slice of a Bi-2223/Ag tape for measurement [90]. Measuring is executed by applying over most of the tape width a B_z profile which is constant (and of sufficient amplitude), but which changes polarity sharply at $x = x_0$. Since the perpendicular field is relatively small in the region around $x = x_0$, the region corresponds closely to a measured I_c value. The field profile along the tape width is

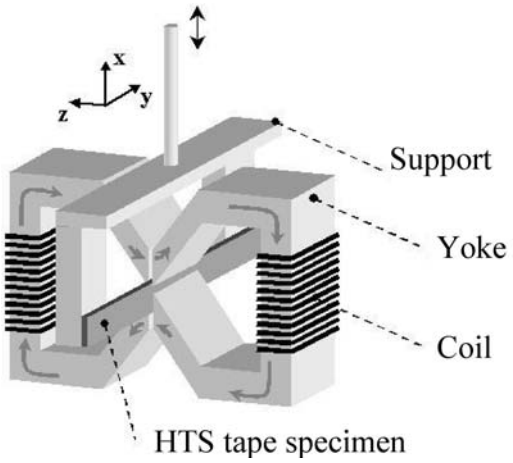

Figure 6.1: Schematic representation of the MK.

changed by moving the specimen through the gradient to measure the tape's $I_c(x_0)$-profile, see Figure 6.1. A local I_c is determined at regular position intervals of 50 µm using a standard four-probe technique. The critical current defined with a voltage criterion of 1 µV cm^{-1} is measured at 77 K in liquid nitrogen.

Analyzing the data requires several assumptions. First, the supercurrent is assumed to flow only in the y-direction (i.e., $J_x = J_z = 0$) while the critical current density J_c is assumed to depend only on the lateral position x ($\partial J_c / \partial y = \partial J_c / \partial z = 0$) and the local magnetic field $B_z(x)$. The field dependence of J_c is assumed separable from the position dependence, that is, $J_c(x, B_z) = J_{c0}(x)\, S(B_z)$ with $S(0) = 1$. When the magnetic field profile B_z of the magnetic knife is applied, the critical current $I_c(x_0)$ can then be expressed as an integral over the width W of the tape:

$$\begin{aligned} I_c(x_0) &= \int_{-W/2}^{W/2} h_{SC}(x)\, J_c\left[x, B_z(x - x_0)\right] dx \\ &= \int_{-W/2}^{W/2} h_{SC}(x)\, J_{c0}(x)\, S\left[B_z(x - x_0)\right] dx \end{aligned} \qquad (6.1)$$

where $h_{SC}(x)$ is the thickness of the superconducting structure at x determined from optical micrographs. This formulation ignores the self-field of the tape but makes use of the system-specific B_z distribution and the measured magnetic field dependence of the global J_c; the $h_{SC}(x)\, J_{c0}(x)$-distribution is calculated as deconvolution of the integral in (6.1) [90].

6.2 The measurements

The specimen used in these measurements was a 60-filament Bi-2223/Ag tape (cross-section shown in Figure 6.2) with a columnar filament structure made by the tape in rectangular tube (TIRT) process [48,49,50]. Short elements of this tape (50–70 mm) were analyzed with two techniques: Hall sensor magnetometer and magnetic knife.

Figure 6.2: Cross-section of a 60-filament Bi-2223/Ag tape of thickness 0.235 mm and width 4.05 mm.

Results

Magnetic field distributions above the tape were measured with HS at DC transport currents I_{op} of $0.36\,I_c \approx 9.4$ A and $1.13\,I_c \approx 29.3$ A. The measured B_z profile varied significantly along the specimen length, as shown in Figure 6.3. This variation reflects the non-uniform current density distribution inside the filament columns, likely caused by transverse cracks or other structural non-homogeneities. Sub-critical transport currents (Figure 6.3 (a)) showed these non-homogeneities more markedly than over-critical currents (Figure 6.3 (b)).

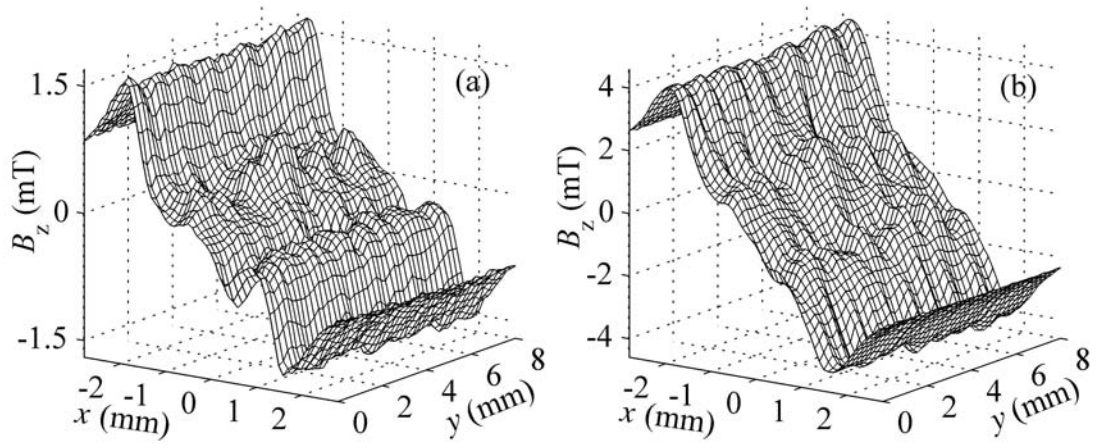

Figure 6.3: HS data of measured B_z distribution above the tape specimen at (a) $I_{op} = 0.36\,I_c$; (b) $I_{op} = 1.13\,I_c$

In over-critical measurements, the current could flow through the weak spots or silver, which made the B_z profiles smoother. The remanent state signal was of an order of 0.5 mT, which means that the remanent currents formed no large current loops within the filaments, as they do within homogeneous tapes. Local critical currents $I_c(x_0)$ measured with the MK over the tape specimen revealed clear maxima (corresponding to the positions of the filament columns) and minima (corresponding to the silver between them). The distribution of the critical current density $h_{SC}(x)\,J_{c0}(x)$ obtained by deconvolution of the measured $I_c(x_0)$ profile at $B_z = 0.25$ T is plotted in Figure 6.4. It is typical of sufficiently high MK field amplitudes (that is, $B_z >>$ self-field $\approx$ 5-10 mT) that the deconvolution result is essentially independent of B_z [90].

Comparison of the $h_{SC}(x)\,J_{c0}(x)$ profile with the $h_{SC}(x)$ estimate (light grey area in Figure 6.4) obtained from the cross-section in Figure 6.2 reveals that the $J_{c0}(x)$ values in the central filament column are systematically lower than those in the two side columns. This observation correlates well with the stress-strain pattern of the applied rolling deformations, which showed better texture in the outer columns [51,79].

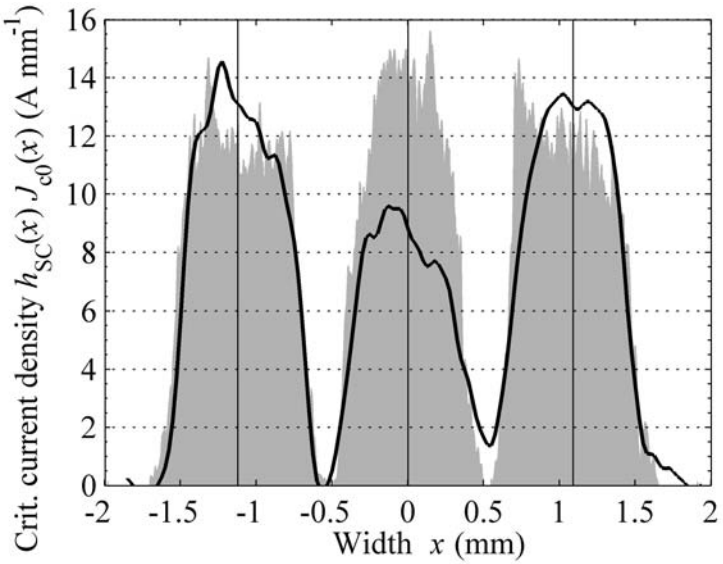

Figure 6.4: Deconvoluted critical sheath current density $h_{SC}(x)\,J_{c0}(x)$ calculated from $I_c(x_0)$ distribution measured at 0.25 T. The light grey area represents the relative superconductor content in arbitrary units of the specimen determined from Figure 6.2. The three solid vertical lines represent the centers of the filament columns, as determined from Figure 6.2.

6.3 Comparison and combination of HS and MK

Though both experiments yield some information on inhomogeneous current flow in the tape, they impose specific boundary conditions in terms of the magnetic field (MK of applied field; HS of self-field). A direct comparison of the data can therefore be only qualitative. However, to compare the results of these experiments in a semi-quantitative manner, we would do well to relate them to model calculations. In the section below, variations in the current carrying capacity in the (lateral) x-direction are modeled with 2D calculations whereas variations on the tape's xy-plane require 3D models such as those used in the section after the one below.

$J_c(x)$ variations

$B_z(x)$ can be calculated analytically by assuming that the current density J flows straight through the specimen's cross-section (that is, $J_x = J_z = 0$) [9]. Such 2D computations were carried out to illustrate the current sharing between filament columns and to compare the results of magnetic knife and Hall probe scanning.

B_z profiles were studied in four cases. A transport current of $1.13\,I_c$ was studied because at overcritical currents $J_y(x)$ variations result only from the specimen's inhomogeneous current-carrying capacity, not from its magnetic history. In case I, we assumed a single rectangular current-carrying zone with its dimensions shown in Figure 6.5 (a). $I_{op} = 29.3$ A was evenly distributed over the zone's cross-section. In cases II and III, three rectangular zones (modeling the three filament columns) were assumed, as shown in Figure 6.5 (b). In case II, the currents flowing in all the three zones were equal, that is, $I_1 = I_2 = I_3 = I_{op} / 3$. In cases III and IV, the currents were defined after the magnetic knife measurements. The zone currents I_1, I_2, and I_3 in case III were directly proportional to the columnar maximum values of $h_{SC}(x)\,J_{c0}(x)$ shown in Figure 6.4, that is, $I_1 = 0.39\,I_{op}$, $I_2 = 0.25\,I_{op}$, and $I_3 = 0.36\,I_{op}$. In case IV, the current flowed again in one filament, but the current density $J_y(x)$ varied according to the $h_{SC}(x)\,J_{c0}(x)$-distribution in Figure 6.4. Hence $J_y(x) \propto J_{c0}(x)$ and

$$I_{op} = 1.13\int_{-W/2}^{W/2} h_{SC}(x)\,J_y(x)\,dx .$$

The B_z of the self-field generated by these four current distributions was calculated at a measurement height of 250 µm used in the HS experiment. In Figure 6.6, the computed B_z profiles are compared with the range of measured HS profiles of Figure 6.3 (b). The three separate filament columns are clearly visible because the local minima and maxima of the measured $B_z(x)$ are located on the columns' boundaries. When we used the filament column dimensions shown in Figure 6.5 (b), the computed minima and maxima were located in the same positions as the measured minima and maxima. The computed profiles fit well within the range of the measured values. The best agreement was achieved in case II. Detailed comparison between cases II (currents identical in all three zones) and

III (current varied from zone to zone) suggests that in the HS experiment the current was evenly divided between the zones—contrary to the results of the MK measurements,

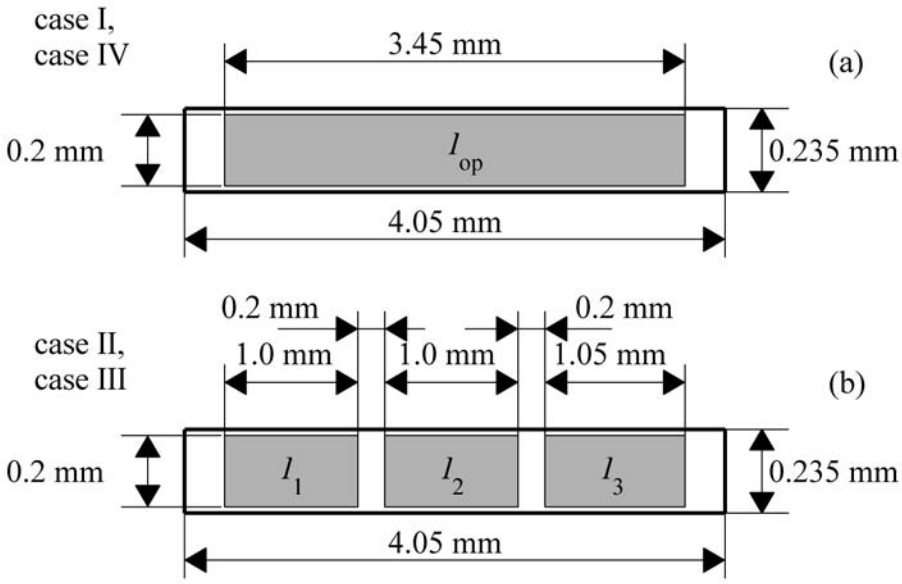

Figure 6.5: Cross-sectional geometries used in 2D model calculations: (a) one-zone model used in calculation cases I and IV; (b) three-zone model used in calculation cases II and III.

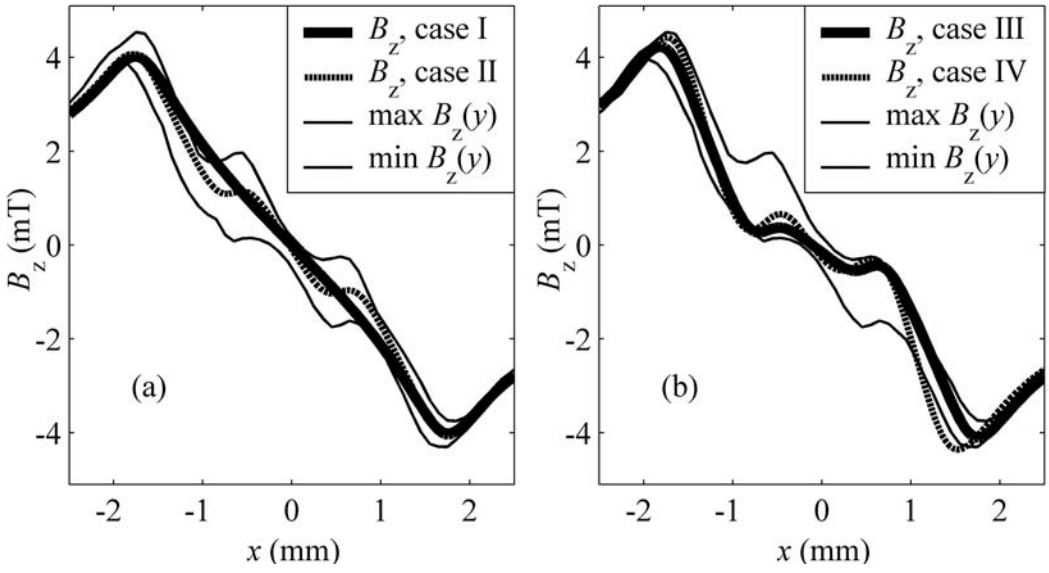

Figure 6.6: (a) 2D calculated B_z profiles for cases I and II; (b) 2D calculated B_z profiles for cases III, and IV at I_{op} = 29.3 A. Maximum and minimum of the HS measured $B_z(y)$ from Figure 6.3 (b) are shown for comparison.

which show a strong variation in $J_{c0}(x)$. However, this does not mean that either the HS or MK results were false. Rather, we must take into account two essential differences in the experiments: (1) the details of the $B_z(x)$ profile and (2) the validity of the $J_x = 0$ assumption. The first has to do with the effect of the $J_c[B_z(x)]$-dependence on the measured transport current distribution $J_y(x)$. According to the MK measurements, J_{c0} was lowest in the center column, but in this method the magnetic self-field barely affected the current distribution. On the other hand, in the HS experiment, $B_z(x)$ was fully determined by the self-field. There, $B_z(x)$ was close to zero in the specimen center while the current was less dense at the tape edges where the self-field was higher and oriented along the z-direction. In other words, in the HS experiment the specimen carried a sizeable transport current throughout its cross-section, causing the current density to be more evenly distributed than the $J_{c0}(x)$ measured with the MK.

The second difference between HS and MK involves a possible meandering of the current in the xy-plane. In the MK measurement, the applied $B_z(x)$ profile forced the current to flow in the y-direction by effectively cutting off J_x components on a scale of 100 μm [90]. In a 'global' transport experiment, such as the HS, the current seeks to circumvent possible weak spots, which means a local increase in current density at one or both sides of any weak spots. These differences illustrate that HS and MK measurements should not be seen as competitive techniques, but rather as complementary measurements that can be combined to examine possible current variations in the lateral and longitudinal direction.

$J_c(x, y)$ variations

Meandering of the current, as discussed above, cannot be modeled with 2D calculations but calls for a more sophisticated approach. Three-dimensional computations, run on an OPERA 3D post-processor, which solves the magnetic field by numerical integration of the Biot–Savart law [9], were performed to explain the variation of $B_z(y)$ above each filament column (see Figure 6.3). First, we inspected the possibility that some filaments in the columns of Figure 6.5 (b) may have been damaged, causing the current to meander vertically inside a filament column, but we detected no visible variation in the computed B_z maps because the thickness of the column was only 0.2 mm. Then we

examined the currents meandering horizontally (in the xy-plane) inside the specimen. Three typical cases are shown in Figure 6.7: intergrowths between the columns, intra-columnar meandering, and variable column width. In addition to the current flowing straight through the columns, periodically meandering currents were used, as shown in Figure 6.7. In this figure, as well as in the following discussion, symbols I_1, I_2, and I_3 refer to the current components in filaments 1, 2, and 3 that flow strictly in the longitudinal y-direction. The symbol I_{12} marks the current flowing between columns 1 and 2, and I_{23} marks the current flowing between columns 2 and 3. Symbols I_{11}, I_{22}, and I_{33} mark meandering currents inside columns 1, 2, and 3. Since the sample current causing Figure 6.3 (b) was clearly highly inhomogeneous, finding the optimal current amplitudes would have been too demanding task for the present model and inversion softwares. Therefore, the current amplitudes used in Figure 6.7 were determined after few trials on different amplitudes and do not present any optimal solution to the problem. The map shapes computed using these currents are presented in Figure 6.8.

Figure 6.8 (a) shows a computed map over a specimen with intergrowths. In the center of the specimen (about $x = 0$), the shape is similar to that of the measured one shown in Figure 6.3 (b). The amplitude of the $B_z(y)$ variations agrees quantitatively with the highest measured variation when currents via intergrowths are about 1.0 A. However, over the outer boundaries of the superconductor, the $B_z(y)$ variation is hardly visible, in contrast to the measured behavior. In Figure 6.8 (b), the $B_z(y)$ variations caused by currents meandering inside columns are seen over the columns' interior; however, over the column edges, that is, at the local maxima and minima of $B_z(x)$, the variation is negligible. Each current flows from one side of the column to the other and back. Finally, Figure 6.8 (c) shows the effect of changes in the column width on the B_z maps. This model showed good agreement with measurements at the tape edges in that the amplitude of $B_z(y)$ variations agreed quantitatively with measurements when the meandering currents were $I_{11} = I_{22} = 1.0$ A and $I_{33} = 0.5$ A. However, in the tape center, Figure 6.3 (b) agreed better with Figure 6.8 (a) than with Figure 6.8 (c). None of the studied models alone could produce a map like the measured one. Consequently, the map was most likely produced by a combination of different types of defects in the real specimen.

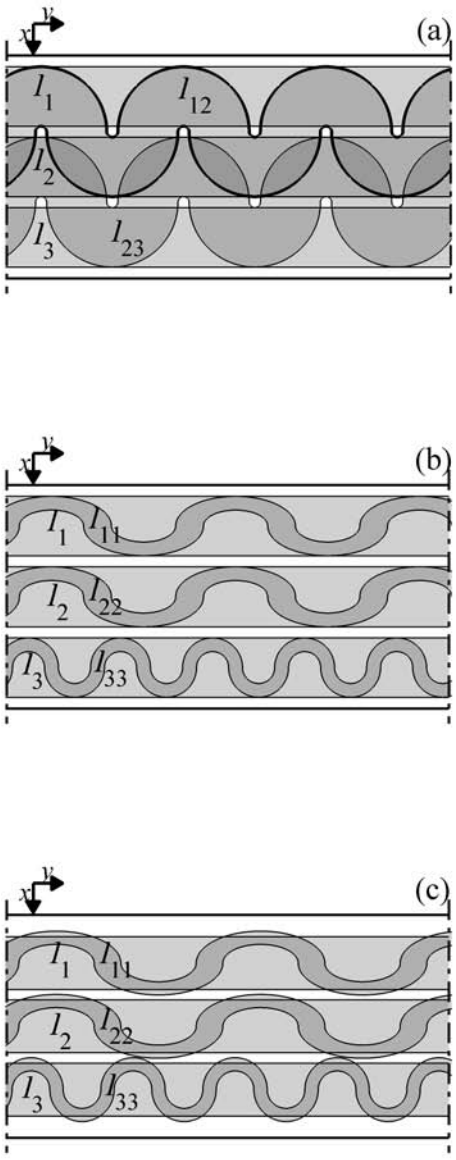

Figure 6.7: Scheme of in-plane current flow in 3D magnetic field computations. In all cases, the thickness of the current paths is constant, 0.2 mm. For simplicity, all filament columns, i.e., straight current paths, have equal widths. The specimen width is 4.05 mm and the visible specimen length is 8 mm; all other dimensions are to scale. The currents are (a) $I_1 = I_2 = I_3 = 9.1$ A, $I_{12} = I_{23} = 1.0$ A; (b) $I_1 = I_2 = I_3 = 8.4$ A, $I_{11} = 2.0$ A, $I_{22} = I_{33} = 1.0$ A, and (c) $I_1 = I_2 = I_3 = 8.9$ A, $I_{11} = I_{22} = 1.0$ A, $I_{33} = 0.5$ A.

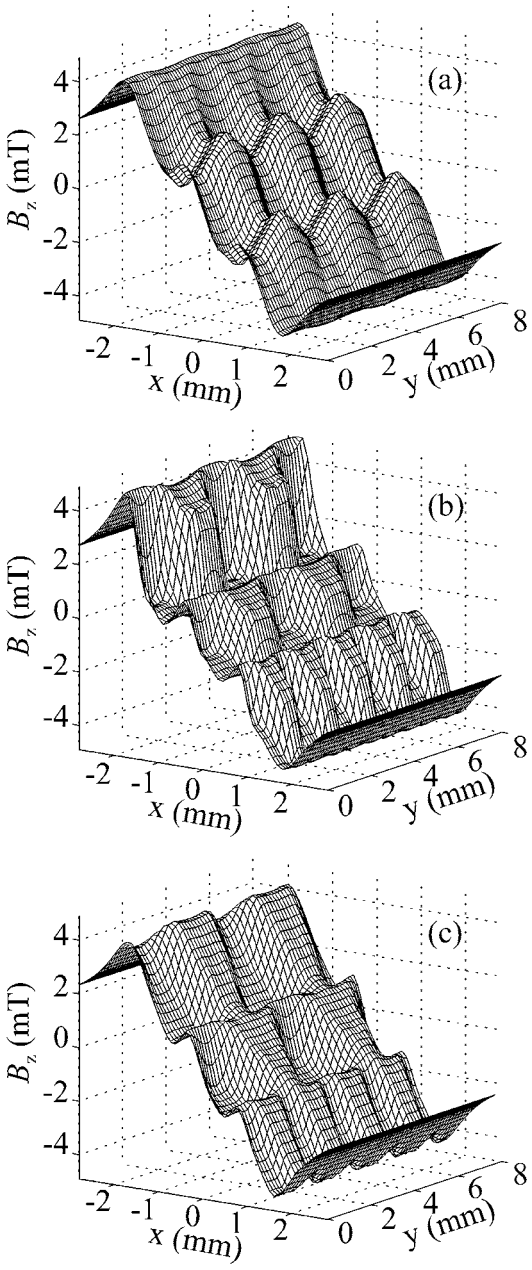

Figure 6.8: Typical $B_z(x, y)$ shapes from 3D calculations assuming (a) columnar intergrowth currents; (b) intracolumnar meandering; (c) lengthwise column width variation

6.4 Chapter summary

This chapter introduced the basic operational principle of the MK and showed how HS and MK measurements should not be seen as competitive techniques, but rather as complementary measurements that can be combined to examine possible current variations in the x and y-directions. For example, the MK may diminish the current meandering inside the specimen, which affects the measured critical current distribution. In addition, the MK suppresses self-field effects, which may be seen in the critical current distribution. Variations in the tape's cross sectional capacity to carry current in the y-direction were modeled with 2D calculations and by 3D models in the tape xy-plane. No one model alone could produce a map like the measured one, which may have resulted from a combination of different types of defects.

7 Current distribution calculations

Finally, we discuss two cases of calculating current densities that cause measured magnetic flux density. First, we focus on the evolution of current density during a standard $V(I)$-measurement; here calculation is based on the local magnetic flux density dependence of the material properties. Second, we examine the evolution of current density during an AC cycle and test a penetration model thereof. For the most part, this chapter is based on publications 3 and 7.

7.1 Current distribution during current-voltage measurement

Normally, a material's $E(J)$ characteristics are derived by dividing the I by the superconductor's cross-sectional area and the V by the distance between the voltage taps. This assumption of a constant J is an oversimplification because the quality and quantity of the superconducting material as well as the magnitude and orientation of the magnetic flux density, $\mathbf{B}_s$, created by the transport current, vary inside the specimen. Changes in $\mathbf{B}_s$ can also induce screening currents in the specimen. In this section, Hall-sensor measurements and numerical computations are used to estimate the evolution of the current density distribution $J_y(x, z)$ inside the tape during a $V(I)$ measurement.

The specimen and measurements

The American Superconductor tape, presented in section 5.1, was used in measurements. The voltage–current characteristics of a short specimen were measured at 77 K with a standard four-point method at several external magnetic flux density, $\mathbf{B}_e$, amplitudes and directions. Because at low external fields the self-field causes a clearly visible reduction in I_c and n, two specimens were connected in antiparallel to compensate for self-field [57,88]. The compensated $I_c(\mathbf{B}_e = 0\ \mathrm{T})$ was 180 A compared to 145 A in the uncompensated measurement. Figure 7.1 is a compilation of the I_c and n values in the

compensated self-field and uncompensated external field measurements, the curves being hereafter referred to as $I_c(\mathbf{B})$ and $n(\mathbf{B})$ characteristics.

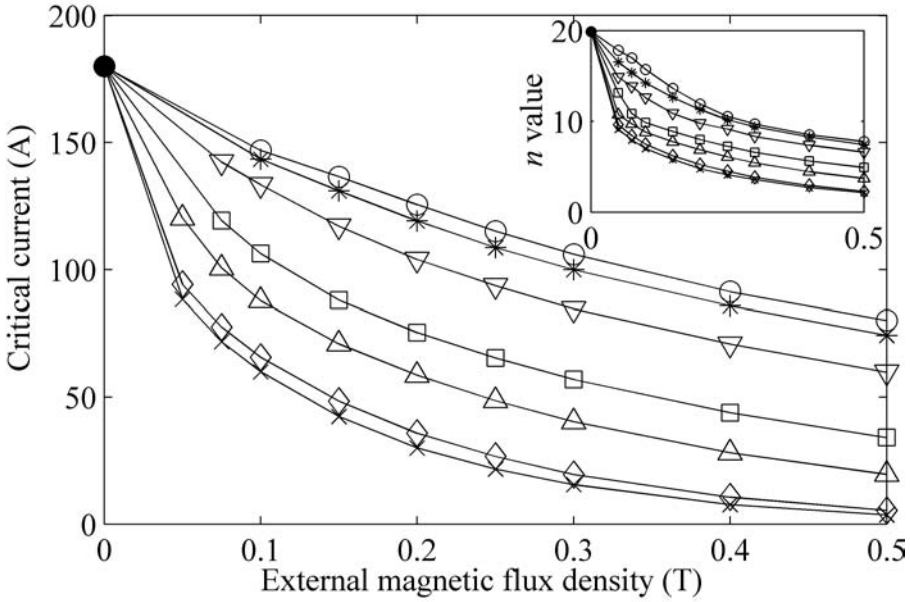

Figure 7.1: I_c as a function of the external magnetic field B_e in different directions: (×) β = 0°, (◊) β = 30°, (Δ) β = 60°, ( ) β = 70°, (∇) β = 80°, (∗) β = 85°, and (O) β = 90°. (•) marks I_c(0 T) from a compensated measurement. Inset shows the corresponding n values.

To study the changes in the current density distribution as the current amplitude rose from sub-critical to over-critical values, we used a Hall sensor magnetometer to measure B_z profiles over a specimen carrying a DC transport current. First, we used the I_{op} values of 66, 91, 115, 148, and 170 A, but because the profile changed considerably between 66 and 91 A, we measured later also I_{op} values of 68, 70, 72, 74, 76, and 78 A to map this evolution.

Computational model

We computed the effect of the self-field on the current density distribution, and in the current density distribution (CDD) model used a power law approximation for $E(J)$ characteristics. In CDD computations, the y-directional current density distribution $J_{CDD}(x, z)$ that fulfils the condition

$$E(x,z) = E_c \left[\frac{J_{CDD}(x,z)}{J_c\left(\mathbf{B}(x,z)\right)} \right]^{n\left(\mathbf{B}(x,z)\right)} = E_0$$

at each point inside the tape was searched with an iterative algorithm based on finite element method [68]. $E_c = 1\ \mu V\ cm^{-1}$ is the electric field criterion, and E_0 is a given constant defining the total current through the specimen. In the CDD model, $J_c(\mathbf{B})$ and $n(\mathbf{B})$ characteristics are assumed to be location independent, which is a valid assumption if the superconductor is homogeneous, and if the material is evenly distributed over the specimen cross-section. In this case, $J_c(\mathbf{B})$ characteristics can be calculated as $I_c(\mathbf{B})$ divided by the superconductor's cross-sectional. The $n(\mathbf{B})$ characteristics can be used as such. The B_z profile over the tape surface caused by $J_{CDD}(x, z)$ was calculated using Biot-Savart's law [9].

As discussed in Chapter 4, the current density distribution inside the tape can be solved from measured magnetic flux density profiles, but no method can uniquely solve this inverse problem without additional assumptions. One simple method is least squares fitting (LSF), where the tape cross-section is divided into N_J current elements in the x-direction. With N_M measurement points of the magnetic field B_z, the dependence between the element currents and the B_z can be written in the matrix form $A\mathbf{I} = \mathbf{B}_z$, where $\mathbf{I}$ is the vector containing the currents I_j of each current element $j = 1, 2, \ldots, N_J$, and $\mathbf{B}_z$ is the vector containing the measured magnetic flux densities B_{zi}, $i = 1, 2, \ldots, N_M$. In general, $N_M > N_J$, and the least squares method yields $\mathbf{I} = (A^T A)^{-1} A^T \mathbf{B}_z$. Here we used LSF with $N_M = 91$ and $N_J = 10$.

Results and discussion

We studied the evolution of $J_{CDD}(x, z)$ with increasing transport current using the CDD model at $E_0 = 100\ fV\ cm^{-1}$, $100\ pV\ cm^{-1}$, $10\ nV\ cm^{-1}$, $1\ \mu V\ cm^{-1}$, and $10\ \mu V\ cm^{-1}$, which correspond to computed transport currents I_{op} of 66, 91, 115, 148, and 170 A. At $E_0 = E_c$, the computed current 148 A agreed well with the critical current 145 A measured on a single tape. In computations, the self-field reduces the n-value from 21.5 determined at $66\ A \le I_{op} \le 91\ A$ to 16.6 determined at $148\ A \le I_{op} \le 170\ A$. The n value calculated from the $V(I)$ curve can be higher than the n value of the material at zero field since the self-field increases during measurement and steepens the $V(I)$ curve. Figure 7.2 shows the $J_{CDD}(x, z)$ inside the tape at $I_{op} = 148$ A. The calculational tape width used in this section was 3.9 mm to compensate for the current free silver matrix outer layer.

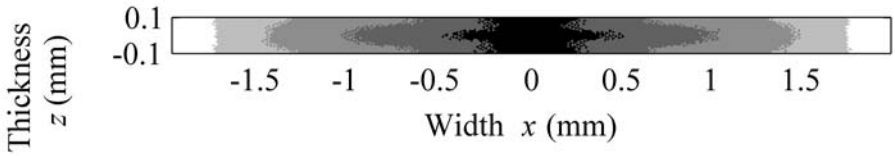

Figure 7.2: Contour map of the computed current density distribution $J_{CDD}(x, z)$ at a computed transport current I_{op} = 148 A. The colored areas from black to white represent J_{CDD} values of 236.0-217.6, 217.6-199.2, 199.2-180.8, 180.8-162.4 and 162.4-144.0 A mm^{-2}, respectively.

The current density was highest in the middle of the tape because the self-field was zero and material was assumed homogeneous. The lowest J_{CDD} occurred at the tape edges, where the z-component of $\mathbf{B}_s$ was the highest. Because $J_{CDD}(z)$ remained fairly constant, we reduced $J_{CDD}(x, z)$ into one-dimensional current per unit width, $i_{CDD}(x) = \int_{-H/2}^{H/2} J_{CDD}(x, z)\mathrm{d}z$, where H is the thickness of the tape. In the jth region, the current per unit width was defined according to LSF as $i_{LSF}(x) = N_J I_j / W$, where W is the tape width. The $i_{CDD}(x)$ and $i_{LSF}(x)$ are compared in Figure 7.3.

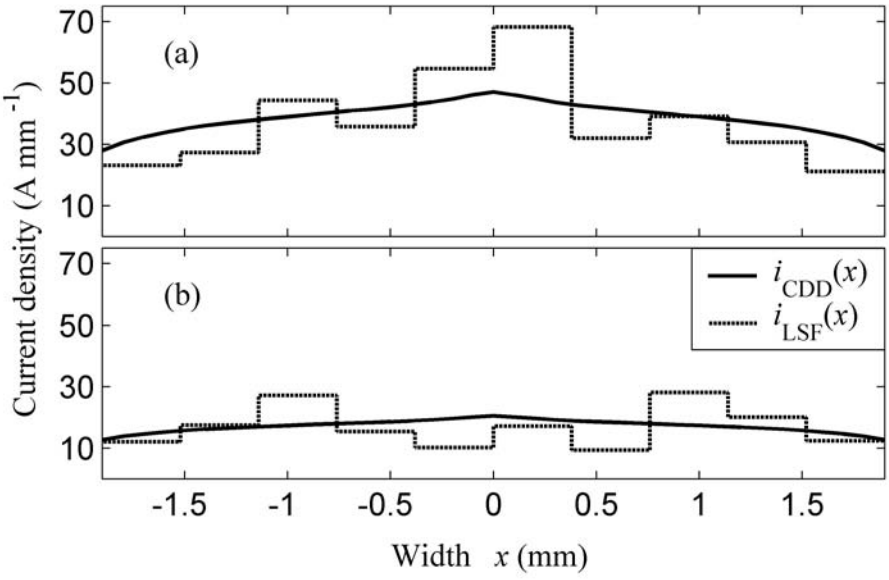

Figure 7.3: Comparison of $i_{CDD}(x)$ and $i_{LSF}(x)$; (a) corresponds to I_{op} = 148 A and (b) I_{op} = 66 A.

The shape of i_{CDD}(x) depends only slightly on the operating current. The minimum of i_{CDD} at the edges, $i_{CDD}(\pm W/2)$, was 38 % lower than the $i_{CDD}(0)$ at I_{op} = 66 A. This differerence increased to 41 % at I_{op} = 91 A, after which it decreased again, reaching 35 % at I_{op} = 148 A. Two effects create these slight variations. First, since both $J_c(\mathbf{B})$ and $n(\mathbf{B})$

are decreasing functions of **B**, the $E(J)$ characteristics at different **B** approach each other when current density increases. On the other hand, with rising current the self-field gets bigger. The interplay between these effects is shown schematically in Figure 7.4. The $E(J)$ curves at different **B** close each other asymptotically. Therefore, although the self-field at $x = \pm W/2$ rises faster with rising current than at $x = 0$, the closing of the $E(J)$ characteristics overcomes this at some point due to the nonlinear **B**-dependence of the superconductor and explains the difference variation between $i_{CDD}(0)$ and $i_{CDD}(\pm W/2)$.

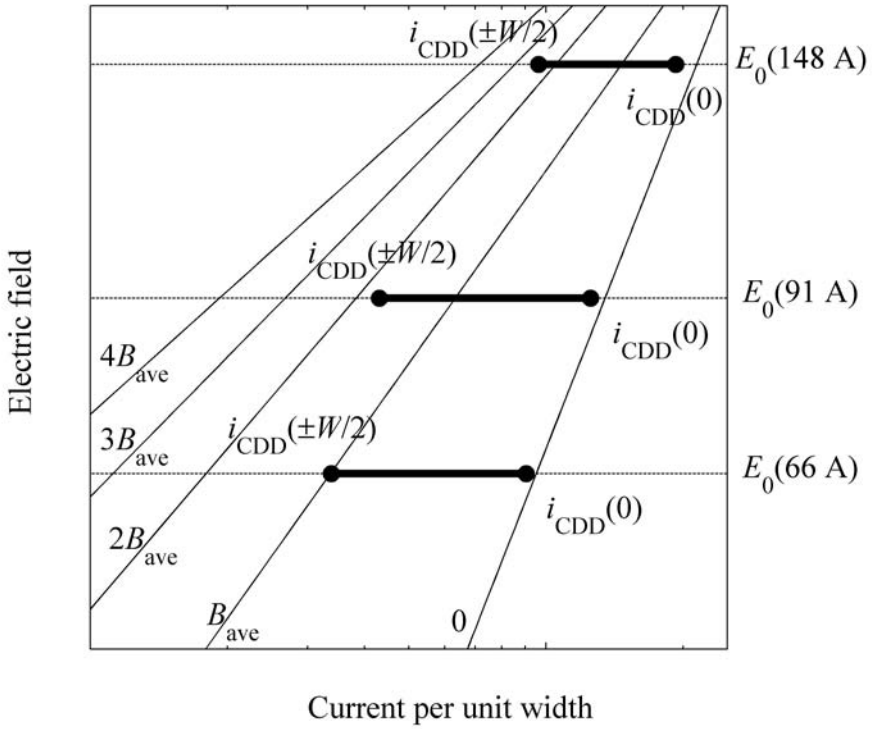

Figure 7.4: Schematic explanation for the combined effect of B-dependence of $E(J)$-curves and the increase of self-field on the difference between $i_{CDD}(0)$ and $i_{CDD}(\pm W/2)$. Thin lines represent the $E(J)$-curves at different B-values of 0, B_{ave}, $2B_{ave}$, $3B_{ave}$, and $4B_{ave}$ on a logarithmic scale. The thick horizontal lines represent the current per unit width variation range at three E_0 values corresponding to the three computed I_{op} values of 66, 91, and 148 A. The black dot at the left end of these lines corresponds to the maximum of B and is found at the tape edges, $x = \pm W/2$. The black dot at the right end corresponds to the minimum of B and is found at the tape center $x = 0$.

The $i_{LSF}(x)$ varies more with x than the $i_{CDD}(x)$ at $I_{op} = 148$ A (Figure 7.3 (a)), caused likely by the CDD model's rectangular cross-section compared to the more or less elliptical cross-section of the filamentary area in the real specimen. In contrast to the behavior of $i_{CDD}(x)$, the shape of $i_{LSF}(x)$ changes considerably between $I_{op} = 66$ A

(Figure 7.3 (b)) and I_{op} = 148 A (Figure 7.3 (a)). The $i_{LSF}(x)$ agrees well with critical state models; that is, at low currents, the innermost filaments do not carry much current [8,47]. In principle, the route through a silver matrix from current contact to filaments can affect the final current density distribution. At low amplitudes, the current should flow only in the filaments closest to the current contact, that is, closest to the tape surface. This effect should cause highest currents in the middle filaments, which is contrary to the measured behavior.

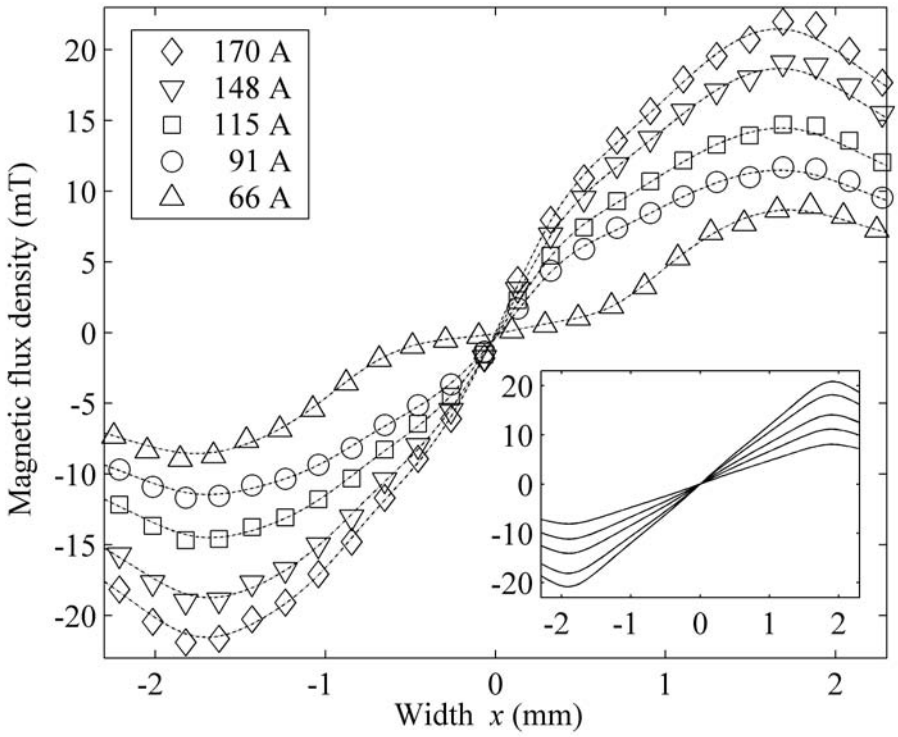

Figure 7.5: Symbols mark only some of the magnetic flux density measurement points for better visualization. Magnetic flux density profiles calculated from $i_{LSF}(x)$ are shown with dashed lines. Solid lines in the inset show corresponding magnetic flux density profiles calculated from $J_{CDD}(x, z)$.

To check whether the LSF caused numerical error in the results, we compared the B_z profiles computed from $J_{CDD}(x, z)$ and $i_{LSF}(x)$ with the measured B_z profiles in Figure 7.5. The computed profiles above the tape are practically linear and due to small changes in the J_{CDD} distribution, their shape is almost independent of the operating current. At I_{op} = 66 A, the measured profile is close to zero at -0.5 mm < x < 0.5 mm. This flat part of the profile narrows down with a rising current and at I_{op} = 74 A disappears completely. Consequently, the behavior of an Bi-2223/Ag material cannot be described solely with

non-linear $E(J)$ characteristics derived from voltage–current measurement at currents lower than ~74 A or ~0.5 I_c.

7.2 Current distribution during an AC cycle

The American Superconductor tape presented in section 5.1 was used as specimen. An alternating transport current of $i_T(\theta) = I_{op}\sin(\theta)$ was fed through the specimen in the magnetometer, and alternating current amplitudes I_{op} of 50 and 150 A were used at frequencies 20, 50, 100, and 400 Hz to demonstrate what can be seen from AC maps. To avoid disturbing the current density distributions, we measured each frequency at a separate cool-down. Measurement with $I_{op} = 50$ A was always carried out first. Later, to verify the results, we measured AC maps at frequencies of 0.1, 0.5, 1, 2, 5, and 10 Hz at $I_{op} = 25$ A. Table 7.1 gives details of each AC map.

Table 7.1: Details of AC maps. Samples per cycle, S_{PC}, and number of cycles refer to Hall and transport current signal digitization. All maps covered an area of 6 mm × 2 mm; the number of evenly distributed spatial points varies between maps according to the table data. Measurements M1-M17 are the same measurements presented previously in Table 3.1.

AC map name	M1	M3	M5	M9	M11	M13	M15	M17	M19	M20	M21	M22	M23	M24
Frequency f (Hz)	20	20	50	50	100	100	400	400	0.1	0.5	1	2	5	10
Current amplitude I_{op} (A)	50	150	50	150	50	150	50	150	25	25	25	25	25	25
Widthwise spatial points (pcs)	81	81	81	81	81	81	81	81	81	81	81	81	81	81
Lengthwise spatial points (pcs)	5	5	5	5	5	5	5	5	3	2	2	2	2	2
Parameter S_{PC} (pcs)	100	100	50	50	30	30	20	20	1000	1000	1000	500	200	100
Number of cycles C (pcs)	50	50	100	100	150	150	250	250	2	2	2	4	10	20

Computational model

In the specimen, the currents were assumed to flow lengthwise in the y-direction only. The most accurate indicator of current meandering is a magnetic flux density map created by remanence currents after the transport current has been switched off. The remanence map in Figure 7.6 shows no lengthwise variation and thereby justifies the

assumption of solely longitudinal currents. The cross-section of the specimen filament zone is divided into 400 times 50 discrete rectangles representing lengthwise current threads. The current through a thread is denoted as I_{rs}, where $1 \leq r \leq 400$ and $1 \leq s \leq 50$.

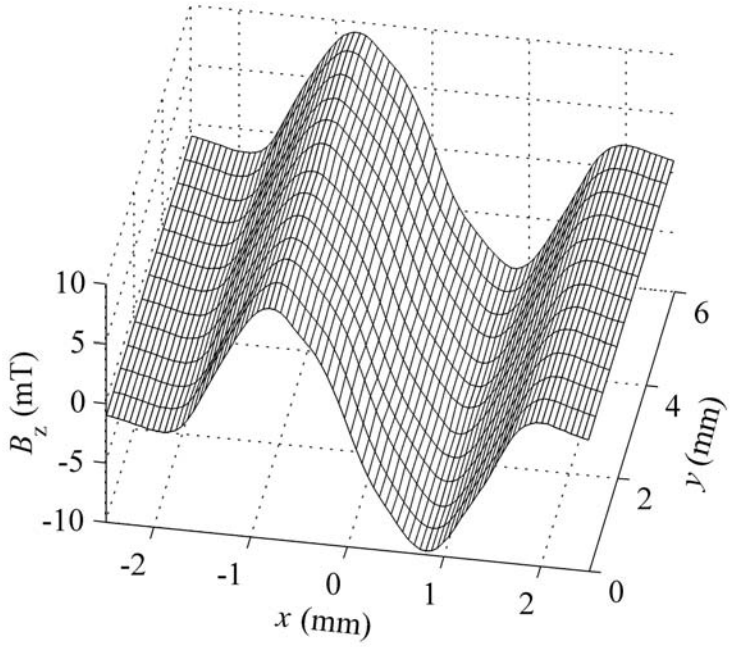

Figure 7.6: Remanence current map roughly 15 minutes after switching off a DC current of 150 A.

Penetration model

According to the Bean model [8], the transport current is assumed to penetrate the specimen's cross section as concentric ellipses from the specimen edges. Since no better estimation exists of the relative qualities of filaments or filamentary coupling, we assumed the filamentary zone to be homogeneous.

Figure 7.7 (a) presents the geometry of the penetration model. Parameters a and b are the semi-axes of the elliptical filament zone, and $a_b(\theta, G, I_N)$ and $b_b(\theta, G, I_N)$ are the semi-axes of the border ellipse between the positive and negative current regions. I_N represents the normalized transport current amplitude, I_{op} / I_c. The semi-axes $a_{min}(G, I_N)$ and $b_{min}(G, I_N)$ define the border of the current-free inner ellipse. The penetration model parameter, G, between 0 and 1 defines the elliptic penetration model that is to be used.

The $a_{min}(G, I_N)$, $b_{min}(G, I_N)$, $a_b(\theta, G, I_N)$, and $b_b(\theta, G, I_N)$ are calculated during a diminishing transport current cycle half, $\theta \in [\pi/2, 3\pi/2]$, from equations

$$\left(\frac{a_{min}}{a}\right)^G = \frac{b_{min}}{b}, \quad \left(\frac{a_b}{a}\right)^G = \frac{b_b}{b}, \tag{7.1}$$

$$\frac{A_{max} - A_{min}}{A_{max}} = \frac{\pi ab - \pi a_{min} b_{min}}{\pi ab} = \min\left(1, I_N\right), \text{ and} \tag{7.2}$$

$$\begin{aligned} \frac{A_+ - A_-}{A_{max}} &= \text{sign}\left(I_N \sin\theta\right) \cdot \min\left(1, \left|I_N \sin\theta\right|\right) \\ A_+ &= A_b - A_{min} = \pi a_b b_b - \pi a_{min} b_{min} \\ A_- &= A_{max} - A_b = \pi ab - \pi a_b b_b \end{aligned} \quad . \tag{7.3}$$

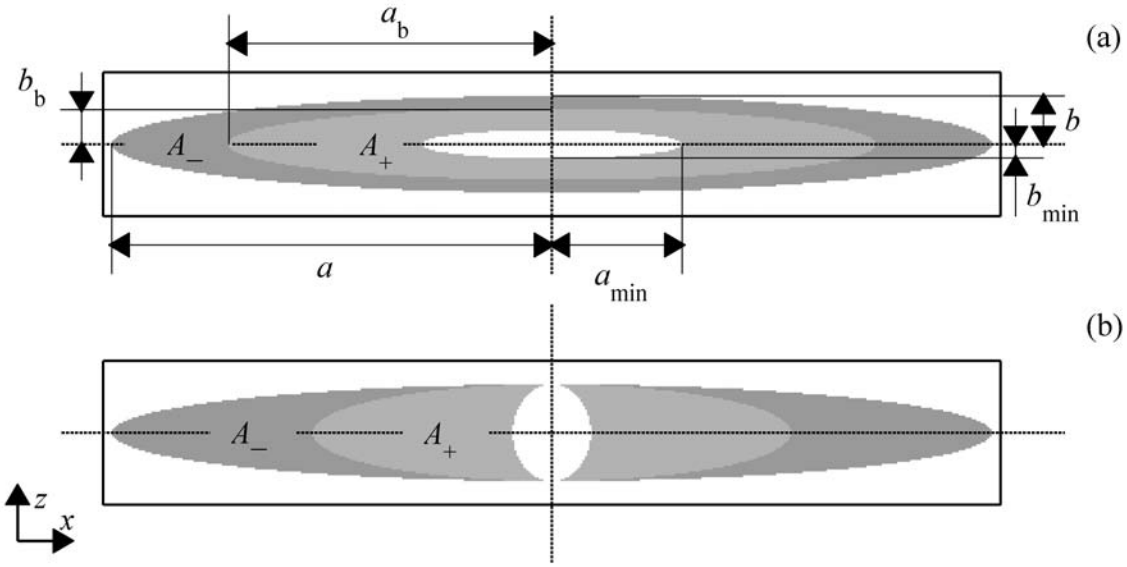

Figure 7.7: Current penetration areas when $I_N = 0.9$ and $\theta = \pi$ rad. (a) Current penetration when $G = 1$. Parameters a and b define the semi-axes of the filamentary zone ellipse; a_b and b_b are the semi-axes of the border ellipse between positive and negative current zones; a_{min} and b_{min} define the semi-axes of the current-free zone. A_+ and A_- mark the positive and negative current zones, respectively. (b) Current penetration when $G = 0$.

Equation (7.1) defines the penetration model, and (7.2-7.3) are derived from the relative areas of negative and positive currents based on the Bean model. A_{max} means the filamentary zone ellipse area, A_{min} is the current-free zone area, and A_b is the area defined by the border semi-axes. A_+ and A_- refer to the positive and negative current areas, shown

in Figures 7.7 (a) and 7.7 (b). In case of $I_N \geq 1$, no current-free inner zone exists, and during the times $|i_T(\theta)| > I_c$, the current over I_c is evenly distributed between all threads in A_+ or A_-. From (7.1-7.3), we can easily derive that

$$a_b(\theta, G, I_N) = a\left\{1 + \frac{1}{2}\left[\operatorname{sign}\left(I_N \sin(\theta)\right) \cdot \min\left(1, \left|I_N \sin(\theta)\right|\right) - \min\left(1, I_N\right)\right]\right\}^{\frac{1}{G+1}},$$

$$b_b(\theta, G, I_N) = b\left\{1 + \frac{1}{2}\left[\operatorname{sign}\left(I_N \sin(\theta)\right) \cdot \min\left(1, \left|I_N \sin(\theta)\right|\right) - \min\left(1, I_N\right)\right]\right\}^{\frac{G}{G+1}}, \quad (7.4)$$

$$a_{min}(G, I_N) = a\left[1 - \min\left(1, I_N\right)\right]^{\frac{1}{G+1}}, \quad \text{and} \quad b_{min}(G, I_N) = b\left[1 - \min\left(1, I_N\right)\right]^{\frac{G}{G+1}}.$$

Thread current determination

We now know the elliptic semi-axes (7.4) of the current areas and can calculate the discrete thread currents $I_{rs}(\theta, G, I_N)$. $P_{rs}(\theta, G, I_N)$ and $N_{rs}(\theta, G, I_N)$ are used as temporary variables to define whether each thread belongs to a positive, negative, or zero current-region. X_{rs} and Z_{rs} represent the x- and z-coordinates of the center of each current thread. The threads carrying positive and negative currents during a diminishing current cycle half are searched according to

$$P_{rs}(\theta, G, I_N) = \begin{cases} 1, \text{ if } \dfrac{X_{rs}^2}{a_b^2(\theta, G, I_N)} + \dfrac{Z_{rs}^2}{b_b^2(\theta, G, I_N)} < 1 \ \wedge \ \dfrac{X_{rs}^2}{a_{min}^2(G, I_N)} + \dfrac{Z_{rs}^2}{b_{min}^2(G, I_N)} \geq 1 \\ 0, \quad \text{otherwise} \end{cases}$$

and

$$N_{rs}(\theta, G, I_N) = \begin{cases} 1, \quad \text{if} \quad \dfrac{X_{rs}^2}{a_b^2(\theta, G, I_N)} + \dfrac{Z_{rs}^2}{b_b^2(\theta, G, I_N)} \geq 1 \\ 0, \quad \text{otherwise} \end{cases}.$$

The positive and negative currents I_{pos} and I_{neg},

$$I_{\mathrm{pos}} = \frac{I_{\mathrm{op}}\left[1+\sin(\theta)\right]}{2} \quad \text{and} \quad I_{\mathrm{neg}} = \frac{I_{\mathrm{op}}\left[1-\sin(\theta)\right]}{2},$$

are equally divided between the threads with $P_{rs} = 1$ and $N_{rs} = 1$, respectively. Then, $I_{rs}(\theta, G, I_{\mathrm{N}})$ can be defined as

$$I_{rs}(\theta, G, I_{\mathrm{N}}) = \frac{I_{\mathrm{pos}} P_{rs}(\theta, G, I_{\mathrm{N}})}{\sum_{r,s} P_{rs}(\theta, G, I_{\mathrm{N}})} - \frac{I_{\mathrm{neg}} N_{rs}(\theta, G, I_{\mathrm{N}})}{\sum_{r,s} N_{rs}(\theta, G, I_{\mathrm{N}})},$$

where the first term is zero in the negative current-zone threads, and the second term is zero in the positive current-zone threads. If a thread belongs to a zero current-zone, both terms are zero. Naturally, the current distribution in an increasing current cycle half is opposite to that given above.

Figure 7.7 shows also the current penetration in the extremes of G at $I_{\mathrm{N}} = 0.9$ and $\theta = \pi$ rad. Figure 7.7 (a) shows the current penetration when $G = 1$; closely similar models have been used to explain the current penetration at AC transport currents, for example, in [1,69]. Figure 7.7 (b) shows that when $G = 0$, the model resembles closely the current penetration often encountered in external magnetic field calculations [1,11], apart the fact that the current flows in the same direction on both sides of the specimen. Comparison of Figures 7.7 (a) and 7.7 (b) demonstrates clearly the effect of the parameter G on the definition of the penetration model.

Magnetic flux density calculation

We can calculate analytically also the magnetic flux density z-component at the measurement point (x_m, z_m), caused by the thread current I_{rs}, $B_{zrs}(x_m, z_m, \theta, G, I_{\mathrm{N}})$ [9]. By summing the contributions B_{zrs} from all current threads, we arrive at $B_{\mathrm{z}}(x_m, z_m, \theta, G, I_{\mathrm{N}})$. To be later able to optimize the penetration model parameter, we must efficiently compare measured and calculated magnetic flux densities. For such comparison and to be able to move on to the frequency plane, we must define the simulated samples of the magnetic flux density z-component, $c_{mn}(G, I_{\mathrm{N}})$. Since S_{PC} is fixed in each measurement, we can define $c_{mn}(G, I_{\mathrm{N}})$ as

$$\theta_n = n2\pi/S_{\mathrm{PC}}, \quad 0 \le n \le (N-1) \quad \Rightarrow \quad c_{mn}(G, I_{\mathrm{N}}) = B_{\mathrm{z}}(x_m, z_m, \theta_n, G, I_{\mathrm{N}}).$$

Frequency components

Here DFT analysis means finding the N frequency components, $\mathrm{V_{H}}_{mk}$ and $\mathrm{I_{T}}_{mk}$, $0 \le k \le (N-1)$, of the digitized $v_{\mathrm{H}mn}$ and i_{mn} and comparing them with the corresponding frequency components, $\mathrm{C}_{mk}(G, I_{\mathrm{N}})$, calculated from the simulated samples $c_{mn}(G, I_{\mathrm{N}})$. The defining equations can be found in publication 7.

At any measurement point m, the frequency spectrum, FS_m, of $\mathrm{V_{H}}_{mk}$, $\mathrm{I_{T}}_{mk}$, and $\mathrm{C}_{mk}(G, I_{\mathrm{N}})$ is given using only positive frequencies and scaling equal to the amplitudes of these frequencies. Definition of FS_m equations appear in publication 7. FS_m components correspond to frequencies $f_k = k f S_{\mathrm{PC}} / N$, where f is the frequency of the alternating current i_{T}. Information about DFT is widely available, for example, in [14].

In addition to comparing frequency spectra at different measurement points m, we could benefit from checking the spatial profiles SP_k of the desired FS_m component k. The defining equations for the spatial profiles spanning over $m_1 \le m \le m_2$ are given in publication 7.

Error functions

Two error-functions, $\Delta_1(G, I_{\mathrm{c}})$ and $\Delta_{13}(G, I_{\mathrm{c}})$, are defined below. We use them later to show the difference when we include the third harmonic to optimize the penetration model parameters G and I_{c}. Indexes K and L refer to the frequency components of the transport current main frequency f and its third harmonic, respectively, in equations

$$\Delta_1(G, I_{\mathrm{c}}) = \sqrt{\sum_{m=m_1}^{m_2} \left[\left| C_{mK}(G, I_{\mathrm{N}}) \right| - \left| \mathrm{V_{H}}_{mK} \right| \right]^2 \Big/ \sum_{m=m_1}^{m_2} \left| C_{mK}(G, I_{\mathrm{N}}) \right|^2},$$

$$\Delta_3(G, I_{\mathrm{c}}) = \sqrt{\sum_{m=m_1}^{m_2} \left[\left| C_{mL}(G, I_{\mathrm{N}}) \right| - \left| \mathrm{V_{H}}_{mL} \right| \right]^2 \Big/ \sum_{m=m_1}^{m_2} \left| C_{mL}(G, I_{\mathrm{N}}) \right|^2}, \quad \text{and}$$

$$\Delta_{13}(G, I_{\mathrm{c}}) = \Delta_1(G, I_{\mathrm{c}}) + \Delta_3(G, I_{\mathrm{c}}).$$

Characteristics of measured data

Previously, Hall sensor measurements at AC current have been carried out with a lock-in amplifier. In these measurements, the harmonic frequency content has been small and has therefore often been discarded [18]. Our measurements confirmed that at harmonic frequencies the signal was small yet significant enough to explain the time-evolution of the measured magnetic flux density.

In measurements at I_{op} = 150 A, harmonic frequency amplitudes were always < 4 % of the main frequency amplitude of the Hall voltage and < 1.5 % of the main frequency amplitude of the current at the spatial point, x_{max}, where the measured signal was maximal (see Figures 7.8 (c), 7.8 (e), 7.9 (c), and 7.9 (e)). However, the relative harmonic content changed as we selected a spatial point closer to the center of the specimen. Figures 7.8 (d), 7.8 (f), 7.9 (d), and 7.9 (f) illustrate the frequency content at the spatial point, x_{mid}, between the maximum measured signal and the center. The current harmonic amplitudes were still < 1.5 % of the main frequency component, but the harmonic frequency amplitudes of the Hall voltage, compared to the main frequency amplitudes, were typically ~15 % at 20 Hz, ~12 % at 50 Hz, ~11 % at 100 Hz, and ~8 % at 400 Hz. An increasing harmonic content transforms the sine to a "shark's fin," as seen in Figures 7.8 (a) and 7.8 (b). Two distinctive parts can be seen in the "shark's fin." First, the signal diminishes slowly from its maximum, and then at some point it begins to plunge. The harmonic content's spatial dependence existed also in the measurements at I_{op} = 25 A and I_{op} = 50 A though its effect was hardly visible.

In these measurements, noise components were generally small and concentrated on the main frequency harmonics, as seen in Figures 7.8 (c)-(f), 7.9 (e), and 7.9 (f). Only in measurements M15 and M17 was significant noise discovered in the Hall voltages, concentrating on the 384 Hz harmonics, as shown in Figures 7.9 (c) and 7.9 (d). These noise components can be seen as variation in the signal amplitude in Figure 7.9 (a) and as variation in both signal amplitude and form in Figure 7.9 (b). Clearly, the noise components make measurements M15 and M17 seem like failures or devoid of information.

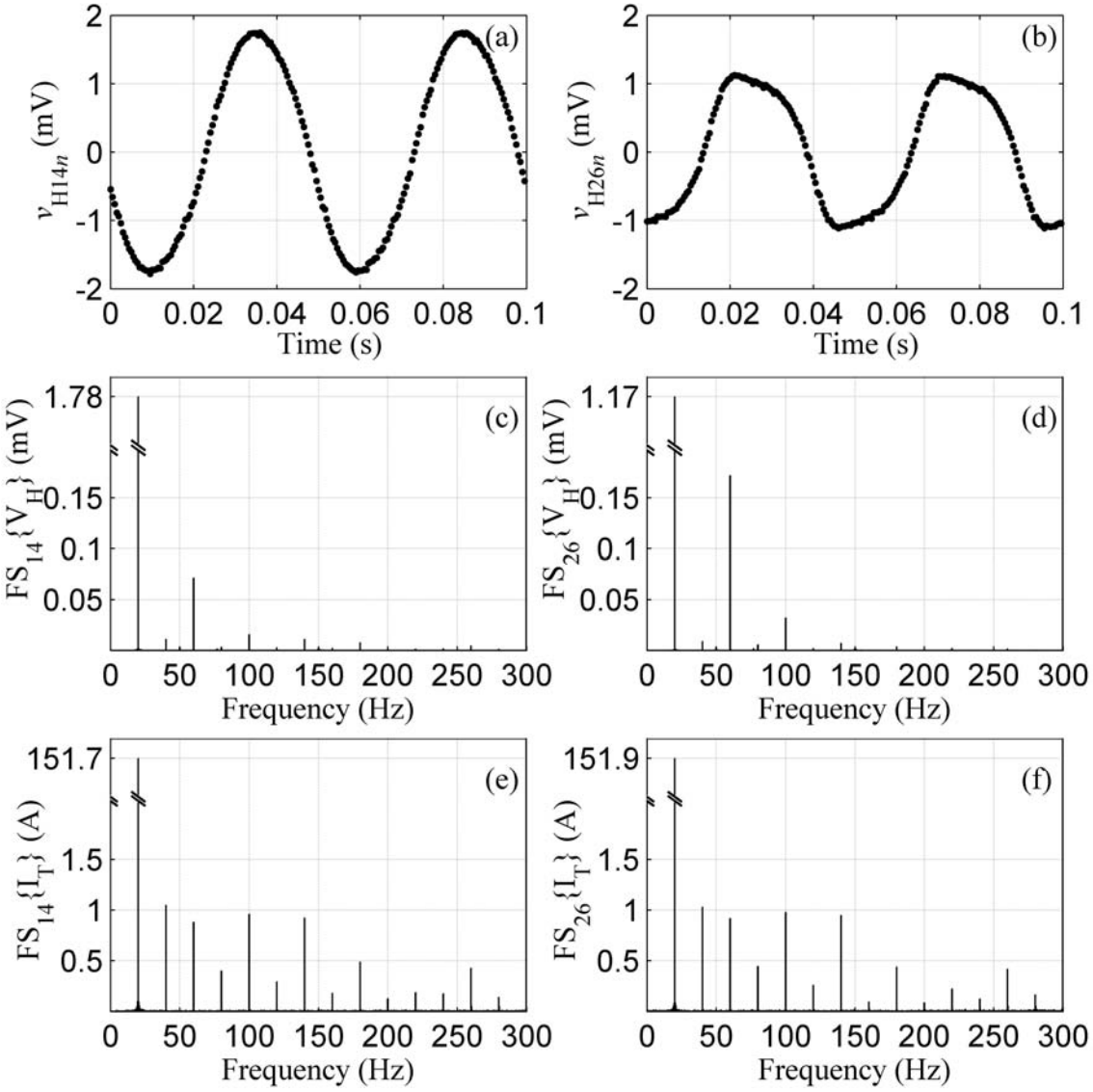

Figure 7.8: Frequency spectra of M3 at spatial points m = 14 and m = 26. The first point corresponds to x_{max} and the second to x_{mid}. (a) The first two cycles of v_{H14n} digitizations and (b) v_{H26n} digitizations. (c) Part of the $FS_{14}\{V_H\}$, (d) $FS_{26}\{V_H\}$, (e) $FS_{14}\{I_T\}$, and (f) $FS_{26}\{I_T\}$.

After the M17 measurement, the Hall current was switched off, and the measurement was rerun during the same cool-down. The induced voltage waveform resembled a sine, except for the relatively flat area between each sine cycle. The signal's frequency components, their relative strengths, and even the signal levels corresponded closely to the noise in Figures 7.9 (c) and 7.9 (d). Because the signal's frequency components did not comprise the harmonics of the current's main frequency, they were probably caused by some structural limits of the Hall-sensor.

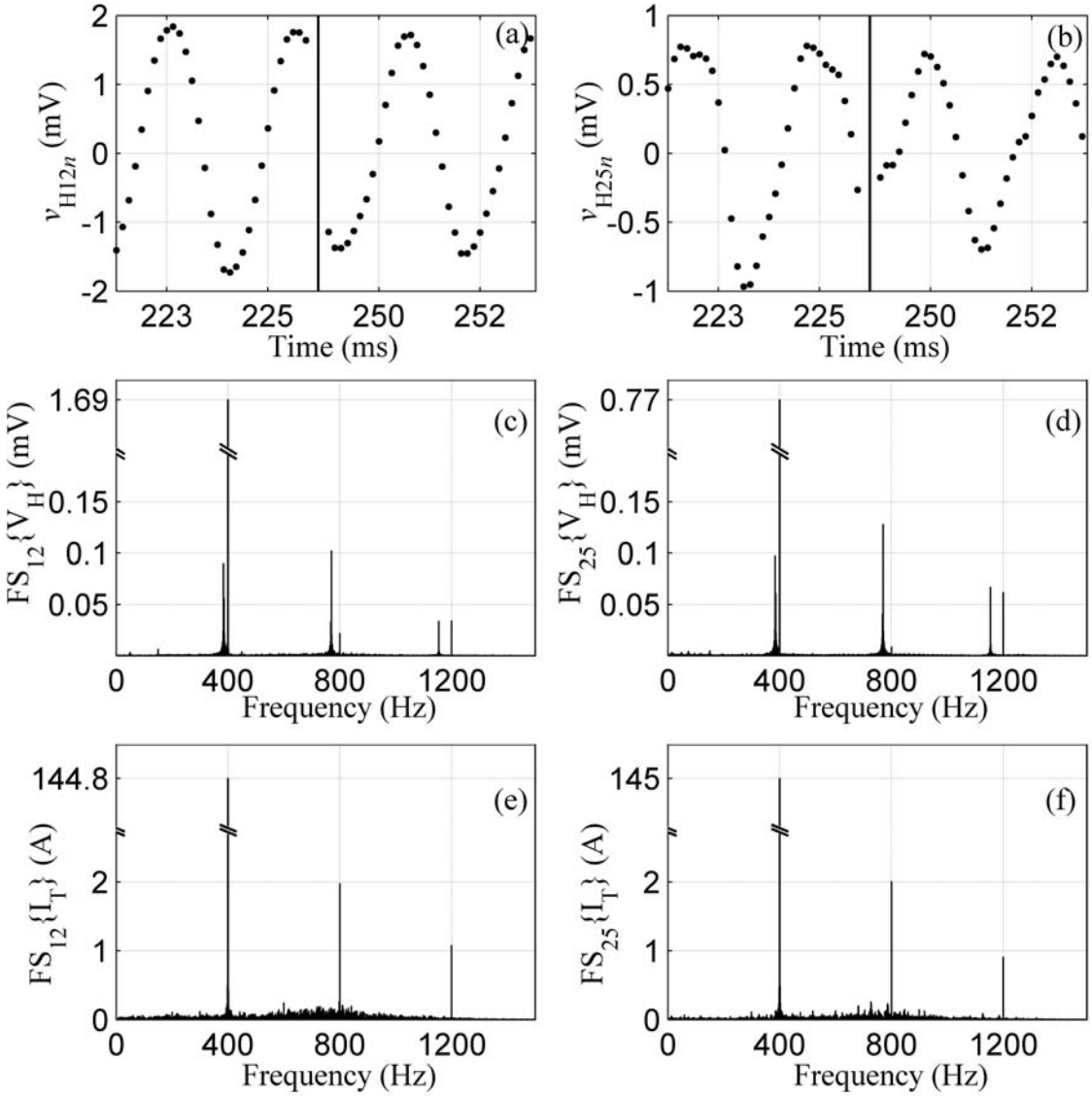

Figure 7.9: Frequency spectra of M17 at spatial points $m = 12$ and $m = 25$. The first point corresponds to x_{max} and the second to x_{mid}. (a) Two short sections of v_{H12n} digitizations. The signal form is seen as practically sine, but amplitude is fluctuating. (b) Two short sections of v_{H25n} digitizations. Both signal form and amplitude fluctuate rapidly. (c) Part of the $FS_{12}\{V_H\}$, (d) $FS_{25}\{V_H\}$, (e) $FS_{12}\{I_T\}$, and (f) $FS_{25}\{I_T\}$.

Though the noise components in M15 and M17 appeared to compromise the usefulness of the AC Hall system, they, in fact, demonstrate the system's versatility. Measurements made with the AC Hall magnetometer allow full exploitation of digitized signal processing tools, expanding thus the usefulness of the results. For example, identifiable noise components can be filtered away for easily interpretable results, as shown in Figure 7.10. Effective filtering can be done in the time domain as well, where the average current and Hall-voltage cycles can be determined as discussed in section 3.4.

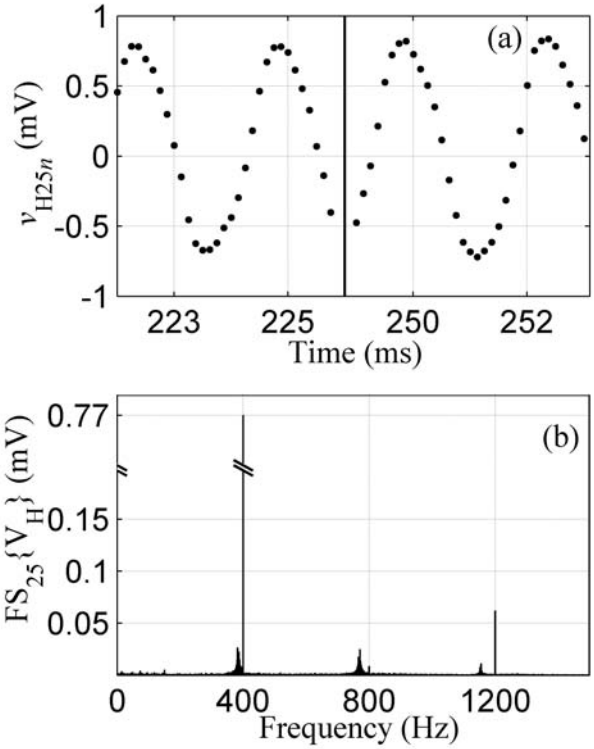

Figure 7.10: (a) Two short sections seen in Figure 7.9 (b) after crude filtering of noise frequencies. Signal form and amplitude fluctuate minimally; the "shark's fin" is clearly visible. (b) Figure 7.9 (d) after the crude filtering.

Main frequency and third harmonic optimization

Table 7.2 shows the values of G_1, I_{c1}, G_{13}, and I_{c13}, which correspond to the minimum error values of $\Delta_1(G, I_c)$ and $\Delta_{13}(G, I_c)$ in each measurement. Error minimization using $\Delta_1(G, I_c)$ is referred to as main frequency optimization and that using $\Delta_{13}(G, I_c)$ as third harmonic optimization.

Table 7.2: Results of main frequency and third harmonic optimization. G_1 shows minimum error Δ_1 G-values and I_{c1} the corresponding minimum I_c-values. G_{13} and I_{c13} show the same values for the minimum error Δ_{13}.

AC map name	M1	M3	M5	M9	M11	M13	M15	M17	M19	M20	M21	M22	M23	M24
G_1	1.00	0.00	1.00	0.05	1.00	0.59	1.00	0.85	1.00	1.00	1.00	1.00	1.00	1.00
I_{c1} (A)	126	163	128	170	134	159	148	170	101	110	110	97	108	105
G_{13}	1.00	0.80	0.99	1.00	1.00	1.00	0.97	1.00	1.00	1.00	1.00	1.00	1.00	1.00
I_{c13} (A)	164	151	178	158	171	167	175	189	159	163	163	163	163	162

Optimization can give I_c values roughly with an uncertainty of 5 A and G values with an uncertainty of 0.1. Nevertheless, both optimization results showed that the I_c values were frequency independent at 0.1-10 Hz (M19-M24). In other words, current distribution does not markedly change within this frequency range. In all measurements, optimization gave satisfactory spatial profiles of the main frequency (for example, Figure 7.11 (a)), but the poor fitting of the third harmonic spatial profiles in measurements M19-M24 suggests that the penetration model needs further refining (see Figure 7.11 (b)).

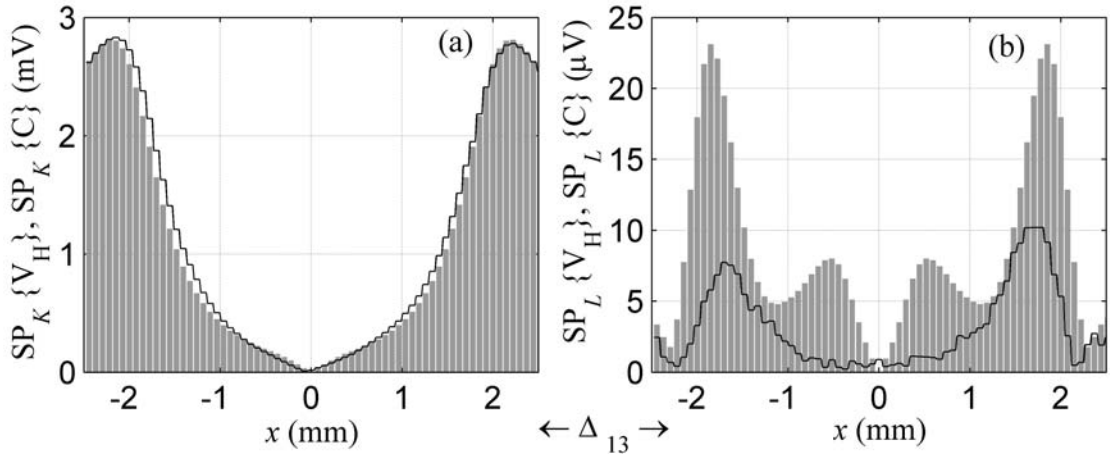

Figure 7.11: Comparison between spatial profiles of M20 (dark lines) and third harmonic optimization results (light bars): (a) main frequency and (b) third harmonic frequency.

The greatest difference between the main frequency and third harmonic optimization occurred in measurements M3, M9, M13, and M17. While main frequency optimization gave G-values of 0.00, 0.05, 0.59, and 0.85 for these measurements, third harmonic optimization yielded more credible results of 0.80, 1.00, 1.00, and 1.00, respectively. Also the optimal I_c-values differed considerably.

Figure 7.12 (a) and (c) shows computed main frequency and third harmonic spatial profiles calculated using G_1 and I_{c1} compared to measured spatial profiles. The calculated third harmonic profiles were far too big, but the main frequency profiles were a close match. The result was to be expected because the main frequency optimization sought to minimize only the difference between measured and calculated main frequencies. Figure 7.12 (b) and (d) shows computed main frequency and third harmonic spatial profiles calculated using G_{13} and I_{c13} compared to measured spatial profiles. Comparison

of Figure 7.12 (a)-(b) and 7.12 (c)-(d) shows that though the main frequency match is worse in the third harmonic optimization, the latter results are yet much better.

The difference between calculation and measurement in Figure 7.12 (b) further underlines the need to refine the penetration model. Because the difference between the third harmonic optimization results and measured spatial profiles is much better in Figure 7.12 (b) and (d) than in Figure 7.11, the penetration model should be refined in terms of its frequency dependence. The detail suggests that refinement should be based on either flux creep or some filament coupling.

Figure 7.12 (e)-(f) shows a few cycles of calculated Hall signals using the main frequency and the third harmonic optimization results at spatial points corresponding to x_{max} and x_{mid}. The signal form of the third harmonic optimization resembled here much more closely the measured "shark's fin" (see Figures 7.8 (b) and 7.12 (f)). In addition, the resemblance of the calculated "shark's fin" to the measured signal proves that the main reason behind this shape is not related to flux creep but can be accurately produced by the critical state-based model used in this thesis.

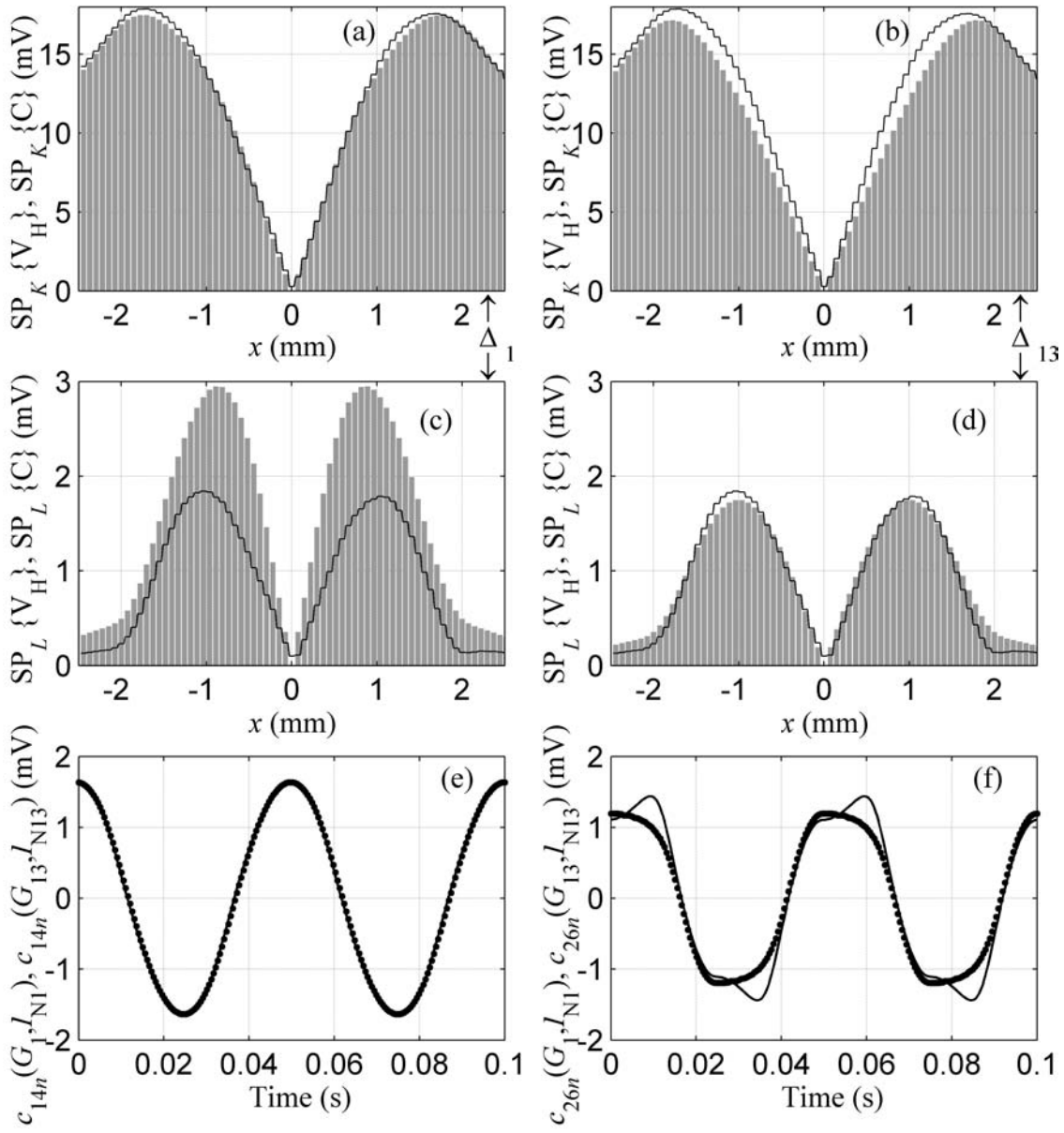

Figure 7.12: Comparison of main frequency optimization and third harmonic optimization results of measurement M3. Spatial profiles from measurement M3 (dark lines) and optimization (light bars): (a) main frequency f, optimization with Δ_1; (b) main frequency f, optimization with Δ_{13}; (c) third harmonic frequency, optimization with Δ_1; and (d) third harmonic frequency, optimization with Δ_{13}. Hall voltage as a function of time, calculated from the main frequency (solid line), and third harmonic optimization (dotted line) results at (e) spatial point $m = 14$ that corresponds to x_{max} and (f) spatial point $m = 26$ that corresponds to x_{mid}. Symbols I_{N1} and I_{N13} refer to I_{op} / I_{c1} and I_{op} / I_{c13}, respectively.

7.3 Chapter summary

In this chapter, the effect of self-field in the evolution of current density inside the Bi-2223/Ag tape during a $V(I)$ measurement was checked. Hall measurements and a simple inversion method were used to compare calculation results with measurements. The measurements and calculations correlated well, but only for currents of $I_{op} > 0.5\ I_c$. In addition, DFT analysis was used to compare measured magnetic flux densities with different alternating transport current penetration models. Optimization yielded only moderate resolution, but the calculations proved numerically stable. The results improved considerably when the third harmonic was included in the optimization. The optimal I_c used in the calculations was much higher than DC I_c.

8 Conclusions

This thesis evaluated the usefulness of magnetic flux density maps measured with a Hall sensor magnetometer. Chapter 2 introduced first the necessary basic concepts needed to understand the rest of this thesis. Then chapter 3 presented the Hall magnetometer and expanded on its capabilities. Chapter 4 discussed the various ways of calculating the currents causing the measured maps, and chapter 5 demonstrated and explained the differences directly visible in the DC and AC maps. Chapter 6 showed the advantages of combining Hall magnetometer measurements with those by magnetic knife. Finally, chapter 7 focused on calculation of the current densities causing current voltage dependence in $V(I)$ measurements and introduced and made use of an optimization method to test an AC cycle penetration model for current density.

The magnetometer presented in chapter 3 is capable of measuring the **B** distribution on top of an HTS specimen at 77 K caused by any cyclic current form in the frequency range of 0-400 Hz. The system differs from previous AC Hall magnetometers in that it does not use phase-lock amplifiers but offers a full spectrum of digitization data for a vast array of digital post-processing tools. In this study, several measurements showed that the results were reproducible and informative. The system is inexpensive, robust, simple to use, and, with fully computerized measurements and post-processing, well suited for tape manufacturers to test systematically, for example, the flux creep time dependence and AC current density evolution of their specimens.

In chapter 4, the inversion method that is used to calculate the current densities causing the measured maps was shown to be numerically unstable. The statistical tools introduced give more realistic error limits for any inversion method than the mathematical tools based on the condition number of the model matrix. Therefore, the former are useful

for comparing different inversion methods and for assessing their numerical stability. In addition, they are important test tools for all those who calculate current density distributions from magnetic flux density maps measured on top of HTS specimens and for others who may use them for calculations involving inversion methods. A numerically stable direct method for determining current densities proved also a simple alternative tool for inversion.

Chapter 5 examined the visible differences in the measured magnetic flux density maps and linked them with those in current densities inside the specimens. Differences did exist between DC and AC maps as well as between Bi-2223/Ag and copper maps. At low I_{op} values, defects in the specimen center were barely visible while those at the edge were barely visible at high I_{op} values. Therefore, the remanent map remains the best tool for checking tape homogeneity. An extensive set of different specimens was tested, and the results showed that several types of defects and structures could be identified by comparing the measured magnetic flux density maps. Generally, thin specimens had more defects at the edges and some problems were identified as being caused by heat treatment rather than mechanical processing. Such knowledge about visible differences in measured maps and an ability to distinguish their probable causes is essential for anyone, primarily tape manufacturers and physicists, who makes Hall measurements or estimates tape homogeneity and performance under AC currents. Association of a certain shape with a probable cause can be turned into an automated measurement and analysis tool for tape homogeneity without recourse to slow or numerically unstable calculations.

In chapter 6, a comparison was made between Hall sensor and magnetic knife measurements. These methods should not be seen as competitive techniques, but rather as complementary measurements that can be combined to examine possible current variations in the x and y-directions. The magnetic knife suppresses possible lateral current meandering and changes thus the current distribution in certain specimens, as seen in Hall sensor measurements. The magnetic knife also removes the self-field effect. The $J_y(x)$ variations were modeled with 2D calculations and current variations in the tape xy-plane by 3D models. No one model alone could produce a map like the measured one, which most likely resulted from a combined effect of various defects. Each measurement system has its limitations, and only by combining measurements from several systems can we

arrive at relatively reliable analysis of the causes behind the measured effects. Consequently, understanding the effects discussed above will help focus analysis of any Hall sensor or magnetic knife measurements.

In chapter 7, calculations were made of how current distribution evolved during a $V(I)$ measurement and an AC cycle. In the $V(I)$ calculation, the measured magnetic flux density dependence of I_c and the n values of the specimen were used in FEM calculations. Comparison of the Hall profiles to the FEM calculations revealed that the self-field effect correlated well with the measurements, but only at I_{op} values of $> 0.5\, I_c$. The n-value calculated from the $V(I)$ curve can be higher than the n of the material at zero field because an increasing self-field during the measurement steepens the $V(I)$ curve. The $V(I)$ calculation result that the power law should be applied only in cases of $I_{op} > 0.5\, I_c$ is important for scientists who calculate losses in HTS tapes.

DFT analysis was used to compare measured magnetic flux densities with different alternating transport current penetration models. The best model was selected based on an optimization process. The process gave only a moderately accurate I_c and penetration parameter G, but it could reliably distinguish differences even in thicknesswise evolution of current density. The results show that the third harmonic content is crucial in optimization and must be taken into account for consistent results. The I_c values given by optimization were systematically greater than the DC I_c values. For anyone interested in examining current density distributions inside a specific specimen, DFT analysis and optimization based on it can prove highly useful for testing different penetration models.

In future, the above system can be modified for YBCO coated conductor tapes. In this case, the Hall sensor's distance from the tape surface must be lowered to a few micrometers, which as such is no serious problem though it calls for active distance measurement and a Hall sensor without a varnish layer. External DC and AC magnetic flux densities can also be added. For large **B** amplitudes, a compensation method must be used though in the range of 0-100 mT no compensation is necessary. Furthermore, covering the measurement system and varying its pressure extends the systems's temperature range.

References

[1] Amemiya N and Ohta Y 2001 Mode of magnetic flux penetration into high T_c superconductors with various cross-sectional shape and their AC loss characteristics *Physica C* **357-360** 1134-43

[2] Anderson P 1962 Theory of flux creep in hard superconductors *Phys. Rev. Lett.* **9** 309-11

[3] Arndt T, Aubele A, Krauth H, Munz M, and Sailer B 2005 Progress in the preparation of technical HTS-tapes of type Bi2223/Ag-alloy of industrial lengths *IEEE Trans. Appl. Supercond.* **15** 2503-6

[4] Arndt T, Aubele A, Krauth H, Munz M, Sailer B, and Szulczyk A 2003 Bi-2223 tapes - specific performance for different applications *IEEE Trans. Appl. Supercond.* **13** 3030–3

[5] Ashworth S and Suenaga M 1999 Measurements of ac losses in superconductors due to ac transport currents in applied ac magnetic fields *Physica C* **313** 175-87

[6] Ashworth S and Suenaga M 1999 The calorimetric measurement of losses in HTS tapes due to ac magnetic fields and transport currents *Physica C* **315** 79-84

[7] Ashworth S and Suenaga M 2001 Local calorimetry to measure ac losses in HTS conductors *Cryogenics* **41** 77-89

[8] Bean C 1964 Magnetization of high-field superconductors *Rev. Mod. Phys.* **36** 31-9

[9] Binns K, Lawrenson P, and Trowbridge C 1992 *The Analytical and Numerical Solution of Electric and Magnetic Fields* (Chichester: Wiley)

[10] Brandt E 1992 Determination of currents in flat superconductors *Phys. Rev. B* **46** 8628–31

[11] Brandt E 1996 Superconductors of finite thickness in a perpendicular magnetic field: strips and slabs *Phys. Rew. B* **54** 4246-64

[12] Brandt E 1996 Universality of flux creep in superconductors with arbitrary shape and current-voltage law *Phys. Rev. Lett.* **76** 4030–3

[13] Bray S, Ekin J, Clickner C, and Masur L 2000 Transverse compressive stress effects on the critical current of Bi-2223/Ag tapes reinforced with pure Ag and oxide-dispersion-strengthened Ag *J. Appl. Phys.* **88** 1178–80

[14] Burrus C and Parks T 1991 *DFT/FFT and Convolution Algorithms: Theory and Implementation, 1st Edition* (New York: John Wiley & Sons)

[15] Campbell A 1995 AC losses in high T_c superconductors *IEEE Trans. Appl. Supercond.* **5** 682-7

[16] Carr W 1979 AC loss from the combined action of transport current and applied field *IEEE Trans. Magn.* **15** 240-3

[17] Chadan K 1989 *Inverse Problems in Quantum Scattering Theory, 2nd Edition* (New York: Springer)

[18] Chesneau E, Glowacki B, Kvitkovic J, Majoros M, van Beek K and Konczykowski M 1999 Comparison of magnetic field profiles of Ag/BSCCO-2223 tapes carrying AC and DC currents *IEEE Trans. Appl. Supercond.* **9** 2557-60

[19] Ciszek M, Ashworth S, James M, Glowacki B, Campbell A, Garré R, and Conti S 1996 Self-field AC losses and critical currents in multi-tube Ag-Bi-2223 conductors *Supercond. Sci. Technol.* **9** 379-84

[20] de Gennes P 1989 *Superconductivity of Metals and Alloys* (Addison Wesley)

[21] Demmel J 1997 *Applied Numerical Linear Algebra* (Philadelphia: SIAM)

[22] Dolez P, Aubin M, Willén D, Nadi R, and Cave J 1996 Calorimetric ac loss measurements of silver sheathed Bi-2223 superconducting tapes *Supercond. Sci. Technol.* **9** 374-8

[23] Dolez P, Aubin M, Zhu W, and Cave J 1998 A comparison between ac losses obtained by the null calorimetric and a standard electrical method *Supercond. Sci. Technol.* **11** 1386-90

[24] Evetts J and Glowacki B 2000 Superconducting materials - the path to applications *Supercond. Sci. Technol.* **13** 443-7

[25] Fleshler S, Cronis L, Conway G, Malozemoff A, Pe T, McDonald J, Clem J, Vellego G, and Metra P 1995 Measurement of the ac power loss of $(Bi,Pb)_2Sr_2Ca_2Cu_3O_x$ composite tapes using the transport technique *Appl. Phys. Lett.* **67** 3189-91

[26] Fukunaga T, Abe T, Oota A, Yuhya S, and Hiraoka M 1995 Alternating current transport and magnetic losses in Ag-sheathed $(Bi,Pb)_2Sr_2Ca_2Cu_3O_x$ wires *Appl. Phys. Lett.* **66** 2128-30

[27] Funaki K, Kajikawa K, Shiraishi H, Iwakuma M, Miyake S, Kumano T, and Hasegawa T 1998 A simple electromagnetic method of cyclic loss measurement for superconducting wires in a combined alternating transverse magnetic field and transport current *Physica C* **310** 132-6

[28] Glowacki B and Majoros M 2000 Transport ac losses in Bi-2223 multifilamentary tapes - conductor materials aspect *Supercond. Sci. Technol.* **13** 483-7

[29] Glowacki B, van der Beek C, and Konczykowski M 2000 Dynamic flux patterns of multifilamentary Ag/$Bi_2Sr_2Ca_2Cu_3O_{10-\delta}$ tapes at 8 K–77 K temperatures *Inst. Phys. Conf. Ser. No* **167** 779–82

[30] Goldacker W, Keßler J, Ullmann B, Mossang E, and Rikel M 1995 Axial tensile, transverse compressive and bending strain experiments on Bi(2223)/AgMg single core tapes *IEEE Trans. Appl. Supercond.* **5** 1834–7

[31] Golub G and van Loan C 1996 *Matrix Computations* (London: The Johns Hopkins Univ. press)

[32] Gourlay S, Sabbi G, Kircher F, Martovetsky N, and Ketchen D 2004 Superconducting magnets and their applications *Proc. IEEE* **92** 1675-87

[33] Hardono T, Cook C, and Jin J 1998 Calorimetric methods for measuring AC losses in HTSC tapes carrying currents *Supercond. Sci. Technol.* **11** 1087-90

[34] Hassenzahl W, Hazelton D, Johnson B, Komarek P, Noe M, and Reis C 2004 Electric power applications of superconductivity *Proc. IEEE* **92** 1655-74

[35] Heine K, Tenbrink J, and Thöner M 1989 High-field critical current densities in $Bi_2Sr_2Ca_1Cu_2O_{8+x}$ / Ag wires *Appl. Phys. Lett.* **55** 2441–3

[36] Herrmann P, Bock J, Bruzek C-E, Cottevieille C, Duperray G, Hascicek J, Legat D, Leriche A, Verhaege T, and Parasie Y. 2000 Long length PIT conductors realized by rectangular deformation route *Supercond. Sci. Technol.* **13** 477–82

[37] Hull J and Murakami M 2004 Applications of bulk high-temperature superconductors *Proc. IEEE* **92** 1705-18

[38] Indenbom M, Nikitenko V, Polyanskii A, and Vlasko-Vlasov V 1990 New method for direct study of magnetic flux distribution in superconductors *Cryogenics* **30** 747–9

[39] Jiang Z and Amemiya N 2004 An experimental method for total AC loss measurement of high T_c superconductors *Supercond. Sci. Technol.* **17** 371-9

[40] Johansen T, Baziljevich M, Bratsberg H, Galperin Y, Lindelof P, Shen Y, and Vase P 1996 Direct observation of the current distribution in thin superconducting strips using magneto-optic imaging *Phys. Rev. B* **54** 16264–9

[41] Johnston P 2001 *Computational Inverse Problems in Electrocardiography* (*Advances in Computational Bioengineering* vol 5) (Southampton: WIT Press)

[42] Kalsi S, Weeber K, Takesue H, Lewis C, Neumueller H-W, and Blaugher R 2004 Development status of rotating machines employing superconducting field windings *Proc. IEEE* **92** 1688-1704

[43] Kasztler A, Foitl M, Kirchmayr H, Polák M, and Majoros M 1999 Critical current variation and current transfer length in multifilamentary Bi-2223/Ag tapes *IEEE Trans. Appl. Supercond.* **9** 2340–2

[44] Kawano K and Oota A 1997 A study on self-field distribution in Ag-sheathed $(Bi,Pb)_2Sr_2Ca_2Cu_3O_x$ monofilamentary tape using a scanning Hall sensor magnetometry *Physica C* **275** 1–11

[45] Kawano K, Abell J, Bradley A, Lo W, and Campbell A 2000 Magnetic field and current distributions at an artificial grain boundary in $YBa_2Cu_3O_{7-x}$ *Supercond. Sci. Technol.* **13** 999-1004

[46] Kawano K, Abell J, Ohtake A, Oota A 2000 A study of the magnetic field distribution in an Ag-sheathed Bi2223 tape using scanning Hall sensor and magneto-optical techniques *Supercond. Sci. Technol.* **13** 1373-7

[47] Kim Y, Hempstead C, and Strnad A 1963 Magnetization and critical supercurrents *Phys. Rev.* **129** 528-36

[48] Kopera L, Kovác P, and Husek I 1998 New rolling technique for texturing of Bi(2223)/Ag tapes *Supercond. Sci. Technol.* **11** 433-6

[49] Kovác P, Husek I, and Kopera L 1997 Application of two-axial rolling for multicore Bi(2223)/Ag tape *Supercond. Sci. Technol.* **10** 982-986

[50] Kovác P, Husek I, Melisek T, Kawano K, and Abell J 2001 BSCCO/Ag tapes made by a tape-in-rectangular tube process *Supercond. Sci. Technol.* **14** 139-44

[51] Kovác P, Husek I, Melisek T, Metz A, van Eck H, and ten Haken B 2002 Transport currents in Bi-2223/Ag tapes made using the tape-in-rectangular tube process, current distribution and I_c-stress degradation *Supercond. Sci. Technol.* **15** 624-9

[52] Kovachev V 1991 *Energy Dissipation in Superconducting Materials* (Oxford: Clarendon Press)

[53] Krelaus J, Nast R, Eckelmann H, and Goldacker W 2000 Novel, internally stranded Bi cuprate conductor concept for ac applications: ring-bundled barrier (RBB) tapes produced by the powder-in-tube assemble and react (PITAR) method *Supercond. Sci. Technol.* **13** 567–75

[54] Kvitkovic J, Majoros M, Glowacki B A , and Apperley M 2002 DC and AC self-magnetic field profiles of (6+1) filamentary BSCCO tapes with different filament arrangements measured by Hall probe magnetometry *Physica C* **370** 187-96

[55] Lahtinen M, Paasi J, Sarkaniemi J, Han Z, and Freltoft T 1995 Homogeneity study of Bi-2223/Ag monofilamentary tapes using Hall sensor magnetometry *Physica C* **244** 115–22

[56] Lehtonen J, Ahoranta M, and Mikkonen R 2002 AC losses in non-homogeneous HTS conductors *Physica C* **372–376** 1743-5

[57] Lehtonen J, Korpela A, Nah W, Kang J, Kováč P, and Mošek T 2004 Influence of self-field on the critical current of Bi-2223/Ag tapes *Physica C* **403** 257-62

[58] Lehtonen J, Paasi J, and Mikkonen R 2000 Computation of losses in a HTS tape carrying AC transport current in external AC magnetic field at temperatures of 20–40 K *IEEE Trans. Appl. Supercond.* **10** 1200–3

[59] Magnusson N, Hörnfeldt S, Rabbers J, ten Haken B, and ten Kate H 2000 Comparison between calorimetric and electromagnetic total ac loss measurement results on a BSCCO/Ag tape *Supercond. Sci. Technol.* **13** 291-4

[60] Magnusson N, Schönborg N, Wolfbrandt A, and Hörnfeldt S 2001 Improved experimental set-up for calorimetric AC loss measurements on HTSs carrying transport currents in applied magnetic fields at variable temperatures *Physica C* **354** 197–201

[61] Mahdi A, Hughes T, Beduz C, Yang Y, Stoll R, Sykulski J, Haldar P, Sokolowski R, and Power A 1997 Thermometric measurements of the self-field losses in silver sheathed PbBi2223 multifilamentary tapes *IEEE Trans. Appl. Supercond.* **7** 1658-61

[62] Majoros M, Glowacki B, and Campbell A 2000 Transport ac losses and screening properties of Bi-2223 multifilamentary tapes covered with magnetic materials *Physica C* **338** 251-62

[63] Majoros M, Glowacki B, Campbell A, Apperley M, and Darmann F 1999 Transport ac losses in (Bi,Pb)SrCaCuO-2223/Ag multifilamentary tapes with different filament arrangements *Physica C* **323** 125-36

[64] Majoros M, Glowacki B, V`Campbell A, Han Z, and Vase P 2000 Influence of defects on transport ac losses and current-voltage characteristics of BiPbSrCaCuO-2223/Ag multifilamentary tapes *Inst. Phys. Conf. Ser. No* **167** 847-50

[65] Malozemoff A, Maguire J, Gamble B, and Kalsi S 2002 Power applications of high-temperature superconductors: status and perspectives *IEEE Trans. Appl. Supercond.* **12** 778–81

[66] Masur L, Kellers J, Li F, Fleshler S, and Podtburg E 2002 Industrial high temperature superconductors: perspectives and milestones *IEEE Trans. Appl. Supercond.* **12** 1145–50

[67] Mikkonen R 2002 Highlights of SC power applications in Europe *IEEE Trans. Appl. Supercond.* **12** 782–7

[68] Nah W, Kang J, Choi S, Park I-H, Joo J, Kwon Y-K, Oh S-S, Ryu K-S, Paasi J, and Lehtonen J 2001 Numerical calculation of critical current in Bi-2223 stacked tapes *IEEE Trans. Appl. Supercond.* **11** 3908-11

[69] Norris W 1970 Calculation of hysteresis losses in hard superconductors carrying ac: isolated conductors and edges of thin sheets *J. Phys. D* **3** 489-507

[70] Ono M, Koga S, and Ohtsuki H 2002 Japan's superconducting Maglev train *IEEE Instru. Meas. Mag.* **5** 9-15

[71] Oomen M, Rieger J, and Leghissa M 1997 Magnetic AC loss in multi-filamentary Bi-2223/Ag tapes *Inst. Phys. Conf. Ser.* **158** 1449-52

[72] Oota A,Inada R, Inagaki N, Ogawa Y, Nakamura Y, Fukunaga T, and Zhang P 2004 Significant reduction in AC transport self-field losses of Ag-sheathed Bi2223 tapes achieved by changing filament arrangements *Supercond. Sci. Technol.* **17** S440-4

[73] Orehotsky J, Reilly K, Suenaga M, Hikata T, Ueyama M, and Sato K 1992 AC losses in powder-in-tube $Bi_2Ca_2Sr_2Cu_3O_{10}$ tapes at power frequencies *Appl. Phys. Lett.* **60** 252-4

[74] Paasi J and Lahtinen M 1993 Characterization of high-T_c superconducting tapes using Hall sensors *Physica C* **216** 382–90

[75] Paasi J and Lahtinen M 1997 Computational comparison of AC losses in different kinds of HTS composite conductors *IEEE Trans. Appl. Supercond* **7** 322-5

[76] Paasi J, Kalliohaka T, Korpela A, Söderlund L, Herrmann P, Kvitkovic J, and Majoros M 1999 Homogeneity studies of multifilamentary BSCCO tapes by three-axis Hall sensor magnetometry *IEEE Trans. Appl. Supercond.* **9** 1598–601

[77] Paasi J, Lehtonen J, Lahtinen M, and Kettunen L 1998 Computation of AC losses in high-temperature superconductors *Physica C* **310** 62–6

[78] Paasi J, Masti M, Lehtonen J, and Kalliohaka T 2000 Frequency dependence of self-field AC losses in Bi-2223/Ag tapes *IEEE Trans. Appl. Supercond* **10** 1212-5

[79] Pachla W, Diduszko R, Kovác P, Husek I, and Presz A 2002 Spatial structure and composition homogeneity in Bi-2223 TIRT tapes *Physica C* **371** 291-300

[80] Pashitski A, Gurevich A, Polyanskii A, Larbalestier D, Goyal A, Specht E, Kroeger D, DeLuca J, and Tkaczyk J 1997 Reconstruction of current flow and imaging of current-limiting defects in polycrystalline superconducting films *Science* **275** 367–9

[81] Perkins G, Bugoslavsky Y, and Caplin A 2002 Deconvolution of 2D transport currents from the local magnetic field distribution above flat superconducting samples *Supercond. Sci. Technol.* **15** 1140–6

[82] Polák M, Kasztler A, and Kirchmayr H 2001 I-V curves and critical currents of Bi-2223/Ag tape and filaments extracted from it *Physica C* **354** 242-6

[83] Rabbers J, ten Haken B, and ten Kate H 1998 Measuring transport current loss of BSCCO/Ag tapes exposed to external AC magnetic field *Physica C* **310** 101-5

[84] Rabbers J, ten Haken B, and ten Kate H 2001 Advanced ac loss measurement methods for high-temperature superconducting tapes *Rev. Sci. Instrum.* **72** 2365-73

[85] Rabbers J, van der Laan D, ten Haken B, and ten Kate H 1999 Magnetization and transport current loss of a BSCCO/Ag tape in an external AC magnetic field carrying an AC transport current *IEEE Trans. Appl. Supercond.* **9** 1185-8

[86] Rabbers J, van der Meer O, Klein Zeggelink W, Shevchenko O, ten Haken B, and ten Kate H 1999 Magnetization loss of BSCCO/Ag tape in uni-directional and rotating magnetic field *Physica C* **325** 1-7

[87] Scanlan R, Malozemoff A, and Larbalestier D 2004 Superconducting materials for large scale applications *Proc. IEEE* **92** 1639-54

[88] Shaked N, Friedman A, Sinvani M, Al-Omari I, Wolfus Y, Shaulov A, and Yeshurun Y 2001 Effect of external magnetic field on the critical current in single and bifilar Bi-2223 tapes *Physica C* **354** 237-41

[89] Snitchler G, Campbell J, Aized D, Sidi-Yekhlef A, Fleshler S, Kalsi S, and Schwall R 1997 Long length calorimetric measurement of AC losses of Bi-2223 with external field oriented perpendicular to the tape width. *IEEE Trans. Appl. Supercond.* **7** 290-3

[90] ten Haken B, van Eck H, and ten Kate H 2000 A new experimental method to determine the local critical current density in high-temperature superconducting tapes *Physica C* **334** 163–7

[91] Tinkham M 1975 *Introduction to Superconductivity* (McGraw-Hill)

[92] Usák P 1999 Measurement of the transport current distribution in a superconducting tape *Physica C* **316** 229–33

[93] Usoskin A, Rutt A, Knoke J, Krauth H, and Arndt T 2005 Long-length YBCO coated stainless steel tapes with high critical currents *IEEE Trans. Appl. Supercond.* **15** 2604-7

[94] Vogel C 2002 *Computational Methods for Inverse Problems* (Philadelphia: SIAM)

[95] Welp U, Gunter D, Crabtree G, Luo J Maroni V, Carter W, Vlasko-Vlasov V, and Nikitenko V 1995 Magneto-optical imaging of flux patterns in multifilamentary $(BiPb)_2Sr_2Ca_2Cu_3O_x$ composite conductors *Appl. Phys. Lett.* **66** 1270–2

[96] Welp U, Gunter D, Crabtree G, Zhong W, Balachandran U, Haldar P, Sokolowski R, Vlasko-Vlasov V, and Nikitenko V 1995 Imaging of transport currents in superconducting $(Bi,Pb)_2Sr_2Ca_2Cu_3O_x$ composites *Nature* **376** 44–6

[97] Wijngaarden R, Heeck K, Spoelder H, Surdeanu R, and Griessen R 1998 Fast determination of 2D current patterns in flat superconductors from measurement of their magnetic field *Physica C* **295** 177–85

[98] Wilson M 1983 *Superconducting Magnets* (Oxford: Clarendon Press)

[99] Xing W, Heinrich B, Zhou H, Fife A, and Cragg A 1994 Magnetic flux mapping, magnetization, and current distributions of $YBa_2Cu_3O_7$ thin films by scanning Hall probe measurements *J. Appl. Phys.* **76** 4244–55

[100] Zhang P, Inada R, Uno K, Oota A, and Zhou L 2000 Reduction in alternating-current transport losses of a $(Bi,Pb)_2Sr_2Ca_2Cu_3O_x$ multifilamentary tape-form conductor by the introduction of resistive barriers *Supercond. Sci. Technol.* **13** 1505-8

Tampereen teknillinen yliopisto
PL 527
33101 Tampere

Tampere University of Technology
P.O. Box 527
FIN-33101 Tampere, Finland